University of Alberta

Investigation of Gradient Echo MRI for Blood Vessel Imaging and

Susceptibility-Weighted Imaging in the Human Brain

by

Amir Eissa

A thesis submitted to the Faculty of Graduate Studies and Research
in partial fulfillment of the requirements for the degree of

Doctor of Philosophy

Physics

Examining Committee

Dr. Alan Wilman; Department of Biomedical Engineering.

Dr. Frances Fenrich; Department of Physics.

Dr. Jack Tuszynski; Department of Physics.

Dr. Nicola De Zanche; Department of Oncology.

Dr. Richard Frayne; Department of Radiology and Clinical Neurosciences; University of Calgary.

To My Parents;
To All whom they love
and All who love them.

To my beloved daughter Malak
"May you become the best learner
and the kindest truth seeker"

To My Teachers.

Abstract

Despite the vast myriad of applications and the long way it has come, MRI is still a relatively new field of knowledge with much prospect for more advancement and expansion. This work is mainly concerned with two gradient echo imaging methods which are directly or indirectly related to blood vessel imaging as well as iron depiction in the human brain. In each case, new methods are introduced that overcome existing limitations.

For blood vessel imaging, 3D Time-of-Flight (TOF) MR angiography (MRA) with its known capability to image arteries as well as veins was implemented at 3.0 T. At this field strength, the significant RF profile variability due to RF interference is a liability for circle-of-Willis imaging in the human brain that was overcome by introducing a new means to counter the RF effects through increased slope of the ramped pulse. In addition a new method is introduced for TOF MRA with two-in-one arterial and venous 3D TOF imaging to overcome the significant scan time overhead of a traditional second venous scan and for cutting down RF power utilization. Using this method total scan time could be reduced by as much as 46% and specific absorption rate (SAR) due to spatial saturation could be reduced by as much as 92%.

For iron sensitive imaging, Susceptibility Weighted Imaging (SWI) was developed at 4.7 T. The phase SWI method was used to visualize lesions in Multiple Sclerosis (MS) patients and was experimentally compared to the

visibility on standard T2 weighting with results demonstrating visualization of new lesions, with 18% of total lesions exclusively visible on SWI.

A new approach to 3D imaging was also introduced to enable accurate oblique SWI scanning while overcoming the current restriction to axial imaging to produce correct phase effects for oblique imaging. New results from oblique phase imaging were presented and the phase measurements from key brain structures were successfully validated against images obtained by the current standard of axial imaging.

Acknowledgement

Table of Contents

List of Tables

List of Figures

List of Abbreviations

1.5T	1.5 Tesla (magnet or magnetic field)
1.5 T	1.5 Tesla (magnet or magnetic field)
2-stage	Two stage
3.0T	3 Tesla (magnet or magnetic field)
3D	Three dimensional
ACQ	Acquisition (relating to)
ADC	Analog to Digital Converter
B_o	Main static field strength
BOLD	Blood Oxygenation Level Dependent (Contrast)
CNR	Contrast to Noise Ratio
CSF	CerebroSpinal Fluid
FLAIR	Fluid Attenuated Inversion Recovery
CT	Computerized Tomography
FID	Free Induction Decay
fMRI	functional Magnetic Resonance Imaging
FOV	Field of view
FSE	Fast Spin Echo
FT	Fourier Transform
GM	Gray Matter
GP	Globus Pallidus
GRE	Gradient Recalled Echo
GRO	Read out gradient
H	Magnetic field (vector)
Hct	Hematocrit
ISEE	Independent Slab Excitation and Encoding
iso-center	Central point of the MRI magnet bore that is considered the point of origin
M	Magnetization (Vector) due to susceptibility effect
MAP	Maximum Activity Projection
MCA	Middle Cerebral Arteries

MHz	Megahertz
MIP	Maximum Intensity Projection
mIP	minimum Intensity Projection
M_o	Magnetization at thermal equilibrium
MPR	Multi-Planar Reformatting
MR	Magnetic Resonance
MRA	Magnetic Resonance Angiography
MRI	Magnetic Resonance Imaging
MS	Multiple Sclerosis
ms	Millisecond
M_{XY}	Transverse magnetization
M_Z	Longitudinal magnetization
NMR	Nuclear Magnetic Resonance
PAC	Phased Array Coil(s)
PD	Proton Density
PE1	Phase encoding (first phase encoding in case of 3D imaging)
PE2	Second (slice) Phase Encoding in 3D imaging
pss	Position of slice selection
pss'	Position of slice selection (modified)
Ramp1	Regular ramp pulse
Ramp1.5	Ramp pulse with slope x 1.5
Ramp2	Double sloped ramp pulse
RF	Radiofrequency
RN	Red Nucleus
ROI	Region of Interest
SAR	Specific Absorption Rate
SD	Standard Deviation
SE	Spin Echo
SENSE	SENSitivity Encoding
SMASH	Simultaneous Acquisition of Spatial Harmonics
SN	Substantia Nigra

SNR	Signal to Noise Ratio
SS	slice selection (relating to)
SW	Susceptibility Weighted
SWI	Susceptibility Weighted Imaging
T	Tesla
t	Time
T'_2	Relaxation time constant based on local magnetic field non-uniformities
T_1	Longitudinal relaxation (time constant)
T_2	Transverse relaxation (time constant)
T_2*	Effective transverse relaxation for Gradient Echo (time constant)
T2WFSE	T2 weighted fast spin echo
TE	Echo Time
TEM	transverse electromagnetic (coil)
thk	Thickness
TOF	Time of Flight
TR	Time of Repetition
W	Watts
WM	White Matter
α	Excitation flip angle
γ	Magnetogyric ratio
θ	Theta, angle
χ	Magnetic susceptibility
ω_o	Larmor frequency

Chapter 1

Introduction

1.1 Introduction to the Thesis (Overview)

The objective of this dissertation is to present the methods and results obtained by the application of gradient-echo magnetic resonance imaging (MRI) at both clinical and high field strengths. In this work, two main imaging techniques were investigated and compared to standard imaging: the susceptibility-weighted imaging (SWI) and a modified 3-D time-of-flight (TOF) angiography.

MRI is a technique primarily used in medical imaging to visualize the structure and function of the body. It provides detailed images or pictures of the inside of the body, including the soft tissues of the brain and spinal cord, in any plane. Unlike computed tomography (CT), MRI does not use X-rays. Rather, MRI uses a powerful magnet and sends radio waves through the body; the images can appear on a computer screen as well as on film. As such, MRI has much greater contrast than CT, making the former useful especially for neurological diseases. The advantages of MRI among other medical diagnostic techniques are its non-invasive nature, versatility, excellent tissue contrast and sensitivity to flow and diffusion.

Depending on the tissue being scanned, it is known that different tissues have different magnetic susceptibilities. Susceptibility in this context is defined as the extent or degree of magnetization of a material caused by the application of a

magnetic field. This exact difference between tissues can serve as a mark or label to distinguish various structures by obtaining images with various contrasts. The SWI is based on this fact and it is quite possible to obtain distinct pictures for various body structures or tissues (water, fat, protein, brain, spinal cord, etc.).

On the other hand, the time of flight technique, TOF, exploits blood flowing nature to distinguish it from stationary tissues. Researchers studying the nature of flow in controlled phantoms developed the early work on TOF. A phantom is an artificial object of certain characteristics and composition that is scanned to calibrate or validate the MRI system. Parameters validated include homogeneity, imaging performance and orientation aspects. A phantom is usually a container made often of polymers, has various shapes and filled with fluid.

Different techniques were developed for flow-based MRI. In general, these techniques can be divided into three major categories based on the effects used for imaging: (a) "time-of-flight" effects (1-7); (b) velocity-induced phase (8-11); and (c) signal enhancement caused by MR contrast agents.

Both SWI and TOF techniques have different applications in blood vessel imaging. As well, they have different basis. As mentioned above, the TOF method depends on the movement of arterial or venous blood to enhance its signal, while the SWI method is based on the utilization of the magnetic properties of deoxygenated hemoglobin, resulting in darker imprints for venous structures. In this research, the SWI method was studied at magnetic field strength of 4.7 T, while the TOF method was studied at both 1.5 and 3.0 T.

The two methods have wide spread applications in both established and emerging clinical diagnosis. Both methods have limitations, either inherently or relevant to higher field strengths (greater than 1.5 T).

The research presented here is an attempt to overcome some of the limitations of the two imaging methods and find new applications of SWI in clinical imaging of multiple sclerosis (MS).

In this chapter, a brief introduction to MRI and its techniques is presented. This is followed by a review of the various techniques used along with a survey of previous relevant work as it appears in the open literature. This will be followed by a comparison of different methods, identification of research gaps and the significance of performing this research. Some of the preliminary results obtained in early research development will also be presented to highlight the theoretical background of this research, while showing the novelty in the experimental procedures.

The subsequent chapters will discuss in detail the techniques developed supported by a thorough analysis of data collected and an overall assessment of the results obtained or new findings.

In chapter 2, the experimental work conducted by implementing SWI at 4.7 T is discussed. The results obtained are compared to those obtained by fast spin echo (FSE) method to MS patients. It will be shown that improved visualization of MS lesions is possible using SWI at higher field strengths, reflected by more clear contrasts. As such, it is possible to use SWI to track the

progression of this disease with more precision, allowing better understanding of the disease, opening the way for possible effective medical treatment.

In chapter 3, a new method is introduced to overcome the current restriction of applying SWI almost solely to axial imaging. The new technique depends on separate excitation and acquisition volumes. It allows imaging at various angles, along oblique planes, hence called oblique SWI.

In chapter 4, the effects of radio frequency (RF) inhomogeneity on TOF ramp pulse excitation are discussed. Using higher field strengths (3.0 T), a solution is also offered to better visualize the intracranial arteries.

In chapter 5, a new TOF imaging technique is presented based on simultaneous arteries and veins scanning. The technique produces two distinctive sets of images. Although the total scanning time is slightly higher than that for one image, yet it still reduces considerably the significant scan-time overhead of a second venous scan while decreasing the deposition of RF power in the sample.

In this research, the experimental work was executed using Varian® High Field MRI Scanner (Varian, Palo Alto, CA) with field strength of 4.7 T, a 3.0 T MRI system (SMIS, Surrey, UK) and a 1.5 T Siemens Sonata MRI system (Siemens, Erlangen, Germany).

1.2 Magnetic Resonance Imaging

Every human cell contains hydrogen atoms (protons with **spin** property). When a patient is placed within a magnetic field, these protons align like tiny magnets. When radio-frequency (RF) pulses producing an **electromagnetic** field are transmitted in a plane perpendicular to the magnet, these protons become

excited. When such protons return to their original state, i.e. relax, energy is produced, which can be received and translated into images (12).

MRI scanning can discriminate between body substances based on their physical properties, for example, differences between water and fat containing tissues. MRI scanning is therefore particularly useful at providing highly detailed images of soft tissues. MRI scanning can also provide images in various planes without the movement of the patient.

On an MRI scan some tissues appear to be brighter or darker than others. Brightness might depend on the density of protons in that area (an increased density being associated with a brighter area). Relaxation times for the hydrogen protons can vary and two times are commonly measured: Longitudinal relaxation time, known as T_1, and transverse relaxation time, known as T_2. Relaxations time properties are routinely used to show contrast between different soft tissues.

At equilibrium, the net magnetization vector lies along the direction of the applied magnetic field, orthogonal to the plane taken and is called the equilibrium magnetization (see definition of magnetization below). In this configuration, there is no transverse magnetization. The net magnetization is called longitudinal magnetization.

1.2.1 Relaxation Times and the Bloch Equations

It is possible to change the net magnetization vector by providing certain energy to the nuclear spin system. In electromagnetic terms, this energy has certain frequency, which depends on the static magnetic field as well as the type of nuclear species being studied. If enough energy is put into the system, it is

possible to transform the spin system and bring the longitudinal magnetization to zero.

The time constant which describes how this longitudinal magnetization returns to its equilibrium value is called the spin-lattice relaxation time (T_1). This effect is mainly induced by the exchange of energy between different nuclear spins as they move in random patterns and thus cause microscopic changes in the magnetic field. T_1 is simply the time to reduce the difference between the longitudinal magnetization and its thermal equilibrium value by 63%. The Bloch equations offer the main mathematical framework for explaining the behavior of magnetic spins during relaxation.

If the net magnetization is placed in the opposite direction (anti-parallel with the main field), it will gradually return to its original, equilibrium position at a rate governed by T_1.

If the net magnetization is placed in the transverse plane, it will rotate about an axis orthogonal to that plane. The rotational frequency would equal the frequency of the photon that causes a transition between the two energy levels of the spin. This process is called precession, or oscillation, and the frequency exploited is called Larmor frequency.

$$\omega_o = \gamma \, B_o \qquad\qquad\qquad (1\text{-}1)$$

where ω_o is the Larmor frequency (radians s^{-1}), B_o is the static field strength (Tesla) and γ is gyromagnetic ratio (radians s^{-1} T^{-1}) (13).

The transverse magnetization component rotates about the direction of the static field and dephases. Dephasing here means that smaller compenents of the

transverse magnetization rotate with respect to each other or go out of phase (angle) in the transverse plane once the RF pulse is turned of. In addition to this rotational dephasing, the net magnetization starts to dephase because each of the spin or proton packets making it up is undergoing a slightly different magnetic field and rotates at its own Larmor frequency. The longer the time elapsed, the greater is the phase difference. Here the net magnetization vector is initially along one of the transverse axes. This vector can be depicted as the overlap of several thinner vectors from the individual proton packets contributing to the whole dephasing process. The time constant that governs the rate of decaying of the transverse magnetization is called the spin-spin relaxation time, T_2.

T_2 is always less than or equal to T_1. The net magnetization in the transverse plane goes to zero and then the longitudinal magnetization increases until it reaches the value of the net magnetization. T_1 governs the rate of recovery of the longitudinal magnetization.

In the previous discussion, the system relaxation processes, described by T_2 and T_1 times, are described individually for clarity. In reality, both processes occur simultaneously with the only restriction being that T_2 is always less than or equal to T_1.

The decay of transverse magnetization is attributed to two factors:

1) Molecular interactions, said to lead to a pure T_2 molecular effect.

2) Variations in the strength of the original magnetic field, said to lead to T'_2 effect, which significantly drops the signal-to-noise ratio (SNR).

The combination of these two factors is what actually results in the decay of transverse magnetization in all GRE (Gradient Recalled Echo) imaging sequences. The combined time constant is called T_2^*. The relationship between T_2 from molecular processes and that from inhomogeneities in the magnetic field (T'_2) is as follows:

$$\frac{1}{T_2^*} = \frac{1}{T_2} + \frac{1}{T_2'}$$

(1-2)

With MRI dependence on the more biologically variable parameters of 1) proton density, 2) longitudinal relaxation time (T_1) and 3) transverse relaxation time (T_2), variable image contrast can be achieved by using different pulse sequences and by changing the imaging parameters. As a matter of fact, white material is darker than gray material in T_1-weighted images and brighter than gray material in T_2-weighted images (12).

Signal intensities on T_1-, T_2- and proton density-weighted images relate to specific tissue characteristics. For example, the changing chemistry and physical structure of hematomas over time directly change the signal intensity on MR images, providing information, for example, about the progress of a bleeding. Moreover, with MR's multiplanar capability, the imaging plane can be optimized for the anatomic area being imaged. Consequently, the relationship of lesions, for example, to other areas of the brain can be identified more accurately.

The behavior of magnetic fields and electric fields is described by the well-known Maxwell equations. The behavior of magnetic fields and magnetization can also be described by Bloch set of equations (14). Bloch

equations are a set of coupled differential equations that describes the rate of change of magnetization with time. If properly integrated, often by numerical methods, Bloch equations can estimate the components of magnetization as a function of time and under any condition. The difference from Maxwell equations is that they relate the components of the magnetic field to the system relaxation time (T_1 and T_2), rather general time frames.

The equation governing the rate of change of longitudinal magnetization is as follows:

$$\frac{dM_Z}{dt} = -\frac{M_\circ - M_Z}{T_1}$$

(1-3)

where M_Z is the longitudinal magnetization, M_o is the equilibrium magnetization and T_1 is the longitudinal relaxation time constant.

If the above differential equation is solved for longitudinal magnetization following a 90 excitation, it yields:

$$M_Z(t) = M_\circ (1 - e^{\frac{-t}{T_1}})$$

(1-4)

The equation governing the rate of change of transverse magnetization (M_{XY}) is as follows:

$$\frac{dM_{XY}}{dt} = -\frac{M_{XY}}{T_2}$$

(1-5)

where T_2 is the transverse relaxation time constant.

On solving the above equation for M_{XY} it yields:

$$M_{XY}(t) = M_{XY}(0).e^{-t/T_2}$$

(1-6)

Depending on the pulse sequence being used, the time constant T_2 is used as is (in SE applications) or replaced by the time constant T_2^* (in case of GRE applications).

Bloch showed a resemblance between magnetic resonance and mechanical resonance. In the latter, friction is responsible for the transmission of mechanical energy to the surrounding environment. In MR, the transmission of energy created by the magnetic moment to its surrounding or local environment is mediated through proton relaxation and is primarily due to its thermal "contact" with that environment (fluctuating magnetic fields). Since proton relaxation is described in terms of relaxation times, the variation, or rate of change, of the components of the magnetic field are proportional to the system relaxation times (T_1 and T_2).

Further advancements in MRI techniques were made possible by the incorporation of new agents or methods. For example, the introduction of Gadolinium contrast agents allowed better enhancement of image contrast for the so-called regions of interest (ROI).

Improvements in acquisition and analysis software to unprecedented levels were made possible by the fast developments in computer science and processor technology, especially high-speed processors. This opened the way for significant improvement in post-processing imaging. Examples are temporal subtraction (post-contrast-pre-contrast images), intensity-to-time curves for small, targeted

regions of interest (ROI), maximum intensity projection (MIP), minimum intensity projection (mIP) and multi-planar reformatting (MPR).

1.2.2 MRI Hardware

An MR system consists of the following components: 1) a powerful magnet to generate the static magnetic field, 2) homogenizing coils (called shim coils) to make the magnetic field as equally distributed as possible, 3) an RF coil to for radio signal transmission into the body part being scanned, 4) a receiver coil to detect the returning radio signals (echo), 5) gradient coils to detect and provide spatial localization of the signals, and 6) a computer system for reconstruction of the final image from radio signals received (15).

The magnet produces the required field strength for the imaging procedure (normally 1.5 T, but up to 11 T has been built). The first coil used in an NMR experiment was the multi-turn solenoid coil. After that, the birdcage coil (Figure 1-1) was introduced by Hays (16) and became the most routinely used volume coil in MRI, especially for imaging the head and brain.
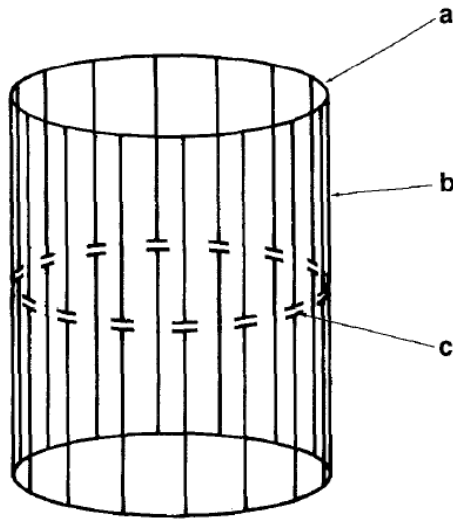
Figure 1-1: Birdcage Coil. (a) Circular End Ring; (b) Straight Segment; (c) Capacitor.

It is widely acceptable that the birdcage coil provides a better overall magnetic field homogeneity and improved SNR compared to older coil designs, such as the solenoid coils. Field homogeneity ensures uniform atomic nuclei, allowing a large field of view (FOV), while the high SNR ensures obtaining high resolution images. Actually, the ability of birdcage coils to produce circularly polarized fields using quadrature excitation can increase the SNR by 41%, making the images more resolvable (17).

Sometimes the birdcage coil is shielded from other coils (i.e. shim and gradient coils) inside the MRI set-up to minimize any interference. The birdcage coil was the basis for further improvements in coil design and assembly. New designs were developed and used, such as end-capped birdcage resonator and the double tuned quadrature birdcage coil. A birdcage coil or other types of RF coils

can alternatively function as a transmitter coil, as a receiver coil or can be used for both functions.

The transmitter coil creates the magnetic field that excites the nuclei of the tissue. It is essential to have a uniform field over the region of interest to provide a spatially uniform excitation. If inhomogeneous magnetic field is created, some of the nuclei are either not excited or excited with different flip angles, leading to poor image contrast and SNR. The receiver coil detects the resonance signal then induces a corresponding voltage.

As the nuclei relax back to their original state, they emit some RF energy that has the same frequency as the applied RF signal. The signal emitted is often referred to as free induction decay (FID) or the NMR signal. With different tissues, the nuclei relax at different rates leading to different time-varying signal levels and consequently different tissue contrast in the image. Using the magnetic gradients, the spatial location is determined and the measured signal is transformed to an image via signal processing tools.

The RF coils are required to have a large filling/loading factor (volume of sample per volume of the coil). By having the size of the body part to be imaged and the size of the coil comparable, a good SNR is achieved because the system is less sensitive to the external thermal noise and the receiver coil is close to the region of interest. This factor becomes more important at high magnetic fields (Section 1.5).

Surface RF coils are very popular because they serve as a receive-only coil, but their sensitivity drops off as the distance from the coil increases. They

have a good SNR for tissues adjacent to the coil. The advantage of surface coils is their ability to produce a strong and localized RF field that can provide a high SNR compared to other coils, especially in the imaging of relatively small volumes.

Surface coils are often used for better signal reception. This is because they are sensitive to signals close to the coil, which means that surface coils can detect the signal in an organ of interest more efficiently. The surface coils amplify the noise signal, but the loss in coil sensitivity compensates for this amplification, since the coils remain indifferent to noise signals from the rest of the patient (i.e. further away from the coil). Surface coils can also be optimized to image deep-body structures.

Scan room is surrounded by an RF shield. The shield prevents the high power RF pulses from radiating out through the hospital. It also prevents the various external RF signals (e.g. television and radio signals) from being detected by the imager. Some scan rooms are also surrounded by a magnetic shield, which prevents the magnetic field from extending too far into the hospital. In newer, powerful magnets, the magnet shield is an integral part of the assembly. The patient is positioned within the magnet by a computer controlled patient table. The table has a positioning accuracy of 1 mm.

The heart of the MRI system is the computer. It controls all the components of the scanner. The computer also controls the RF components: RF source and pulse programmer. The source produces a sinusoidal wave at predetermined frequency. The pulse programmer converts the RF pulses into

desired pulse shapes as dictated by the operator. The RF amplifier increases the pulse power from milliwatts to kilowatts. The computer also controls the gradient pulse programmer, which sets the shape and amplitude of each of the magnetic field gradients. The gradient amplifier increases the power of the gradient pulses to a level sufficient to operate the gradient coils.

The signal intensity on the MR image might be determined by four basic parameters: 1) proton or spin density, 2) T_1 relaxation time, 3) T_2 relaxation time, and 4) flow. Proton density is the concentration of protons (hydrogen atom nuclei) in the tissue in the form of water and macromolecules (proteins, fat, etc). The T_1 and T_2 relaxation times (see above) define signal behavior after excitation as well as the way the protons revert back to their resting states (equilibrium) after the initial RF pulse excitation.

1.2.3 Pulse Sequence

One of the confusing aspects of MRI is the variety of pulse sequences available from different equipment manufacturers. A pulse sequence is the measurement technique by which an MR image is obtained. It contains the hardware instructions (RF pulses, gradient pulses and timings) necessary to acquire the data in the desired manner.

As implemented by most manufacturers, the pulse sequence actually executed during the measurement is defined from parameters directly selected by the operator (e.g. repetition time; TR, field of view; FOV) and variables defined in template files (e.g. relationships between RF pulses and slice selection gradients). This allows the operator to create a large number of pulse sequence

combinations using a limited number of template files. It also enables the manufacturer to limit parameter combinations to those suitable for execution. Sometimes, similar sequences may be known by a variety of names by the same manufacturer, adding to the confusion of pulse sequences (18). As a result, comparison of techniques and protocols between manufacturers is often difficult due to differences in sequence implementation. To have such a comparison, knowledge of confidential, proprietary information might be needed.

The contrast on the MR image can be manipulated by changing the pulse sequence parameters. A pulse sequence sets the specific number, strength, and timing of the RF and gradient pulses. The two most important parameters are the repetition time (TR) and the echo time (TE). The TR is the time between consecutive RF pulses. The TE is the time between the initial RF pulse and the received signal peak (echo).

The most common pulse sequences are the T_1- weighted and T_2-weighted sequences. The T_1-weighted sequence uses a short TR and short TE (TR < 1000 ms, TE < 30 ms). The T_2-weighted sequence uses a long TR and long TE (TR > 2000 ms, TE > 80 ms).

The T_2-weighted sequence can be employed as a dual echo sequence. The first or shorter echo (TE < 30 ms) is proton density (PD) weighted or a mixture of T_1 and T_2 weighting. This image can be very helpful in studying periventricular pathology. For example, it can be used in evaluating multiple sclerosis, because the hyper-intense plaques are contrasted against the lower signal cerebrospinal fluid (CSF). More recently, the FLAIR (Fluid Attenuated Inversion Recovery)

16

sequence has replaced the PD image. FLAIR images are T_2-weighted with the CSF signal suppressed (19).

Generally, there are two commonly used pulse sequences in MR imaging:

1) Spin Echo Sequence, and

2) Gradient Echo Sequences

Spin echo sequence is a pulse sequence whose signal is an echo resulting from the refocusing of magnetization after the application of a 90° and 180° RF pulses. It has at least two RF pulses, an excitation pulse, often called the α pulse and one or more $180°$ refocusing pulses that generate the spin echo(s). A refocusing pulse is required for every echo produced, making it a tedious procedure. Spin echo sequences also utilize gradient pulses of opposite polarity in the readout and slice selection directions to refocus the protons at the same time as the spin echo. That implies a longer protocol, demanding some extra human resources or prolonged imaging time. Spoiler gradients are used following signal detection to dephase any residual transverse magnetization and minimize spurious echoes (20).

In a spin echo sequence, the repetition time, TR, is the time between successive excitation pulses for a given slice. The echo time, TE, is the time from the excitation pulse to the echo maximum. A multi-slice loop structure is used to acquire signals from multiple slices within one TR time period.

On the other hand, gradient echo sequences, often called gradient recalled echo sequence (GRE) do not use a $180°$ pulse to refocus the protons. Rather, the echo signal is generated only through gradient reversal. The application of

imaging gradients induces proton dephasing. Application of a second gradient pulse of the same duration and magnitude but of opposite polarity reverses this dephasing and produces an echo known as gradient echo.

All gradient echo sequences use gradient reversal pulses in at least two directions (the slice selection and the readout directions) to generate the echo signal. Excitation angles less than 90° are normally used.

The absence of the 180° RF pulse in gradient echo sequences has several important consequences. The sequence kernel time may be shorter than for an analogous spin echo sequence enabling more slices to be acquired for the same TR if a multi-slice loop is used (15). This is very unique and implies versatility, in that image refining and reconstruction is easily achieved. More information or details can be revealed once more slices are used. As well, it implies that less total RF power is applied to the patient, so that the total RF energy deposition is lower. Additional contrast mechanisms are also possible. The static sources for proton dephasing, which are magnetic field inhomogeneity and magnetic susceptibility differences, contribute to the signal decay. As such, the echo time (TE) determines the amount of T_2^*-weighting in a gradient echo image rather than only T_2-weighting, as in a spin echo image.

For these reasons, the overall signal level in gradient echo images is expected to be less than that in spin echo images, yet with comparable acquisition parameters. The image quality of gradient echo sequences is also more sensitive to metal implants and to the region of anatomy under investigation. In addition, fat, protein and water protons within a voxel also contribute different amounts of

signal depending upon the chosen echo time, due to their different frequencies and hence different phases at echo time.

1.2.4 Gradient Echo Pulse Sequence

The procedure for generating an image varies from one instrument to another, but can be described in terms of a timing diagram. This diagram is used to examine and test for imaging sequence (Figure 1-2, for example). In this context, the timing diagram has entries for the signal, magnetic field gradients and radio frequency as a function of time.
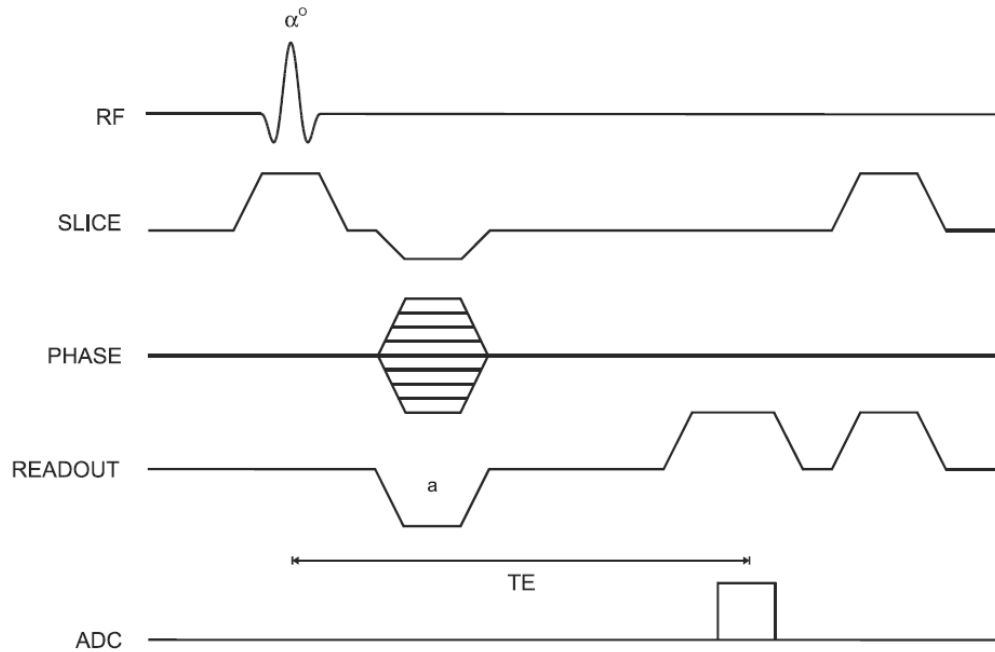
Figure 1-2: Spoiled gradient-echo sequence timing diagram. Because there is no 180° RF pulse, the polarity of the G_{RO} dephasing gradient pulse (α) is opposite that of the readout gradient pulse applied during signal detection. Gradient spoiling is illustrated at the end of the loop. The TE time is measured from the middle of the excitation pulse to the center of the echo. ADC is analog-to-digital converter (15).

The simplest FT imaging sequence contains a phase encoding gradient pulse, a frequency encoding gradient pulse, a slice selection gradient pulse, a 90°

19

slice selective RF pulse and a signal. The pulses for the three gradients represent the magnitude and duration of the magnetic field gradients.

The first event to occur in this sequence is to turn on the slice selection gradient and the slice selective RF pulse simultaneously. The RF pulse can be a truncated sinc function-shaped burst of RF energy. Once the RF pulse is complete the slice selection gradient is turned off. The phase encoding gradient is turned on. Once the latter is turned off, the frequency-encoding gradient is turned on and the signal generated is recorded. Slice selection gradient is followed by slice refocusing gradient lobe while the read-out gradient is preceded by read-out dephasing gradient lobe.

This sequence of pulses is repeated many times to collect all the data needed to produce an image. As mentioned before, the time between the repetitions of the sequence is called the repetition time, TR. Each time the sequence is repeated the magnitude of the phase encoding gradient is changed. The magnitude is changed in equal steps between the assigned maximum and minimum values of the gradient.

The slice selection gradient is always applied perpendicular to the slice plane. In MRI, slice selection is the selection of protons in a plane passing through the object. Larmor equation is the determining rule for this selection. Slice selection is conducted by applying a one dimensional, linear magnetic field gradient at the same time the RF pulse is applied. A 90° RF pulse applied in conjunction with the magnetic field gradient will excite the protons in the area of interest. The frequency-encoding gradient is applied along one of the sides of the

image plane, while the phase-encoding gradient is applied along the remaining edge of the image plane. As such, there is a sequence combination encompassing the slice selection, phase- and frequency-encoding gradients.

The signal from the receiver coil(s) is amplified and then the carrier frequency is removed (demodulated). This practically produces NMR signal in the rotating frame. The resulting signal lies in the audio/supersonic frequency range. In the so-called quadrature detection process, the signal is then converted from "real" signal into complex signal (real and imaginary), which is ready for Fourier transformation (13). The data is then digitized (e.g. using analog to digital converter ADC).

Fourier transformation is used convert the above measured data (k-space) into image space. Mathematically, the image data is of complex form, which has two sub-components, a magnitude component or image and a phase component or image.

Magnitude images are the most commonly used part of MR images where most contrast mechanisms work. Phase images on the other hand can be used to show flow or susceptibility effects.

MR signals are corrupted by "white" noise, which has a Gaussian (normal) probability distribution. After the inverse Fourier transform of the complex data is completed, the noise in the complex image data is still white (Gaussian). The image data is not derived from the real or imaginary components of the image data. That is, the data are not the result of calculations using only the real data, or

images using only the imaginary data. Rather, both parts of the complex data values are used, and magnitude images and phase images are derived (15).

Each image has a physical meaning: examples are flow for phase image and proton density for magnitude image. After performing the FT, magnitude images are the real and the imaginary parts combined together and calculated as a scalar quantity, while phase images are the angular component of the complex number (the angle of the transverse field vector at each image pixel).

After making the calculation of a magnitude image, the noise probability distribution is no longer Gaussian (white). Rather, it becomes Rician (tending to a Rayleigh distribution as the SNR goes to zero) (21).

1.2.5 Image Resolution

The previous discussion of MRI assumes that the magnetic resonance scanner is functioning exactly as the theory suggests and high-resolution images are readily obtainable. In real-life applications this is not the case.

Resolution is a measure of image quality. It is inversely proportional to the distance of two resolvable features. When two features in an image are distinguishable, the image is said to be high-resolution. The ability to resolve distinctive features in an image is a function of many variables; the exponential decay time of signal (T_2), signal corruption by noise (or signal-to-noise ratio; SNR), sampling rate, slice thickness, and image matrix size, to name a few.

A high-resolution MR image can be thought of as the convolution of the nuclear magnetic resonance (NMR) spectrum of the spins (protons) with their spatial concentration map (22).

To get high-resolution images, three factors are important (23):

i. Temporal (or time) resolution, which should be high so that motion effects (called artifacts) do not dominate and degrade edge sharpness,

ii. Contrast resolution, which must be high so that edges of organs and lesions can be identified easily against the background tissue or noise; and

iii. Spatial (gradient or location) resolution, which also must be high so that small objects and closely spaced edges are detectable.

1.2.6 Image Artifacts

Usually, there is a trade-off between high contrast, high temporal, and high spatial resolutions and, consequently, image artifacts are occurring.

An image artifact is any feature which appears in an image, a feature that is not originally present in the imaged object. An image artifact is sometime the result of improper operation of the imager, instrument or system-related factors and, frequently. a consequence of natural processes or properties of the human body.

Though it is a noninvasive technique, producing high quality, diagnostically interpretable MRI images often require long imaging times compared with physiologic motions. These long imaging times mean that patient motion, which is not avoidable at all, causes blurring and replication (more commonly known as ghosting) artifacts. Examples include respiration, cardiac motion, blood flow, peristaltic motion of the digestive system or restlessness of the patient. That might lead to serious errors in interpreting the images obtained, because such errors or artifacts can obscure, and be mistaken for, pathology.

Therefore, it is important to be familiar with the appearance and dealing with artifacts to avoid further technical or legal liabilities.

The most common types of artifacts are those related to motion and phases. As the name suggests, motion effects in MR are the results of the movement of the imaged object or a part of the imaged object during the imaging sequence. The motion of the entire object during the imaging sequence generally results in a blurring of the entire image with ghost images in the phase encoding direction. Movement of a small portion of the imaged object results in a blurring of that small portion of the object across the image.

The solution to a motion artifact is to immobilize the patient or imaged object. Heart beating and patient breathing are more difficult to deal with, because they are unavoidable. The experienced operator would use the so-called gating, where the imaging pulse sequence is gated to the cardiac or respiratory cycle of the patient. For example if the motion is caused by pulsing artery, one could trigger the acquisition of phase encoding steps to occur at a fixed delay time after the R-wave in the cardiac cycle. By doing this, the artery is always in the same position. Similar gating could be done to the respiratory cycle. A disadvantage of this technique is that the choice of TR is often determined by the heart rate or respiration rate.

Different acquisition and post processing techniques have been suggested to deal with motion artifacts. Examples include nulling of the gradient moment, data averaging, adaptive data correction and others.

Various manufacturers of MRI machines give different names for techniques designed to remove motion artifacts. For example, a few names of sequences designed to remove respiratory motion artifacts are respiratory gating, respiratory compensation and respiratory triggering (22).

The flow-induced phase-shift artifact is caused by movements of the patient or organic processes taking place in the body of the patient. The artifact appears as bright noise, repeating densities or ghosting in the phase encoding direction.

The flow-induced phase-shifts, sometimes called phase encoded motion artifact, depend on several variables related to the coupling of the flow parameters with the parameters of the specific imaging pulse sequence used. Examples include flow direction, strength and duration of gradient pulses, echo time, velocity modulation (random or sinusoidal), mean velocity and the duration of the data acquisition window. Again, the image produced might look blurred or have ghosting.

1.2.7 Flow Compensation

Compensation techniques are commonly used to mitigate this effect. Flow compensation is the addition of gradient waveform lobe to make-up for the loss in phase coherence (that is, phase dispersion) for non-accelerating spins. For example, the flow compensation pulse is designed to produce a zero phase shift at a specified point in time, which is the echo time. Sometimes more averages, anti spasmodic, presaturation techniques are used. Phase shift effects are produced by

movements of the protons under existence of any field gradient, i.e., the slice selection, the phase encoding or the readout gradients.

These phase shifts produce many non-linear effects on the resulting images. On the one hand, these effects may result in several types of artifacts as well as a loss in the signal. On the other hand, the same phase shifts may be controlled to produce images depicting desired flow characteristics, giving NMR its unique ability to image and eventually quantify in-vivo flow. Flow and velocity compensation concepts were discussed early by (24-27) and were also addressed for both SE and GRE mothods (28). Flow compensation is further discussed in section 1.4.1.

1.2.8 Maximum and Minimum Intensity Projections

Maximum Intensity Projection (MIP) is the most commonly used MRI processing technique. Originally, it was called MAP (Maximum Activity Projection). It is simply a computer visualization of 3D data that in the visualization plane projects the voxels (volume elements) with maximum intensity that fall in the way of parallel rays traced from the viewpoint to the plane of projection. By this, two MIP renderings from opposite viewpoints are symmetrical images. Using special ray-tracing algorithms, an image of unique pixels (picture elements) is produced, representing the highest intensity signal in that location within the examined volume.

Although it is computationally fast, the downside of this method is that the 2D results do not provide a good sense of depth, or penetration, of the original data. To improve the sense of 3D, animations are usually rendered of several MIP

frames, where the viewpoint is continuously changed, creating the illusion of rotation. This helps the viewer's perception to find the relative 3D positions of certain features. In symmetrical structures, the viewer will find difficulty in distinguishing between left and right or front and back, unless depth weighting is used during production. This might also help in recognizing clockwise and counterclockwise rotations.

MIP-MRI has found some medical applications, for example, in evaluating the morphology of breast implants in the doubt of implant failure. In contrast-enhanced MRI, it is possible to evaluate the presence of malignant lesions on the basis of morphology and enhancement pattern. Using MIP for post-processing reconstructions, the morphology and spatial distribution of these lesions is further diagnosed, allowing any further surgical treatment (29).

In a similar fashion to MIP, minimum intensity projection (mIP) is another way of data post-processing. Here, the voxels with minimum intensity that fall parallel to the lines or rays are traced back to the projection plane. This method is sometimes used in black blood MR angiography. The flowing blood appears dark. When especially prepared pulses are used, flow effects cause strong intravascular signal loss. With mIP, better visualization of blood flow through the selected slice is obtained, allowing improvement in segmentation of cardiac myocardium from the bulk of the blood. mIPs are also used in SWI to render lesions and venous structures.

Multi-planar reformatting (MPR) is a 2D post-processing technique used to generate sagittal, coronal and oblique (or diagonal) views from axial sections.

The user usually defines three points of interest then a plane is drawn cutting through the body in the views selected (slicing). By rotating the 3-D dataset for different voxels (sometimes called data cubes), it is possible to focus on areas or regions of interest. Modern techniques allow computerized point selection and slice drawing (30). The imager can cut through different parts to unveil details of interest. Since 2-D projections are generated, MPR is usually combined with other post-processing tools to isolate and study in detail areas of interest.

1.3 Susceptibility Weighted Imaging (SWI)

1.3.1 Susceptibility

Magnetization is simply the magnetic polarization of a material produced by an arbitrary magnetic field. When a material is subjected to a static magnetic field it becomes "magnetized" and affects the surrounding area by a magnetic field distribution resulting from the newly arising magnetic dipole. Magnetization can be viewed as the amount of magnetic moment exerted by the magnetic field per unit mass or volume of an object, in this context bodily tissue or fluid.

The origins of the magnetic moments can be either microscopic electric currents resulting from the motion of electrons in atoms, or the spin of the electrons or the nuclei.

Net magnetization results from the response of a material to an applied magnetic field, together with any inherent, unbalanced magnetic dipole moments. Magnetization is not always homogeneous within an object. Rather, it is a spatial- or position-dependent quantity, where some areas might be highly magnetized while others are not).

The pre-described behavior depends on an intrinsic property of matter called magnetic susceptibility, χ (see definition above). The Magnetization, **M** (bold case for vector quantities), which arises due to the static field, **H**, is proportional to the susceptibility of the material:

$$\mathbf{M} = \chi\,\mathbf{H} \tag{1-7}$$

This linear relationship between **M** and **H** is common for paramagnets and diamagnets (such as water and most human tissues) (13).

1.3.2 Phase Imaging

To create an MR image, an immense number of MRI signal readings must be captured or acquired and processed before it is possible to create a resolvable image. This is because the same number of signal measurements is required as there are pixels (picture elements) in the phase encoding direction of the image to be created, which in turn comes from object voxels (volume elements or data cubes).

MRI signal measurement is repetitive in nature. As with the case of net magnetization variation and relaxation periods, measurement of the next signal might also be affected. Image reconstruction from MR data starts with the so-called Fourier transform. FT is a mathematical manipulation of the signal read out enabling its interpretation from time domain to frequency domain (k-space data to spatial signal distribution). FT allows determining the phase and frequency of the signal from each image element representing a net magnetization vector.

Phase images offer an additional source of contrast due to susceptibility differences. This phenomenon of magnetic field perturbations due to susceptibility

29

differences between different tissues leads to local variations in proton precession (oscillation) frequencies in the order of parts per billion. This results in localized variations in signal phase, which imposes additional contrast. The utilization of phase images in addition to magnitude images can lead to different contrast in the resulting images while preserving the more anatomically relevant information in the magnitude image.

In iron-laden structures, like different gray matter structures, creating these two images by SWI can add contrast to the object scanned, making the picture more resolvable (31). The same can be applied to any tissue with diamagnetic or paramagnetic properties differing from the background as in the cases of calcification and venous deoxyhemoglobin respectively. To prepare a readable phase image, a multi-step process is applied first to remove unwanted phase information resulting from static field variations, either inherent to the MRI magnet or due to major susceptibility changes at tissue to air interfaces (31,32). This problem can be solved using different techniques, including the utilization of a 2D high pass filter.

Phase images have been used for different applications such as mapping blood velocities (8), portraying veins (33) and measuring iron content in gray matter regions of the brain (34).

1.3.3 Acquisition of SWI

Susceptibility weighted imaging (SWI) has been introduced in (31,35) as a technique to utilize the contrast offered by phase images while overlapped on a magnitude image. This method has better anatomical feature representation and hence more usable for radiological purposes.

An SWI data set is obtained by scanning a patient or sample using a flow compensated gradient echo pulse sequence while preserving the full complex image after image reconstruction.

1.3.4 Reconstruction of SWI

The resulting image has to be processed to remove the wrap from the raw phase image (Fig. 1-3a and c), the associated slow phase variation resulting from static field variation and any possible shift of the k-space data central point. Different methods have been proposed to solve these problems. One of these is the removal of the slowly changing component by dividing the complex image by a low pass filtered version of the same image and hence obtaining the resulting flattened phase image (Fig. 1-3b and d). This method is essentially applying a high pass filter to the gradient echo complex image to obtain a filtered phase image. Figs. 1-3, 1-5, 1-6 and 1-7 show the experimental results of SWI techniques developed in-house using a 4.7 T Inova scanner (Varian, Palo Alto, CA).

A second method is using homodyne filters. First, the phase image is unwrapped using algorithms shown in (36). Next, a homodyne filter[*] or alternatively a high pass filter is applied to the unwrapped phase image. This leads to the same result obtained by the first method, except that the remaining wraps here look unwrapped[**]. Actually, this difference has no significant effect on obtaining any additional phase information. With this initial unwrapping, problematic areas still existed, because they have phase values outside the operating range of the masking function. These areas would look like being clipped by the masking function and appear in the SWI image as either completely black or as unchanged magnitude information. Fig. 1-4 shows a hypothetical phase profile with an illustration of this phenomenon[2]. The area of the image showing only magnitude information would look better in an SWI image, since wraps in the pure high pass filtering method would appear in the resulting SWI image. On the other hand, SWI image prepared by the unwrapping method would show no such wraps.

---

[*] The above referenced Homodyne filter does the same function as a High Pass filter but applying boxcar convolution (moving average window) to the image data. High Pass filter on the other hand uses multiplication of a selected filter shape with the frequency space image information.
[**] Verified by a comparison of 1) High pass filtering of the complex image and 2) Unwrapping the phase image and then high pass filtering the resulting unwrapped phase image.
[2] Hypothetical filtered phase information were formed by adding to arbitrary cosine waves of different frequency to simulate in-vivo phase information and then adding large slopes to both sides of the graph to simulate phase behavior close to tissue-air interfaces.

<center>TE=10 ms   TE = 10 ms</center>

<center>TE= 20 ms   TE = 20 ms</center>
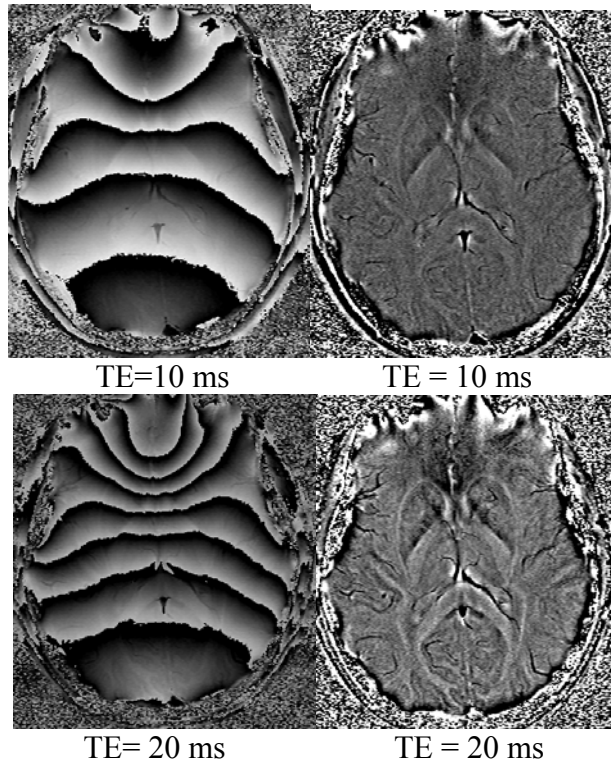
Figure 1-3: Phase images from 4.7 T susceptibility-weighted sequences with different echo times (TE). Raw phase and unwrapped/filtered phase images are shown. Echo time of 15 ms has provided high SNR and reduced phase wrap compared to TE of 20 ms.

An opposing concept would be to favor using the pure High Pass filtering method based on the fact that the wrapped area is marking the area in the image where no SWI contrast has been introduced. This would avoid the utilization of this area for any ROI measurements.

A third method relies on applying a polynomial filter/fit for unwrapping the phase image and subtracting the fit results from unwrapped image (37,38). This method would result in a significant difference from the high pass filtering approach due to differences in the mathematical algorithms being applied. Such differences will depend on the parameters of each method (filter width in the high pass filtering case and polynomial order in the relevant case).

<center>33</center>

To obtain good contrast from a phase/SWI image, a rod shaped voxel is preferred. In this case, the longer edge of the imaging voxel element is directed parallel to the static field. This entails the common practice in SWI of applying high in plane resolution and thick slices (39). Increasing the length along the field direction would increase the sensitivity in the resulting image to phase variation within the voxel because it has a coherent phase sign. In the extreme case where the longest edge of the voxel is laid perpendicular to the magnetic field, the phase sign could be completely reversed. This implies that phase cancellation and other erratic behaviors for voxels can happen when varying angles with the magnetic field. These effects are remarkable in heterogeneous voxels encompassing different tissue types, such as small veins as well as boundaries between different structures.
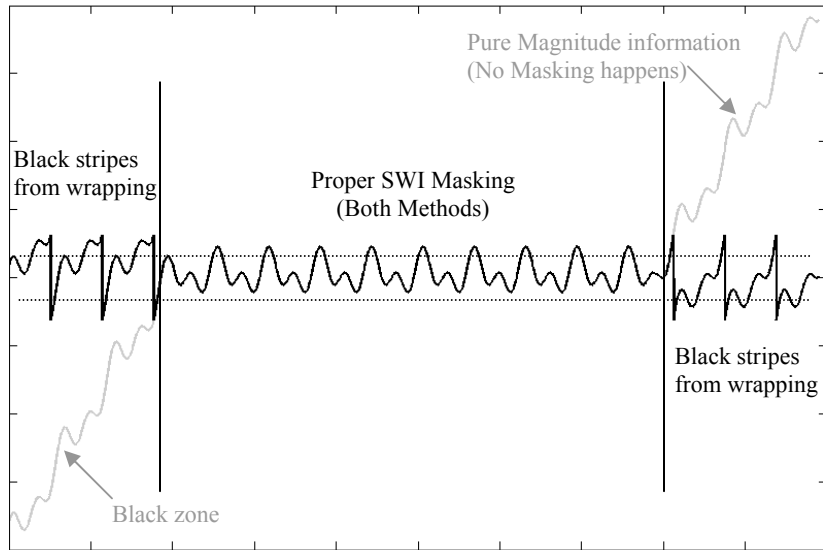
Figure 1-4: Hypothetical scaled phase information after applying the two filtering methods; High Pass Filtering in Black and unwrapping plus High Pass Filtering. The two approaches look the same in the middle segment while different in the outer segments. The outer segments show the area with filtering problems while the two horizontal lines show the upper and lower cutoff limits of the masking function. Phase values below the lower masking cutoff will be portrayed in the final SWI image as black while the values above the higher masking cutoff will be untouched by the masking process and hence will show as magnitude information.
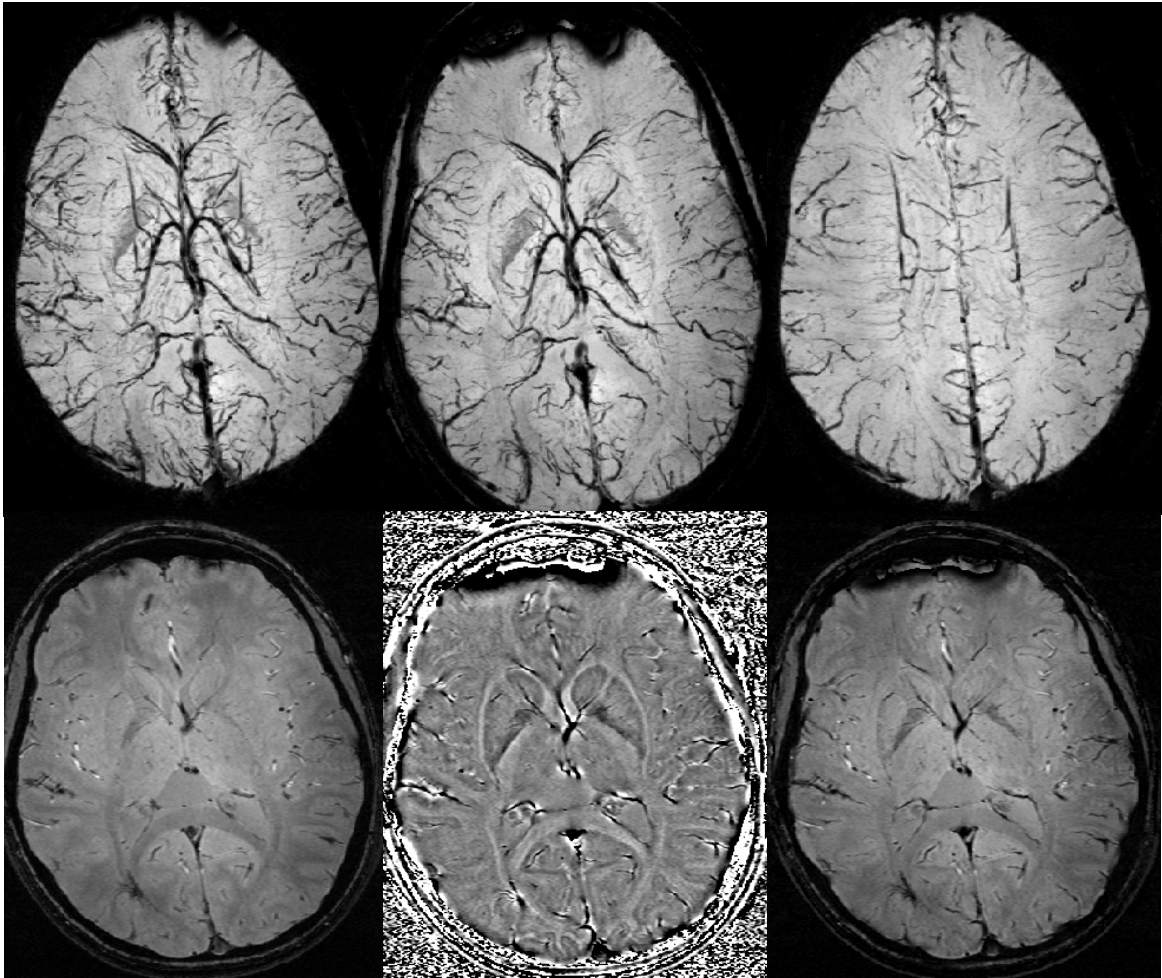
Figure 1-5 : Typical SWI technique for venous imaging at 4.7 T using whole head coverage via 2-mm slices of 2D SWI. Top row: minimum intensity projections from part of the data set show clear venous anatomy. Bottom row: a single source image from this dataset. Magnitude image (standard T_2* contrast TE = 15ms), processed phase, SWI. Note outstanding iron contrast in basal ganglia.

Caudate, GP, Putamen   Caudate, GP, Putamen

T$_2$* magnitude   phase image

GP, Putamen   SN and Red Nucleus

magnitude top,   magnitude top,
phase bottom   phase bottom
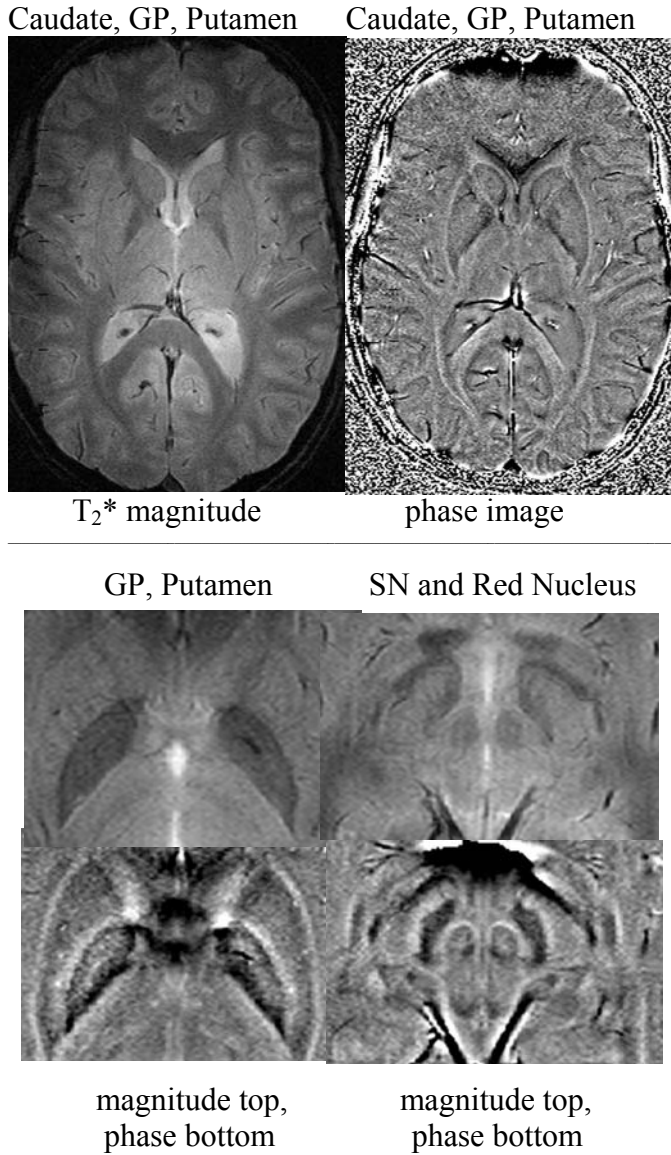
Figure 1-6: T$_2$* magnitude and susceptibility phase images from a healthy volunteer, illustrating different regions of the basal ganglia. A single Birdcage coil was used for transmission and reception in this case, so there is a visible loss of signal as one moves away from the centre in the magnitude, but the phase image is immune to RF variation.
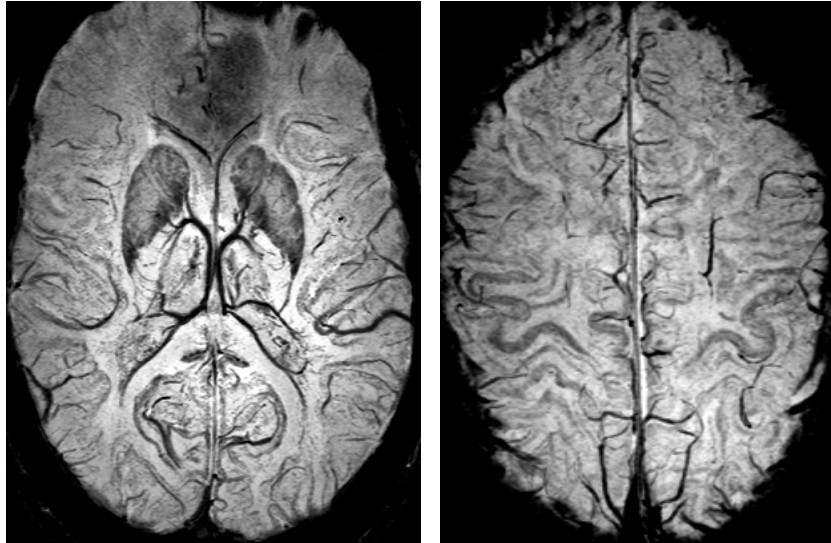
Figure 1-7: Maps of iron and venous vessels through minimum projections of SWI images from 4.7 T. At left note Globus Pallidus and Putamen. At right, note darkening in motor cortex due to increased iron content.

As outlined above, a main challenge facing SWI is the need to acquire this image axially (or at least making sure that the imaging voxel is aligned with the static field (39)).

This results from the manner in which the field perturbations arise around a magnetic dipole aligned with the main field where a rectangular area aligned with the dipole will have a pattern of phase/field summation drastically different from the same summation when applied to a rectangular area that has a non-zero angle with the dipole direction (39)[3].

---

[3] This concept is further discussed in the introduction to Chapter 3.

It has been the tradition since inception of MRI that the read out direction and slice selection/slice encoding direction have to be orthogonal to each other (22).

In the current work, this concept is challenged and the unlocking of both directions will be introduced, allowing such directions to have free angles (i.e. independence). The application of this invention is also introduce, which allows axial acquisition for SWI while being able to image oblique slabs or slices.

1.4 Time of Flight Angiography (TOF)

As explained before, MR TOF angiography is an imaging method that depends on visualizing blood flow. Blood filled structures, such as arteries and veins can be distinguished from surrounding structures by the nature of blood flow rather than displaying vessel walls.

Blood movement would affect the method, which relies on the movement of blood to affect more M_Z saturation to the stationary tissues than to blood which by virtue of its flow, is in a more "fresh" magnetization state as it continuously enters the imaging area.

The conception of this idea began first by noting that flowing water has an apparent T_1 relaxation constant shorter than that of stationary water. This was followed through to being applied to blood imaging (1-4,40).

Transverse magnetization depends on both longitudinal magnetization of the sample and its transverse relaxation time as follows (any consistent set of units apply):

$$M_{XY} = M_Z . \sin\alpha . e^{-t/T_2^*} \qquad (1\text{-}8)$$

Where

t : Time since last excitation

T_2^* : Transverse relaxation of the sample for gradient echo sequences.

M_Z : Longitudinal magnetization

M_{XY} : Transverse magnetization

α : Excitation flip angle

As blood enters the selected imaging volume it is in resting state and gets subjected to a less number of excitation events than the background/stationary tissue. The blood magnetization after **n** RF excitations is described by:

$$M_Z(n) = M_o - \left(M_Z(n-1).\cos\alpha - M_o\right).e^{-TR/T_1} \qquad (1\text{-}9)$$

$$M_{XY}(n) = \{ \left[M_Z(n-1) - M_o\right] e^{-TR/T_1} + M_o\} \sin\alpha \qquad (1\text{-}10)$$

M_o : Magnetization in resting state

TR : Sequence repetition time

T_1 : Longitudinal relaxation time

n   : number of RF pulses experienced by blood volume

This leads to a decline in the blood signal with higher "n". The decline depends on blood velocity component in the slice selection direction as well as slice/slab thickness. The saturation of blood magnetization was studied by (41,42).

The stationary tissue signal is known by the Bloch equation for steady state conditions. It shows the basis for relative signal from the background voxel after many RF excitations (steady state case):

$$M_{XY} = \frac{M_o\left(1 - e^{-TR/T_1}\right)}{1 - \cos\alpha . e^{-TR/T_1}} \sin\alpha \qquad (1\text{-}11)$$

Where M_{XY} is the transverse magnetization, α is the excitation flip angle, M_o is the resting state magnetization of the voxel and TR is the repetition time of the pulse sequence (22). The former equations ignore the T_2^* relaxation term for the assumption of a very short echo time.

At the beginning of a TOF experiment, both tissue and blood have full resting magnetization and both experience M_Z saturation with further excitations. Assuming a T_1 relaxation for blood of 1500 ms and for background of 1200 ms, we can see the decline in both M_Z and M_{XY} for both materials along the course of the experiment. This simulation is shown in figure 1-8 for a typical experiment (α or flip angle is 25º and TR or repetition time is 36 ms.)
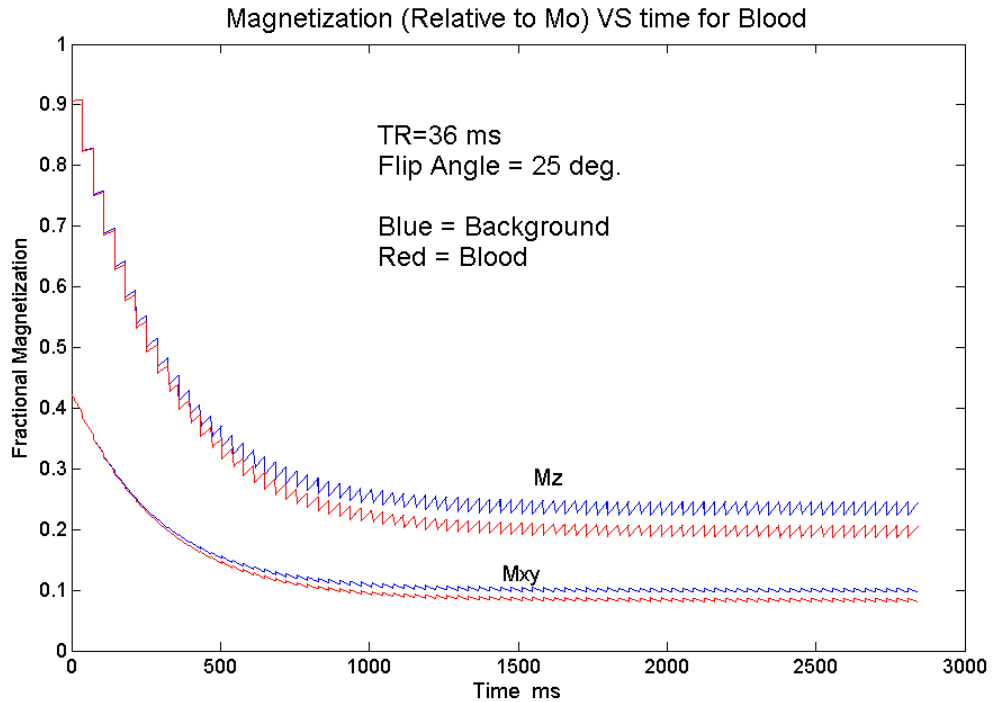
Figure 1-8: showing the M_Z and M_{XY} (as labeled) for assumed stationary background tissue and blood samples with $TR = 36$ ms and $\alpha = 25°$ being the average of a ramped excitation pulse.

Since the in-vivo blood is continuously flowing, it keeps entering the bottom of the slab (in the case of intracranial arterial blood) with no prior RF excitation. Hence the magnetization curves for blood can be shown to start at a later point in time than those of the background (Figure 1-9). As a result, a time window will appear, where blood will have a significantly higher signal than the background (figure 1-10). The width of the window time depends on the SNR of the experiment, where higher SNR can extend the window to just before the limit where blood and background have the same signal. Under the current simulation parameters, this time window can be 0.4 – 0.5 seconds (with a top limit of 0.8 seconds for very high SNR), meaning that blood cannot stay longer than this time in the imaging slab if a full image of blood vessel lumen is to be obtained.

As there is little control on blood speed, the imaging parameters (i.e. slab thickness, flip angle, ramp pulse and *TR*) must be adjusted accordingly. Figure 1-11 shows the same concept for relative blood to background contrast. Here the contrast level intersects the abscissa when blood and background have the same signal levels. By implementing the above concepts to minimize background tissue signal while maintaining blood signal high enough, a good visualization of blood vessels is possible as shown in figure 1-12 which shows a MIP of the intracranial arteries at 3.0 T.
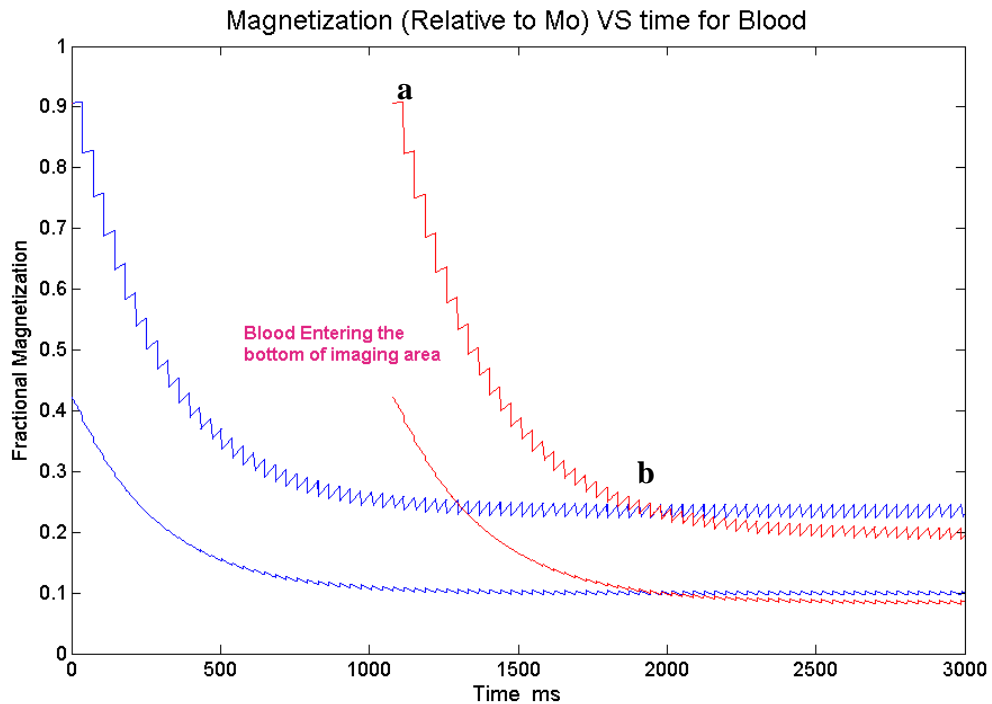
Figure 1-9: As blood enters the imaging slab at an **arbitrary**[4] later point of time (a) it has higher magnetization and signal than the background for a certain period of time ending at (b).

---

[4] A common practice is running several "dummy" scans where all experimental events occur except that no acquisition happens to give the background tissue enough time to reach its minimal signal level at steady state.
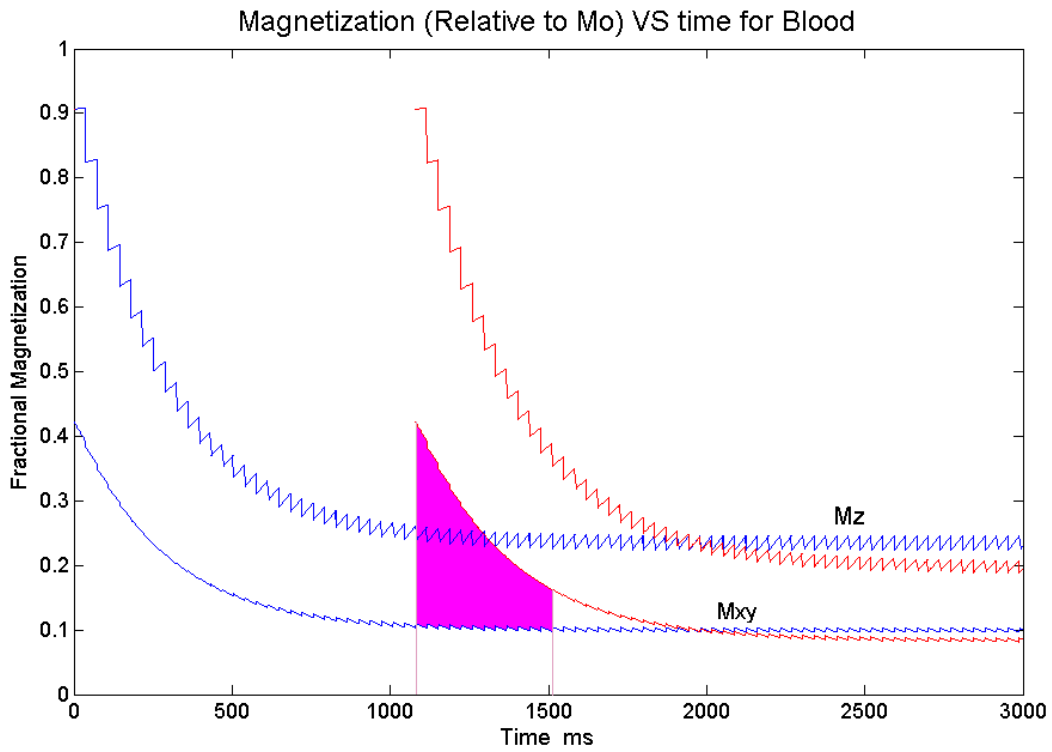
Figure 1-10: Magnetization response from blood and background. The response is affected by blood flow, which effectively maintains fresh magnetization as it enters the imaging slab. The color-shaded area refers to the expected case of blood signal being significantly higher than that of background (actual width of this area depends on SNR in the experiment).
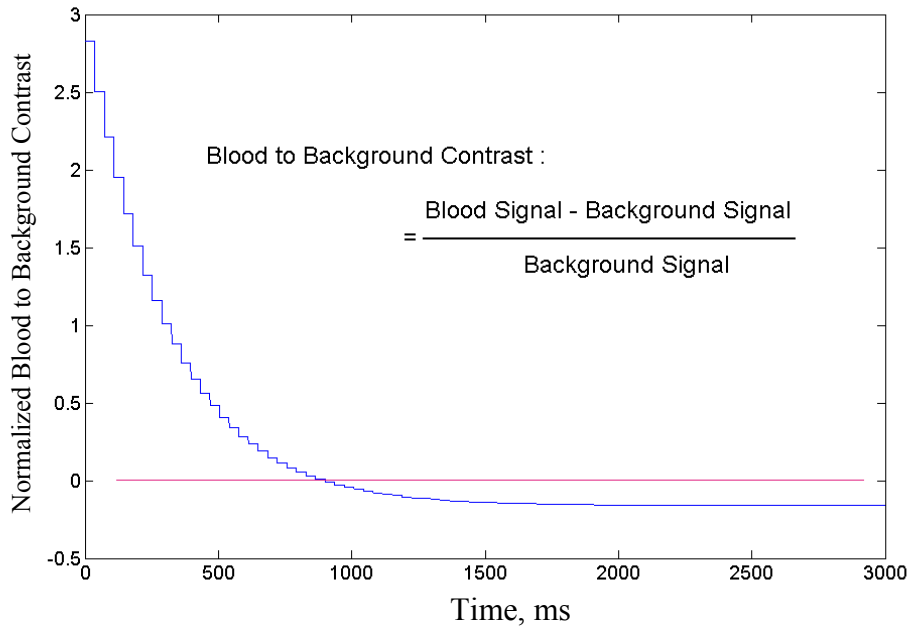
Figure 1-11: Relative blood to background contrast (dimensionless) estimated when blood first enters the imaging slab while background is held at its steady state. Imaging parameters are the same as in previous figure.
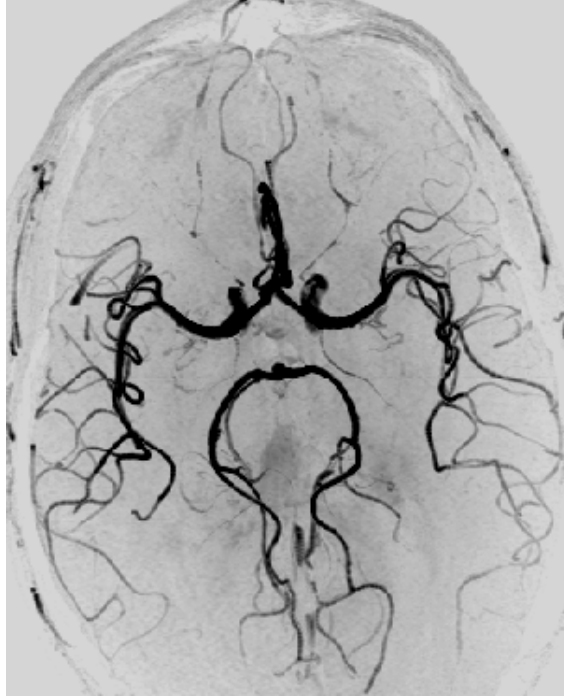
Figure 1-12: A maximum intensity projection MIP from a 3D-TOF scan of a healthy volunteer at 3.0 T.

1.4.1 Flow Compensation;

As blood moves during an imaging experiment, it experiences various gradient levels associated with the different spatial locations it passes through within the period of the applied gradient. This variation depends on gradient levels as well as blood flow rate (or velocity) and leads to compounded effects resulting from the erroneous[5] phase accumulation experienced by the blood sample. As a result, it is possible to have misregistration, which can take different forms. For example, blood signal can assume different location(s) than the real one or ghosting artifacts caused by blood flow pulsatility might happen. In addition, it might lead to reducing the blood signal whenever different

---

[5] This phase accumulation is considered erroneous when the imaging method is depicting blood/tissue signal and spatial location. However, in cases like Phase Contrast imaging, the pulse squence might be designed to utilize this kind of phase changes as a source of beneficial information (nref32,33).

components of the same voxel acquire different phase values (resulting from different speeds within the same voxel). Moreover, unwanted phase values might emerge, which can adversely affect any relevant phase imaging process, as it is the case with SWI.

To overcome these effects for the case of constant blood velocity and to lessen the problem with pulsatile flow, an additional gradient lobe is added to both read out and slice selection gradient set. This will achieve not only zeroth moment nulling, but also first moment nulling. These moments are represented by the following equations:

$$0^{th} \, Moment = \int_{0}^{\tau} G(t).dt = 0 \tag{1-12}$$

$$1^{st} \, Moment = v\int_{0}^{\tau} t.G(t).dt = 0 \tag{1-13}$$

Here t defines the time from the beginning of read out gradients until the echo point (expected peak of acquired signal) and also defines the time from the RF excitation peak until the end of slice selection gradients on a separate channel. Fig. 1-13 shows the case of trapezoidal flow compensation gradients applied for read out and slice selection. The symbols on Fig. 1-13 define the nomenclature of timing parameters as well as gradient heights. The same parameters will be used in subsequent work.
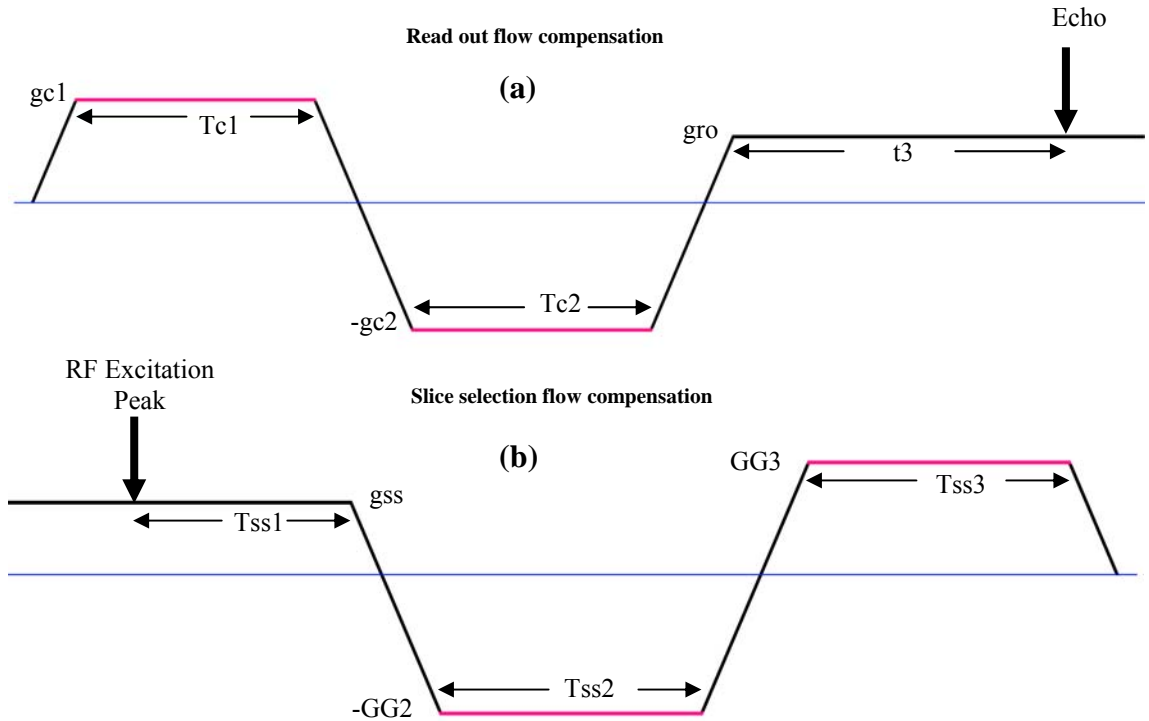
Figure 1-13: Schematic representation of trapezoidal flow compensation gradients for **(a)** Read out channel and **(b)** slice selection channel. The terms gc1 and gc2 represent the read out flow compensation gradient magnitudes while gr0 represents the read out frequency encoding gradient. The term t3 is flat gradient duration until Echo time. Terms Tc1 and Tc2 denote the flat gradient durations of gc1 and gc2 respectively. Slice selection gradient is noted by gss, while slice select flow compensation gradients are noted by GG2 and GG3. Tss1 is the flat gradient duration starting at the peak of the RF Excitation pulse. Terms Tss2 and Tss3 represent the flat gradient duration corresponding to GG2 and GG3, respectively.

To apply flow compensation gradients, the waveforms illustrated above are needed. Basically the method includes the addition of an extra gradient lobe at the beginning of the read out gradients and at the end of the slice selection gradients.

Numerical methods can be used for gradient moment nullifying (9). Different gradient strengths and/or durations can be recursively optimized by trial

47

and error until a zero moment parameter set is reached. The set can further be optimized for gradient solutions with shorter times if minimal TE is needed.

Trial and error technique has an inherent weakness, since any change in relevant parameters will entail repeating the tedious iterations. Any change in the height or duration of read out or slice select gradients will need re-estimation of the flow compensation gradients parameter set depending on the changes in experimental conditions. In other words changes in spectral width, slice thickness and other parameters will obligate such re-estimation. Finding an analytical solution to be used within the pulse sequence would be more convenient and in some cases, may be required.

1.4.2 Read out and slice selection flow compensation: A pulse sequence programming oriented analytical solution

The following work has been implemented using "Inova" MRI Consoles at 3.0 and 4.7 T fields (Varian, Palo Alto, CA) as part of 2D and 3D gradient echo pulse sequences. Read out and slice selection flow compensation waveforms were added with the capability of maximum optimization for shortest possible echo times.

An analytical solution was proposed by Bernstein (43, 44), which includes simple/concise equations as an analytical solution. The suggested solution, however, produced "area of trapezoidal lobes" as variables in the final solution. If direct pulse sequence programming is needed, it is preferable to use the simplest possible parameter inputs from the pulse sequence program without elaborate

preparation. By this, the equations will be user-friendly (or rather, programmer friendly) and can solve for flow compensation parameters.

In this work, the gradient waveform was represented by a series of linear functions starting at base time (i.e. t = 0) at the beginning of the read out gradients as well as at the middle of the excitation pulse. Each linear equation was then defined in terms of its gradient values as well as its time limits.

The sum integrations for both moment functions were estimated and the same was repeated for the gradient functions, G and $G\ t$. The integration yielded two equations for the zeroth and first moment quantities. The two equations were solved simultaneously for the time variables, which control the duration of the flow compensation lobes (the two flat gradient delays Tc1 and Tc2 in the read out case and Tss2 and Tss3 in the slice selection case), while assuming all other parts of the equations are constants. In-house Matlab software was used to find the required solutions.

The resulting equations are fully stated in Appendix 1. The variables involved are defined below. They were also verified numerically by solving for several hypothetical cases and estimating the resulting zeroth and first moment results. The resulting nulling in the simulated moments verified the correctness of the solutions reached. This method has also been used successfully for TOF as well as SWI pulse sequences.

Dependent Variables:

The following four timing variables represent the flat area of the corresponding

flow compensation lobe:

Tc1   = First lobe Read Out

Tc2   = Second lobe Read Out

Tss2   = Second (right after the pulse) lobe Slice Selection

Tss3   = Third (last) lobe Slice Selection

Independent Variables: controlled by user and/or experimental setup

gc1   = first lobe Read out (gradient value)

gc2   = second lobe Read out (gradient value)

grate   = trise/gmax;   (trise = time needed for the gradient to reach from 0 to

            gmax, while gmax = maximum gradient value of the specific system.

            Note: grate = 1/(slew rate))

gro   = read out gradient

t3   = time from the start of flat read out lobe until the echo point (half the time

            parameter 'at' for full read out case)

GG2   =flow compensation gradient of the second lobe (middle one) for Slice

            selection

GG3   =flow compensation gradient of the third lobe (last one) for Slice selection

Tss1   = time from the peak of excitation pulse (middle for a symmetric pulse)

            until its end.

gss   = Slice Selection Gradient

Setting Flow Compensation gradient values:

– The user selects the gradients

– When minimal echo time is needed, solution is through applying higher flow compensation gradients. It was noted that doing so to the middle lobe (more than the remaining flow compensation lobe) of both flow compensation patterns is more effective at reducing flow compensation time.

– The setup assumes trapezoidal gradient waveforms rather than triangular waveforms. It should be noted that too high gradient values could result in erroneous negative delay values (error verification/checks or user vigilance is required).

Initially the two sets of equations were solved independently for either case. As such, the formulas were different. Later, the integration of either case was the same whether it was computed from left to right or in reverse.

The two sets of equations can be used interchangeably (by using Tc1 in place of Tss3, Tss2 ➜ Tc2, Tss1 ➜ t3, gss ➜ gro , GG2 ➜ gc2, GG3 ➜ gc1, and so on). Parameter swapping sequence was confirmed by numerical simulation, where both equations have been used interchangeably and results obtained were correct. Appendix 1 contains the complete formulation of the flow compensation equations. The two equations were successfully validated for several input parameter values.

Figures 1-14 and 1-15 show the time overhead estimated due to flow compensation gradient set as a function of flow compensation gradient heights.

The case presented refers to read out flow compensation with read out gradient of 0.8 Gauss/cm, rise time (from zero gradient to maximum system gradient) of 500 ms, gmax (maximum system gradient) of 6 Gauss/cm and t3 (time from beginning of acquisition until echo) of 2.56 ms.

The overhead time is estimated according to the following:

$$TRO=grate*gc1*2+grate*gc2*2+grate*gro+Tc1+Tc2; \qquad (1\text{-}14)$$

(read out case)

$$TSS=grate*GG2*2+grate*GG3*2+grate*gss+Tss2+Tss3; \qquad (1\text{-}15)$$

(Slice selection case)

Increasing the first lobe gradient and/or second lobe gradient always results in a shorter overhead time. A limitation of system gradients always exists, caused by heating and duty cycle constraints, which are dependent on the specific system. Therefore, in some cases, it is advised not to use the maximum gradients. Inspection of these two figures shows that it is more efficient to utilize further increase in the second gradient lobe height than in the first gradient lobe height to reach the desired shorter echo time.

Fig. 1-14 shows the effect of first gradient lobe height for different values of the second lobe height, while Fig. 1-15 shows the effect of second gradient lobe height for different values of the first gradient lobe. It can be seen that increasing either gradient lobe height would result in a shorter overall time.
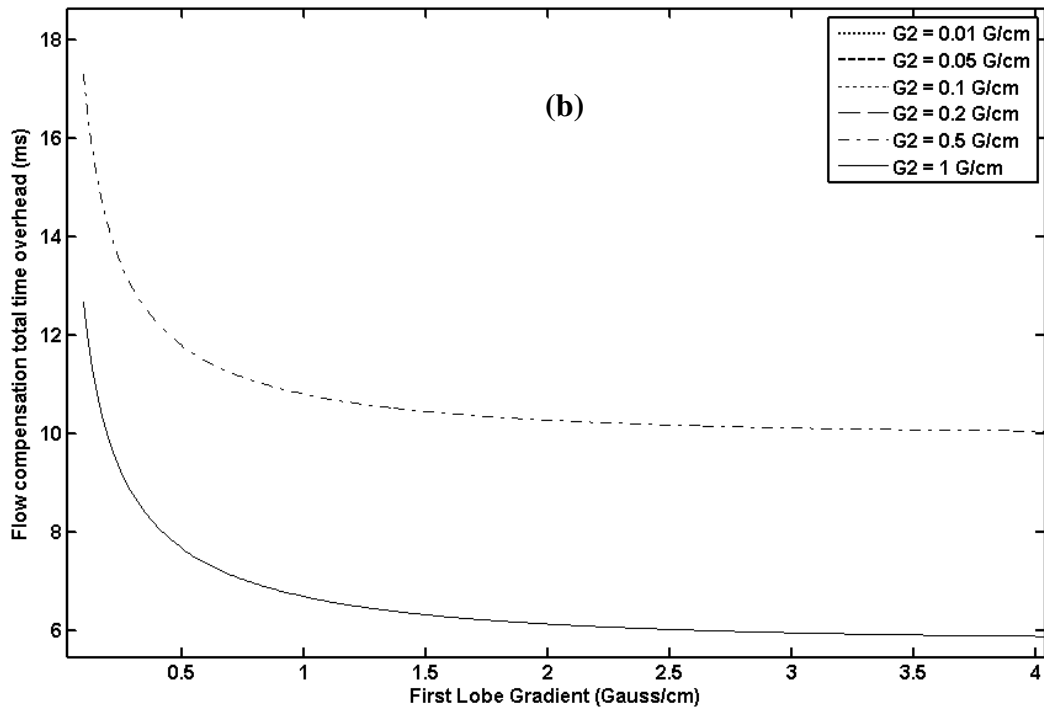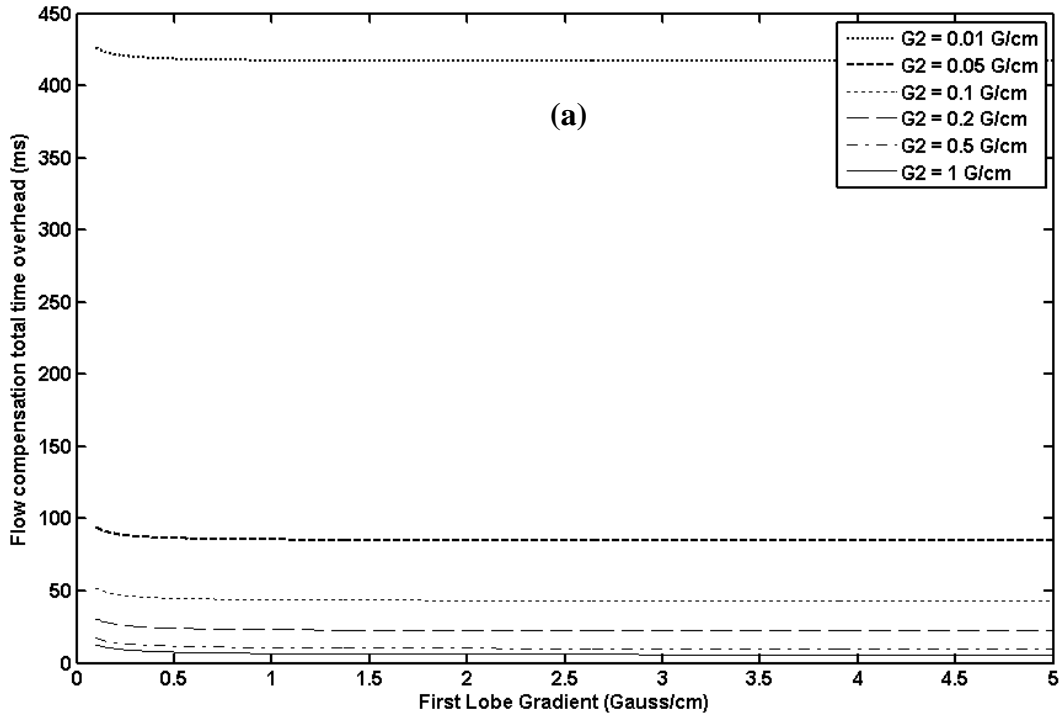
Figure 1-14: Effect of varying the first read out flow compensation gradient on the total time of read out flow compensation gradients for different values of the second lobe of the same flow compensation waveform. The graph in (b) is a zoom in from the graph shown in (a).
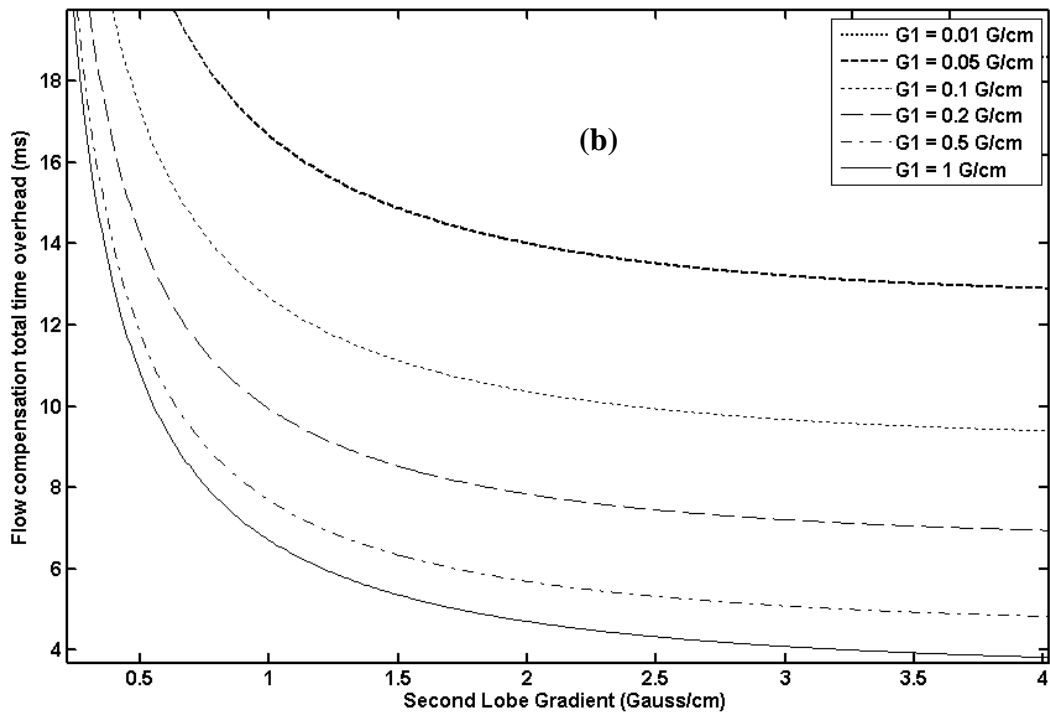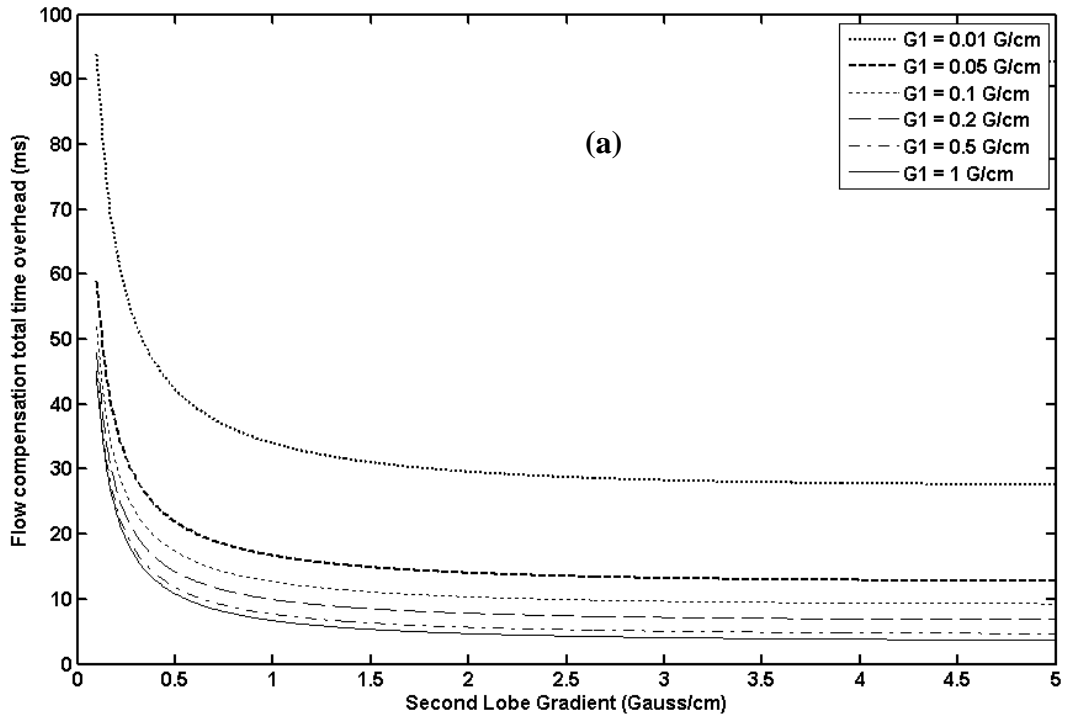
Figure 1-15: Effect of varying the second read out flow compensation gradient on the total time of read out flow compensation gradients for different values of the second lobe of the same flow compensation waveform. The graph in (b) is a zoom in from the graph shown in (a).

54

1.4.3 Venous Suppression Using Spatial Saturation

For better visualization and for proper diagnosis of vascular pathology, separate imaging of arteries or veins might be needed. To do so, a saturation pulse is applied on the proper side of the imaging slab (5,45). A 90 degrees pulse is applied every TR. The resulting transverse magnetization is spoiled by a crusher gradient lobe, which leads to selective suppression of the longitudinal magnetization for either arterial or venous blood. In the case of intracranial venous suppression, a saturation pulse is placed above the imaging slab to suppress signal from the downward flowing venous blood. This leads to a purely arterial scan.

A recommended practice here is to apply a thick saturation pulse to effectively deliver as many saturation pulses as possible to the venous blood before it enters the imaging slab. It is also recommended to apply a gap between the saturation volume and the imaging volume so as to avoid any saturation in the imaging area itself.

1.4.4 Ramped RF Pulses

In 3D-TOF, as blood traverses the thick imaging slab, it encounters several excitation pulses with the exact number of pulses depends on blood velocity and the excitation slab thickness. This can lead to poor blood signal at the end of its path through the slab and hence the possibility of complete loss of contrast with the background. A linearly ramped RF pulse frequency profile has been previously introduced (6) with flip angles lower at the beginning of the blood pathway to minimize blood saturation. Higher flip angles were

progressively introduced until the end of blood pathway, where the highest flip angle extracts the highest possible signal from the blood as it leaves the imaging volume.

The time domain presentation of a ramp pulse is shown in Fig. 1-16 while the frequency domain (k-space data or spatial flip angle profile) is shown in Figure 1-17.

Using a ramped RF pulse resulted in more stable blood signal across the imaging slab (7). This variation of flip angle across the imaging slab leads to different steady state background signal levels, which might harm the MIP visualization of the resulting image.

It is worth mentioning that this variation of background signal goes hand in hand with the possible variation in blood signal, where the background is most suppressed at the end of blood pathway (i.e. where blood signal might be at its weakest level). This suggests that the blood to background contrast can be in a good condition, suggesting an alternative image presentation technique to the MIP method. In Chapter 4 more discussion is given for the method of ramped excitation pulses along with detailed presentation of various experimental results.
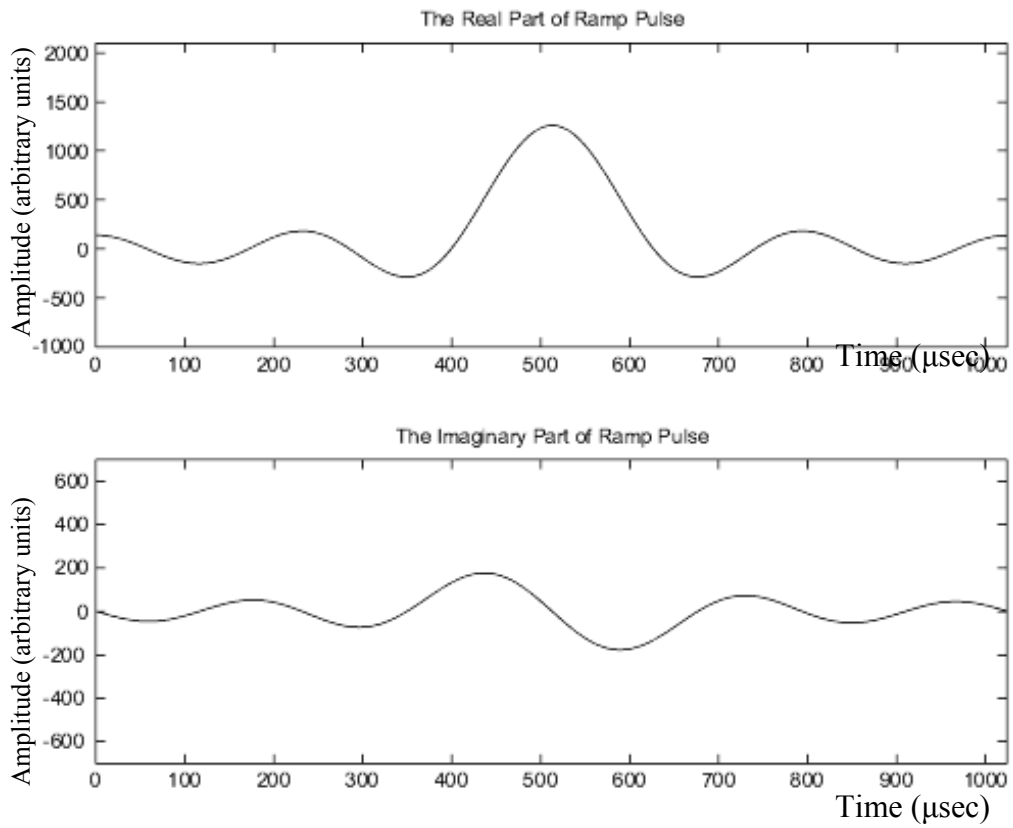
Figure 1-16: RF Ramp Pulse. Time Domain representation of an example ramp pulse with a length of about 1msec.
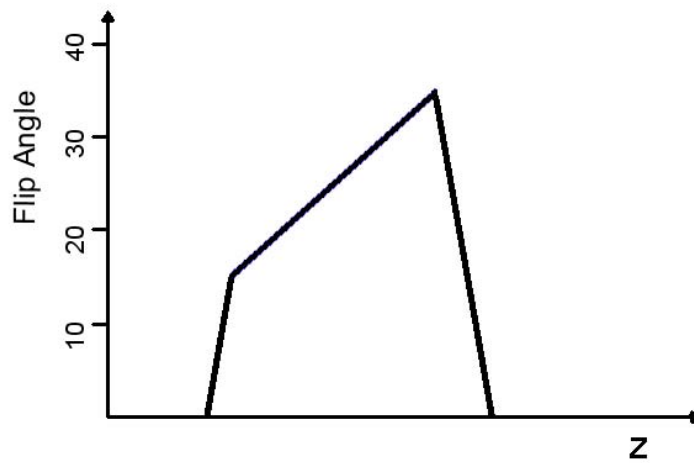
Figure 1-17: Frequency profile (k-space data) of a ramped excitation RF pulse. Flip angle run at the typical slope from 15º to 35º for an average flip angle of 25º.

1.5 High Field Considerations

One major area of advancement in MRI is using a higher static magnetic field with vast opportunity for faster, higher imaging and spectroscopic resolutions, and/or higher contrast imaging. There are evidences that higher field strengths improve chemical shift dispersion, susceptibility, and related BOLD (blood oxygenated level dependent) contrast (46).

The radio frequency (RF) coil is an essential element in MRI systems. As indicated above, it is a device used to transmit and receive the electromagnetic field variations to and from nuclei, such as protons at the nuclei specific Larmor frequency. In addition to obvious increases in the stored energy of the stronger magnet, difficulties in fabricating suitable RF coils also mount with the increasing system frequency.

One of the MRI problems at higher frequencies (associated with high field intensity) is the emergence of complex engineering design issues. Examples of these issues are the design of safe, reliable and versatile RF coils that have high performance and can be easily integrated with new MRI hardware. There are also other physical limitations or problems to imaging high field MRI, including RF penetration, RF power requirements, dielectric focusing and dielectric resonance effects (47).

High field MRI systems require high frequency RF coils and coil sensitivity could be compromised. Re-calibration or re-tuning implies that the imaging process will become time and resource consuming. Though could be

alleviated by digital control and sophisticated computing algorithms, it is an issue that needs to be addressed.

Moreover, at high magnetic fields (greater than 3 T), the performance of the RF coil becomes increasingly dependent on its interaction with the human head/body. As the resonant frequency increases with field strength, the dimensions of the RF coil and the human head/body sizes are no longer negligible relative to the operational wavelength. To solve this problem and design better and more efficient coils, electromagnetic modeling is needed.

High field MRI also presents us with few important challenges as we push the limits of RF heating in some cases and that of RF inohomogeneity in most cases. Also, valid concern arises around the utilization of extra RF power for magnetization transfer and spatial saturation (48).

This in turn raises a question about the best field for the current MRI technological state of the art. Such field should be high enough to reap the above mentioned benefits but also should still allow the majority of MRI techniques to function and yield results that in some cases are as good as lower field results at the least.

Research studies will likely confirm the clinical utility of higher field strengths, say 3.0 or 4.7 T, against the classical 1.5 T. Published studies show not only effects on signal-to-noise ratio, contrast-to-noise ratio, or even diagnostic sensitivity and specificity, but also effects on diagnosis management, and ultimately, effects on patient outcome (49).

The longer T_1 relaxation times of brain tissues (50) offer higher background suppression in the case of TOF, which could allow better blood visibility. Some pulse sequences "appear" to be significantly limited as the field goes higher than 3 T, such as fast spin echo (FSE).

The standard 1.5 T clinical MRI, for example, uses an RF coil, such as the birdcage resonator, which is usually driven in quadrature (2 port) for head and whole body imaging. The resonance frequency for the 1.5 T systems is about 64 MHz for proton imaging. As mentioned earlier, the goals of the coil design at this RF frequency are to produce uniform, circularly polarized magnetic field gradients (to ensure homogeneous excitation) and have low values of the specific (energy) absorption rate (SAR). At such frequency, these goals are easily achieved.

At higher magnetic field strengths, the higher operating frequency makes achieving the previous two goals somewhat difficult. As such, redesigning the RF coils might be essential.

New designs of imaging coils were proposed for usage in high field MRI, which include changes in the physical parameters of the coil components or resonator (length, inductance and capacitance, to name a few), with the aim of reaching a well-distributed magnetic field (47).

One of these designs is the transverse electromagnetic (TEM) resonator. The TEM resonator is simply a transmission line resonator filled with non-discrete lumped capacitive and inductive tuning elements. The resonator has a thin coaxial cylinder fitted with tiny rods (struts). The assembly is surrounded by

a continuous copper sheet (to serve as a conductor) and filled with a low dielectric material. In operation, the rods slide closer or farther apart to change the impedance of the transmission line and tune to the desired resonant frequency.

There are several designs for the TEM, where 8-, 16 and 24-struts have been used (Figure 1-18). The TEM resonator has several advantages over the birdcage coil in terms of improved magnetic excitation, more homogeneous magnetic field and sharper contrast, as well as less significant drop in SNR.
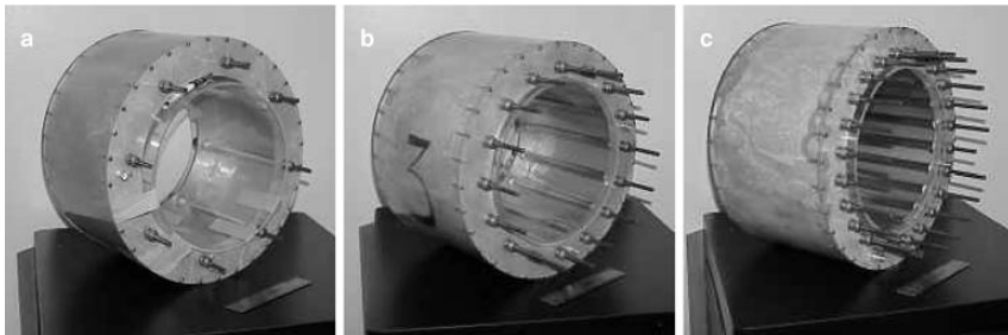
Figure 1-18: TEM Resonators with 8 (a), 16 (b) and 24 (c) struts *(51)*.

Another design is the phased array coil (PAC), sometimes called multi-coil array. It is essentially a number of overlapping surface coils (or elements), each with their own receiver detection circuitry. The PAC is used to increase the surface area acquired whilst maintaining the SNR obtainable with a single surface coil. One example is the 4-channel phased array body coil. The acquisition in each coil/element takes place simultaneously too, so no increase in acquisition time is endured.

The multiple coil nature of the phased array coil is used in parallel imaging strategies such as SMASH (Simultaneous Acquisition of Spatial

Harmonics) and SENSE (Sensitivity Encoding). SENSE uses the additional information captured by the sensitivity map of each coil to allow fewer lines of the frequency domain to be acquired. This approach speeds up the scanning, although a trade-off of SNR occurs.

This design can improve the performance of RF head coils in terms of transverse magnetic field uniformity and reduction of specific (energy) absorption rate. In essence, the PAC increases the SNR gains (22,52,53) by their sensitive reception at the edges of the scanned object, say the brain. However, deeper brain structures suffer from rapid decline in SNR due to their further location from the reception coils. These structures are where SNR gain from higher fields can prove significantly beneficial.

1.5.1 Specific (Energy) Absorption Rate (SAR)

The radio frequency energy from an imaging sequence can cause heating of the tissues of the body. The USFDA recommends that the exposure to RF energy be limited (54). The specific absorption rate (SAR) is the limiting measure. It is an indicator of the rate of energy disposed per patient weight (mass, more accurately)

SAR = Joules of RF energy per second (Watts) / kg of body weight $\qquad$ (1-16)

The recommended SAR limitations depend on the anatomy being imaged. The SAR for the whole body must be less than 4 W/kg. It must be less than 3.2 W/kg averaged over the head.

Any pulse sequence must not rise the temperature by more than 1º C and no greater than 38º C in the head, 39º C in the trunk and 40º C in the extremities. As expected, the amount of energy deposited to the patient body is proportional to the Radio frequency utilized. High magnetic fields require high frequency coils, which means that more energy is needed and will be deposited.

At high field strengths, specific (energy) absorption rate SAR increases, which has some consequences. The guidelines for safe MRI are meant to minimize the risks of damage to body tissue. Usually, energy deposition limits are stated in Watts of RF power per kilogram of tissue. As mentioned earlier in this chapter, these limits impose a specific absorption rate of RF energy, to reduce any heating effects. The USFDA regulations put different limits on SAR for the whole body and other parts individually.

In clinical MRI, doubling the magnetic field strengths produces a four-fold increase in SAR. The current range for field strength is 0.2 to 3.0 T. If ultra-high field strengths of, say, 11.7 T are to be used, SAR becomes a more serious issue.

These limitations on allowable SAR mean that patient exposure to magnetic fields is constrained and different consequences might arise, such as running the scanning for longer TR times, poorer coverage or scan quality from pressure to finish the scan quickly, longer RF pulse durations, lower flip angles or a combination thereof.

A number of SAR management features are applied in modern MRI magnets to maintain consistent pulse sequence parameters and obtain quality images. Depending on the manufacturer, these can include: optimized body coil

design, a priori knowledge of energy deposition throughout the body and anatomy-specific dynamic SAR limits. Coil design may be the most important feature (49).

1.5.2 Signal to Noise Ratio

At high field strengths, scan times can be significantly reduced, while more improvement in image resolution is attainable, largely due to increased signal-to-noise ratio (SNR) (55). Most capital spent to acquire stronger MRI magnets is to improve the realized SNR, which scales linearly with the magnetic field strength at higher values (22). But increased RF frequencies are associated with RF inhomogeneity effects, as mentioned previously, rendering SNR itself spatially variable.

The SNR gains from high field MRI can be utilized for yet unexplored areas of medical research. The possible high-resolution images can be used in studying neurological structures, such as small, deep brain structures, and for pathological applications, such as perivascular diseases where pathology is related to smaller vascular structures. However, caution is needed with possible excessive increases in scan time in which case SNR can be traded for faster imaging by parallel imaging and scanning parameter adjustments.

The MR signal induced in a receiver coil is proportional to the square of the magnetic field strength. Noise however, is directly proportional to the field strength in the range above 1.0 T. This theoretical SNR increase with the field is not normally fully realized in vivo. In practice, SNR gains meeting the full

theoretical expectations are only realized in certain tissues/areas (e.g. cerebrospinal fluid) (12).

High field induces proportionally higher susceptibility effects. Therefore, stronger local magnetic field variations result on the microscopic scale leading in turn to greater spin dephasing. This can ultimately lead to shorter T2 and T2* values. Concurrently, recovery time of longitudinal magnetization (T_1) increases. With the constraints of maintaining reasonable scan times, many pulse sequences must run at lower flip angles rather than increased TR which leads to lower SNR.

SNR increases are by far the most important gain realized by utilizing higher fields which leads to more diagnostic benefits in clinical practice. Such benefits include, better image sharpness, higher spatial resolution and/or higher temporal resolution. Although SNR at 3.0 T is not necessarily 2 folds that at 1.5 T, yet a scan at the former field should yield a SNR comparable to or better than 2 averages at 1.5 T (hence achieving 2 fold increase in temporal resolution).

A technique that normally produces low signal or small effects is most expected to benefit from higher SNR (e.g. fMRI based on the BOLD effect). As parallel imaging techniques can result in lower SNR due to the associated reduction in scan time, increased SNR can bring parallel imaging methods closer to realizing their full potential. (56).

As discussed above, longer T_1 relaxation times at higher fields require changes to pulse sequence parameters. Hence, a pulse sequence parameters set cannot be simply transferred from a 1.5 T system to a 3.0 T system. To preserve the optimum or expect tissue contrast, a longer TR or smaller excitation flip angle

is needed. This can also affect the extent of coverage achievable at the higher field (57).

1.5.3 RF Phenomena at High Field

While SNR is directly proportional to the field strength, RF heating is proportional to the square of RF frequency or field strength. For RF intensive applications, the quadratic climb of RF heating will inevitably set a limit on the maximum field that can be utilized (58) while maintaining feasible implementation and efficient imaging techniques let alone capitalizing on the SNR gains. Such applications include fast spin echo imaging (59), spin echo imaging, magnetization transfer and spatial saturation to name a few. One way to try solving this problem is by changing the MR application design in a way that reduces its RF emissions. One such approach is presented in chapter 5.

Another complication arising at higher fields is RF inhomogeneity, resulting from the shorter RF wavelengths which in turn cause destructive RF interference and RF field focusing (60-67). At 4.7T, the RF wavelength becomes comparable to the head dimensions (about 20 cm) and the edge of the brain receives as much as 40% less excitation angle than planned in the experiment (68). The same effect happens to a lesser extent at 3T with about 20% reduction (61). This phenomenon arises because the RF field at any given point in the tissue is the summation of multiple traveling waves produced by each portion of the coil. For shorter wavelengths, the summation may lead to destructive interference if the path length of each wave component varies. Thus when RF excitation is designed to deliver a specific flip angle distribution over space, these interference

effects must be considered. This effect gives rise to a spatial variation in the possible SNR gain at higher field strengths since interference effects will decrease the flip angles significantly near the edge of the brain while maintaining the intended flip angle near the center. An example of the field focusing effect at 3T and 4.7 T is illustrated in Figure 1-19, showing a theoretical head model (64,67). These results are similar to the 4.7 T experimental measurements found in (68), though somewhat more symmetric. The variation in flip angle delivered to different locations in the brain leads to variation in T_1 weighting. Different flip angles can easily lead to different contrast levels within the same image although in some cases the observer might be eluded by the intensity profile which might look more homogenous than the underlying flip angles distribution (69).

In another application, circle of Willis 3D TOF MRA normally makes use of a ramp pulse with distinct variation over space (6,7). The large RF variation explained above, which results from destructive interference of the short wavelengths, can undermine the effects of this ramp pulse. In chapter 4, a new method is introduced to overcome the RF inhomogeneity problems for intracranial 3D-TOF imaging, specifically for the middle cerebral artery tree with the application of 3.0 T.

1.5.4 Susceptibility Effects

Higher fields cause increased sensitivity to magnetic field inhomogeneity (70), which is both a beneficial and damaging effect. For example, the increased BOLD effect has been a great promise of high magnetic field (71,72), however the decreased EPI image quality, arising from the increased sensitivity to field

distortion, has severely limited the whole brain applications of single shot EPI at high field.

As the field is increased, the slight susceptibility difference between tissues increases accordingly. This leads to greater sensitivity to variation in magnetic susceptibility can be advantageous for distinguishing areas of tissue with increased deoxyhemoglobin or increased iron content (31). At the same time, signal loss at air-tissue interfaces will increase. Gradient echo sequences particularly with long echo times, will potentially suffer from these effects.

In summary, higher field provides tremendous potential for imaging; however, the pulse sequence approaches must overcome the challenges of RF limitations on power and homogeneity. In addition, the approaches must cope with the increased sensitivity to magnetic field inhomogeneity and varying relaxation rates.
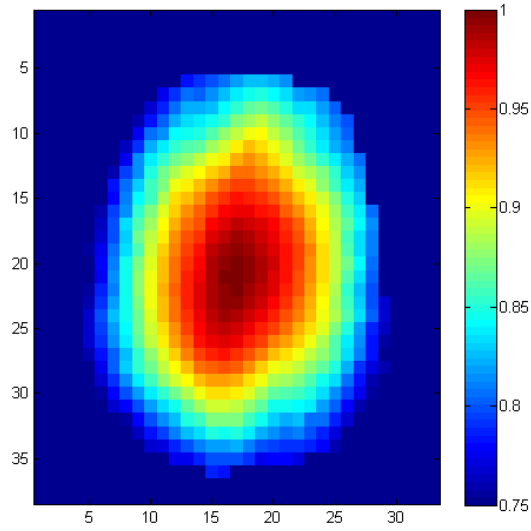
(a)
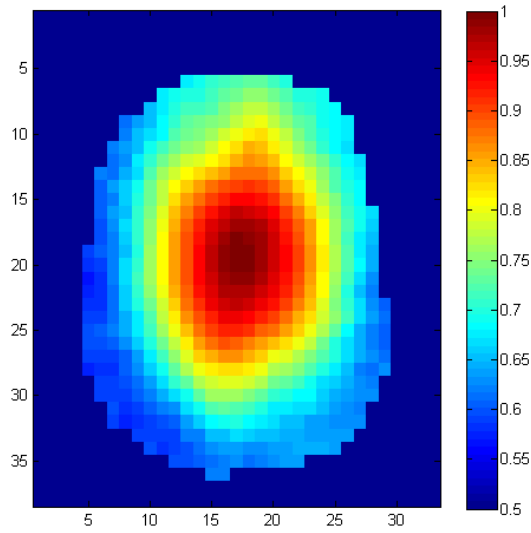
(b)

Figure 1-19: Axial slices showing theoretical RF field distribution at **(a)** 3.0 T and **(b)** 4.7T. At 4.7 T, RF intensity reached as 57% of the maximum within the shown slice as opposed to 73% in the 3.0 T case.

1.6 References

1- Suryan G. Nuclear resonance in flowing liquids. Proc Indian Acad Sci, 1951; 33:107-111.

2- Singer JR. Blood flow rates by nuclear magnetic resonance measurements. Science, 1959; 130:1652-1653.

3- Morse OC and Singer JR. Blood velocity measurement in intact subject. Science, 1970; 170:440-441.

4- Keller PJ, et al. MR angiography with two-dimensional acquisition and three-dimensional display. Radiology, 1989; 173:527-532.

5- Dumoulin, CL, et al. Three-dimensional time-of-flight magnetic resonance angiography using spin saturation. Magn Reson Med, 1989; 11:35-46.

6- Atkinson D, BrantZawadzki M, Gillan G, Purdy D, Laub G. Improved MR-Angiography – magnetization-transfer suppression with variable flip angle excitation and increased resolution. Radiology, 1994; 190:890-894.

7- Nagele T, Klose U, Grodd W, Petersen D, Tintera J. The effects of linearly increasing flip angles on 3D inflow MR-Angiography. Magn Reson Med 1994;31:561-566.

8- Pelc NJ, Herfkens RJ, Shimakawa A, Enzmann DR. Phase contrast cine magnetic resonance imaging. Magn Reson Q. 1991; 7(4):229-254.

9- Moran PR. Experiments for two MR imaging theories of motion phase sensitivity. Radiology, 1991; 180:115-119.

10- Hausmann R, Lewin JS and Laub G. Phase contrast MR angiography with reduced acquisition time: new concepts in sequence design. J Magn Reson Imag, 1991; 1: 415.

11- NJ Pele, MA Bernstein, A Shimakawa and GH Glover. Encoding strategies for three-direction phase contrast MR imaging of flow. J Magn Reson Imag, 1991; 1: 405.

12- McRobbie DW, Moore EA, Graves MJ and Prince MR, MRI from Picture to Proton, 2nd Ed 2006, Cambridge University Press.

13- Bernstein MA, King KF, Zhou XJ. Handbook of MRI Pulse Sequences. 2004 Academic Press.

14- Bloch, F., Nuclear Induction. Physical Review, 1947; 70(7,8):460-474.

15- Brown, MA and Semelka, RC, MRI Basic Principles and Applications, 3rd Ed 2003, John Wiley and Sons, Inc.

16- Hayes E C, Wdelstein W A, Schenck D F, Mueller O M and Eash M. An efficient highly homogeneous radiofrequency coil for whole-body NMR imaging at 1.5 T. J Magn Reson, 1985; 63:622–8.

17- Sank VJ, Chen C-N and Hoult A. A Quadrature Coil for the Adult Human Head. J Magn Reson, 1986; 69:236-242,

18- Kuperman. Magnetic Resonance Imaging - Physical Principles and Applications, 2000.

19- Filippi M, De Stefano N, Dousset V, McGowan JC. MRI in White Matter Diseases of the Brain and Spinal Cord. Med Radiol Diagnostic Imaging Series (Editors: A. L. Baert and K. Sartor, Springer-Verlag Berlin Heidelberg 2005).

20- Weishaupt D, Köchli VD, Marincek B. How Does MRI Work, An Introduction to the Physics and Function of Magnetic Resonance Imaging, 2nd Ed, Springer-Verlag 2006.

21- Sijbers J, den Dekker AJ, Van Audekerke J, Verhoye M and Van Dyck D. Estimation of the Noise in Magnitude MR Images. Magn Reson Imag, 1998; 16(1): 87-90.

22- Haacke EM, Brown RW, Thompson MR, Venkatesan R. Magnetic resonance imaging physical principles and sequence design. New York:John Wiley & Sons; 1999.

23- Lauzon ML, Rutt BK. Generalized k-Space Analysis and Correction of Motion Effects in MR Imaging. Magn Reson Med, 1993; 30(4): 438-446.

24- Axel L and Morton D. MR flow imaging of velocity compensated / uncompensated difference images. J Comput Assist Tomog, 1987; 11:31.

25- Haacke EM and Lenz GW. Improving MR image quality in the presence of motion by using rephasing gradients. Am J Roentgenology, 1987; 148:1251.

26- Nayler GL, Firmin DN and Longmore DB. Blood flow imaging by cine magnetic resonance. J Comput Assist Tomogr, 1986; 10:715.

27- Nishimura DG, Macovski A and Pauly JM. Magnetic Resonance Angiography. IEEE Trans. Med. Imag., 1986; MI-5:140.

28- Laub GA, Kaiser WA. MR Angiography with gradient motion refocusing. J Comput Assist Tomog, 1988; 12(3):377-382.

29- Iacconi C, Cilotti A, Marini C, Moretti M, Mazzotta D, Odoguardi F, Cardillo FA and Starita A, Maximum Intensity Projection in Contrast-Enhanced

magnetic Resonance of the Breast, University of Pisa, Italy, internet access on March 1, 2010.

30- Deshpande V and Laub G, US Patent 7636463, Multi-Planar Reformating Using a 3-Point Tool, assigned to Siemens Aktiengesellschaft, Munich, Germany, December 22, 2009.

31- Haacke EM, Xu Y, Cheng YC, Reichenbach JR. Susceptibility weighted imaging (SWI). Magn Reson Med 2004;52:612–618.

32- Wang Y, Yu Y, Li D, Bae KT, Brown JJ, Lin W, Haacke EM. Artery and vein separation using susceptibility-dependent phase in contrast-enhanced MRA. JMRI 2000; 12:661–670.

33- Reichenbach JR, Essig M, Haacke EM, et al. High-resolution venography of the brain using magnetic resonance imaging. MAGMA, 1998; 6:62–69.

34- Ogg RJ, Langston JW, Haacke EM, Steen RG, Taylor JS. The correlation between phase shifts in gradient-echo MR images and regional brain iron concentration. Magn Reson Imaging 1999; 17: 1141–1148.

35- Abduljalil AM, Schmalbrock P, Novak V, Chakeres DW. Enhanced gray and white matter contrast of phase susceptibility-weighted images in ultra-high-field magnetic resonance imaging. J Magn Reson Imaging 2003; 18:284–290.

36- Rauscher A, Sedlacik J, Barth M, Mentzel HJ, Reichenbach JR. Magnetic susceptibility sensitive MR phase imaging in the human brain. AJNR Am J Neuroradiol 2005;177:736–742.

37- Duyn JH, van Gelderen P, Li TQ, de Zwart JA, Koretsky AP, Fukunaga M. High-field MRI of brain cortical substructure based on signal phase. PNAS 2007;104(28):11796-11801.

38- Yao B, Li TQ, Gelderen PV, Shmueli K, de Zwart JA and Duyn JH. Susceptibility contrast in high field MRI of human brain as a function of tissue iron content, NeuroImage 44 (2009), pp. 1259–1266.

39- Xu Y, Haacke EM. The role of voxel aspect ratio in determining apparent vascular phase behavior in susceptibility weighted imaging. Magn Reson Imag. 2006; 24:155-160.

40- Wehrli FW. TIME-OF-FLIGHT EFFECTS IN MR IMAGING OF FLOW. Magn. Reson. Med. 14(2); 187-193, 1990.

41- Gao JH, Holland SK and Gore JC. Nuclear magnetic resonance signal from flowing nuclei in rapid imaging using gradient echoes. Med Phys 1988; 15:809.

42- Haacke EM, Masaryk TJ, Weilopolski PA, et al. Optimizing blood vessel contrast in fast three-dimensional MRI. Magn Reson Med 1990; 14:202.

43- Bernstein MA, Shimakawa A, Pelc NJ. Minimizing TE in Moment-nulled or Flow-encoded Two- and Three-dimensional Gradient-Echo Imaging. JMRI 1992; 2:583-588.

44- Bernstein MA. Analytical solution for tri-directional flow compensation. In: Proceedings of the 4th Annual Meeting of ISMRM, New York, 1996. p 1254.

45- Potchen EJ, Haacke EM, Siebert JE, Gottschalk A. Magnetic Resonance Angiography; Concepts and Applications. 1993, St. Louis: Mosby.

46- Alayar Kangarlua, Lin Tangd,e, Tamer S. Ibrahim Electric Field Measurements and Computational Modeling at Ultrahigh-Field MRI, Magnetic Resonance Imaging 2007; 25:1222–1226.

47- Ibrahim, Tamer S. Design of RF Coils for MRI Applications, A Computational Electromagnetic Approach. Ph. D. Dissertation, Ohio State University, 2003.

48- Adams JJ. Numerical Design of Resonator Coils for High Field Magnetic Resonance Imaging. MSc Thesis, Ohio State University, 2005.

49- Wald LL, Wiggins GC, Potthast A, Wiggins CJ, and Triantafyllou1 C. Design Considerations and Coil Comparisons for 7 T Brain Imaging. Appl. Magn Reson 2005; 29:19-37.

50- Jezzard P, Duewell S, Balaban RS. MR relaxation times in human brain: measurement at 4 T. Radiology 1996; 199: 773-779.

51- Ibrahim TS, Abduljalil1 AM, Baertlein BA, Lee R and Robitaille P-M-L. Analysis of B1 field profiles and SAR values for multi-strut transverse electromagnetic RF coils in high field MRI applications. Phys Med Biol 2001; 46:2545–2555.

52- Carmichael DW, Thomas DL, De Vita E, Fernández-Seara MA, Chhina N, Cooper M, Sunderland C, Randell C, Turner R, Ordidge RJ. Improving whole brain structural MRI at 4.7 Tesla using 4 irregularly shaped receiver coils. Neuroimage. 2006; 32:1176-84.

53- Hayes CE, Hattes N, Roemer PB.Volume imaging with MR phased arrays. Magn Reson Med 1991; 18(2):309-19.

54- Kiaran P. McGee, Eric E. Williamson and Paul R. Julsrud, MRI Mayo Clinic Guide to Cardiac magnetic resonance imaging, (Mayo Foundation for Medical Education and Research, 1st Ed, 2008).

55- Hudson AM, Kockenberger W, Bowtell RW. Open access birdcage coils for microscopic imaging of plants at 11.7 T. Magn Reson Materials; Phys Biol Med 2000; 10:69-74.

56- Hennig, J. Current Issues in High-Field Magnetic Resonance. Appl Magn Reson 2005; 29(1):1-3.

57- Van de Moortele, PF; Auerbach, EJ; Olman, C, et al. T-1 weighted brain images at 7 Tesla unbiased for Proton Density, T-2* contrast and RF coil receive B-1 sensitivity with simultaneous vessel visualization. NeuroImage 2009; 46(2) :432–446.

58- Bottomley PA, Andrews ER. RF magnetic-field penetration, phase shift and power dissipation in biological tissue - Implications for NMR imaging. Phys Med Biol 1978:23:630–643.

59- Hennig, J., Nauerth, A., Friedburg, H. RARE imaging: a fast imaging method for clinical MR. Magn Reson Med, 1986; 3:823-33.

60- Roschmann P. Radiofrequency penetration and absorption in the human body: limitations to high-field whole-body nuclear magnetic resonance imaging. Med Phys 1987:14:922–931.

61- Alecci M, Collins CM, Smith MB, Jezzard P. Radio Frequency Magnetic Field Mapping of a 3 Tesla Birdcage Coil: Experimental and Theoretical Dependence on Sample Properties. Magn Reson Med 2001:46:379–385.

62- Van de Moortele PF, Akgun C, Adriany G, et al. B-1 destructive interferences and spatial phase patterns at 7 T with a head transceiver array coil. Mag Res Med 2005:54: 1503-1518.

63- Jin JM, Chen J, Chew WC, Gan H, Magin RL, Dimbylow PJ. Computation of electromagnetic fields for high-frequency magnetic resonance imaging applications. Phys Med Biol 1996:41:2719–2738.

64- Collins CM, Li SZ, Smith MB. SAR and B-1 field distributions in a heterogeneous human head model within a birdcage coil. Magn Reson Med 1998; 40:847–856.

65- Simunic D, Wach P, Renhart W, Stollberger R. Spatial distribution of high-frequency electromagnetic energy in human head during MRI: Numerical results and measurements. IEEE Trans Biomed Eng 1996; 43: 88-94.

66- Vaughan JT, Garwood M, Collins CM, Liu W, DelaBarre L, Adriany G, Andersen P, Merkle H, Goebel R, Smith MB, Ugurbil K.7T vs. 4T: RF Power, Homogeneity, and Signal-to-Noise Comparison in Head Images. Magn Reson Med 2001; 46:24–30.

67- Collins CM, Smith MB. Signal-to-noise ratio and absorbed power as functions of main magnetic field strength, and definition of "90 degrees" RF pulse for the head in the birdcage coil. Magn Reson Med 2001; 45:684–691.

68- Thomas DL, De Vita E, Roberts S, Turner R, Yousry TA, Ordidge RJ. High-resolution fast spin echo imaging of the human brain at 4.7 T: implementation and sequence characteristics. Magn Reson Med. 2004; 51:1254-64.

69- Wang D, Heberlein K, LaConte S, Hu X. Inherent insensitivity to RF inhomogeneity in FLASH imaging. Magn Reson Med. 2004; 52:927-31.

70- Gati JS, Menon RS, Urgurbil K, Rut BK. Experimental Determination of the BOLD field strength dependence in vessels and tissue. Magn Reson Med. 1997; 38:296-302.

71- Ogawa S, Tank DW, Menon R, et al. Intrinsic signal changes accompanying sensory stimulation: functional brain mapping with magnetic resonance imaging. Proc Natl Acad Sci USA 1992; 89: 5951-5955.

72- Ugurbil K, Adriany G, Andersen P, Chen W, Garwood M, Gruetter R, Henry PG, Kim SG, Lieu H, Tkac I, Vaughan T, Van De Moortele PF, Yacoub E, Zhu XH. Ultrahigh field magnetic resonance imaging and spectroscopy. Magn Reson Imaging. 2003; 21:1263-81.

Chapter 2

Detecting Lesions in Multiple Sclerosis at 4.7 Tesla Using

Phase Susceptibility-Weighting and T2Weighting

2.1 Introduction

MRI systems have already demonstrated intrinsic susceptibility contrast in human brain utilizing the image phase from a T_2*-weighted gradient echo at both low and high magnetic fields (1-6). Susceptibility-based phase differences increase linearly with magnetic field allowing for a reduction in echo time as the field is increased, which provides a significant SNR benefit in addition to the increased magnetization intrinsic to higher fields. Thus, increasingly higher fields will be preferred for phase susceptibility imaging, provided adequate volume coverage remains possible which may be limited by RF uniformity (7), or air-tissue susceptibility losses. For multiple sclerosis (MS), evidence is now accumulating that susceptibility-weighting may provide a valuable contrast mechanism for identifying lesions that have a significant iron content (8-10); however, the clinical significance of these lesions is unknown. The presence of iron in some MS lesions may be due to hemosiderin products, ferritin buildup, or to the presence of high levels of deoxyhemoglobin (11-13). The phase image is far more sensitive than a magnitude image for detecting subtle changes arising from iron since bulk intravoxel phase shifts can occur without significant phase

dispersion and magnitude loss. This phase measure is also more specific than magnitude hypointensity since relaxation effects are eliminated, and calcifications can be eliminated due to its opposing phase shift (12). Phase susceptibility-weighting provides a valuable new contrast mechanism for assessment of lesions in MS; however, evaluation of this new phase contrast requires comparison to standard MRI approaches.

Table 2-1: MRI Acquisition Parameters

Imaging Parameter	2D T2WFSE Moderate resolution	2D T2WFSE High Resolution	3D SWI
Voxel Size (before zerofilling)	1.84 mm^3	0.34 mm^3	0.90 mm^3
Slice thickness	3.5 mm, no gap	2.5 mm, no gap	3 mm, no gap
Number of slices	36	36	22 slices per slab
In–plane matrix	294 x 256	768 x 378	512 x 256
Field-of-View	22 cm x 18 cm	22 cm x 18 cm	22 cm x 18 cm
TE/TR	51ms/5000ms	44ms/5000ms	20ms/70ms
Flip angles	90º-150º-120º…	90º-165º-150º…	20º
Echo Spacing	17 ms	22 ms	Not applicable
Echo Train	8 echoes	7 echoes	1 echo
Acquisition Time	5.3 min	9 min	6.6 min per slab

T2-weighted fast spin echo (T2WFSE) imaging is a critical component of standard MS lesion evaluation with MRI (eg. 14,15). Previous studies at 7.0 and 8.0 T on human brain using phase susceptibility, either did not compare to T2WFSE, or performed FSE at a lower field strength of 3.0 T (2, 5, 6, 8, 16). Utilizing the same field strength for T2WFSE and susceptibility-weighted imaging (SWI) is essential to understand the added value of phase imaging in MS, since higher fields are known to provide significantly higher lesion counts in T2WFSE (17-19). Recent MS work by Haacke (9) utilized the same field strength for each patient, either 3.0 or 4.0 T, for T2WFSE and SWI; however they

employed substantially lower spatial resolution T2WFSE than SWI, with FSE voxel volumes 8.1 times larger than SWI at 3.0 T, and FSE slice thickness double that of SWI at 4.0 T. Although Haacke (9) has clearly illustrated the visibility and categorization of MS lesions in phase susceptibility imaging, it remains unclear as to the added benefit of phase susceptibility imaging over T2WFSE for high field lesion identification, since some of the benefits of SWI over T2WFSE may have arisen purely from using substantially higher spatial resolution for SWI. Certainly, it is well recognized that higher spatial resolution, in particular thinner slices, will result in higher lesion counts (20). Recently several groups (21-24) have demonstrated high definition T2WFSE of the human brain at 4.7 T. This 4.7 T field strength is also well positioned for excellent susceptibility weighting. Here our goal is to apply phase SWI, as well as T2WFSE, for the study of lesion conspicuity in multiple sclerosis patients at 4.7 T, using similar slice thickness for all methods. This is the first application of 4.7 T imaging in any patient group using FSE and SWI.

2.2 Methods

Human brain imaging of seven relapsing-remitting multiple sclerosis patients (mean age 50.1 ± 5.6 yrs, 5 female, 2 male) was performed using both high and moderate resolution T2WFSE, as well as 3D phase susceptibility-weighted imaging. This study was approved by the local ethics committee, and all subjects gave written informed consent. Images were acquired in the axial orientation. All scans were performed on a 4.7 T whole body MRI system (Varian, Palo Alto, USA). A circumscribing 27-cm transmission RF coil was

used, with reception from either the same coil or a closely-coupled 4-element array coil (PulseTeq, United Kingdom).

Typical acquisition parameters for the three imaging sequences are detailed in Table 2-1. The T2WFSE method was performed at very high resolution with 0.34 mm^3 voxel volumes, then at moderate resolution with 1.84 mm^3 voxels. Following 90º excitation, the FSE methods used refocusing flip angle trains of (150º,120º,120º,120º,120º,120º,120º,120º) for moderate resolution; and (165º,150º,150º,150º,150º,150º,150º) for high resolution. Both FSE acquisitions used two interleaved 18-slice concatenations to yield the 36 contiguous slices. The SWI method employed voxel volumes of 0.90 mm^3. The resulting T2*-weighted gradient echo images were reconstructed to create T2* magnitude, and raw phase images. The phase susceptibility image, named phase SWI, was created by dividing the original complex image by a low pass filtered image created by using a 2D spatial frequency kernel that extended over 1/8th of the k-space matrix, then measuring the resultant phase angle (3). An additional magnitude SWI image was created by multiplying the T2* magnitude by a masked version of the phase SWI image to the 4th power (3).

Quantitative and qualitative measurements were performed on the resulting images. An experienced neuroradiologist evaluated the images from each MRI technique separately to determine the total number of visible lesions. Total lesion counts with T2WFSE and phase SWI were determined independently, without visualization of the other imaging sequence. Lesions on SWI magnitude images were not evaluated. In T2WFSE, lesions were defined as

regions of hyperintensity; in SWI, lesions were defined by hypointensity on the phase SWI image. Artifacts from veins on SWI, and perivascular spaces on FSE, were not considered to be lesions. It is well recognized that higher resolution FSE may result in more lesion counts, thus to fairly compare to the SWI exam with 3 mm slices, FSE lesions were counted on the moderate resolution FSE exam with 3.5 mm slices, with the higher resolution FSE serving only to verify FSE lesion location, and to define its boundaries more effectively. In addition quantitative measurements were made. On the phase SWI images, the absolute phase value and the local phase difference between hypointense lesion and immediate background was determined for each visible lesion. On the high and moderate resolution T2WFSE images, lesion-to-background contrast to noise ratio (CNR) was measured where noise was defined as the standard deviation of a region of air in the image. Normalized contrast defined as (lesion-background)/background was also measured.

2.3 Results

T2-weighted FSE revealed hyperintense lesions in all patients, while hypointense phase lesions were seen in 5 out of 7 patients with phase SWI. Table 2-2 illustrates the lesion counts in each patient for each method. Although the majority of lesions were seen with T2WFSE, 22 out of 124 total lesions were visible only with phase SWI and not with T2WFSE. The mean lesion-to-background normalized contrast and CNR on all MS lesions visible in both FSE methods was 0.59 ± 0.20 normalized contrast and 47.4 ± 22.1 CNR for moderate resolution, and 0.93 ± 0.33 and 16.2 ± 9.8, for high resolution FSE. Note that on

average, high resolution provided higher normalized contrast, but reduced CNR, owing to higher noise levels arising mainly from the five-fold smaller voxel volumes.

Table 2-2: Lesion Counts in Each Patient

Patient no.	Visible in FSE only	Visible in Phase SWI only	Visible with Both Methods	Total Visible Lesions
#1 (Fig. 2-1)	21	0	0	21
#2 (Fig. 2-2)	17	7	7	31
#3 (Fig. 2-3)	14	5	2	21
#4	19	0	0	19
#5	11	5	4	20
#6	1	0	1	2
#7	3	5	2	10
Total Counts	86	22	16	124

Example images from MS patients are shown in Figs.2-1 to 2-3. Figure 2-1 illustrates several T2-visible lesions not visible on phase SWI. This was the typical finding in this study. The differences between moderate and high resolution FSE are shown in Fig. 2-1(d,e), where small T2-visible lesions are better delineated in (e). Figure 2-2 shows two lesions detected with T2WFSE and phase SWI, one lesion detected exclusively with phase, and two lesions detected only with T2WFSE. Figure 2-3 illustrates many lesions including a lesion with central hyperintensity detected with T2WFSE surrounded by a hypointense ring detected with phase SWI.
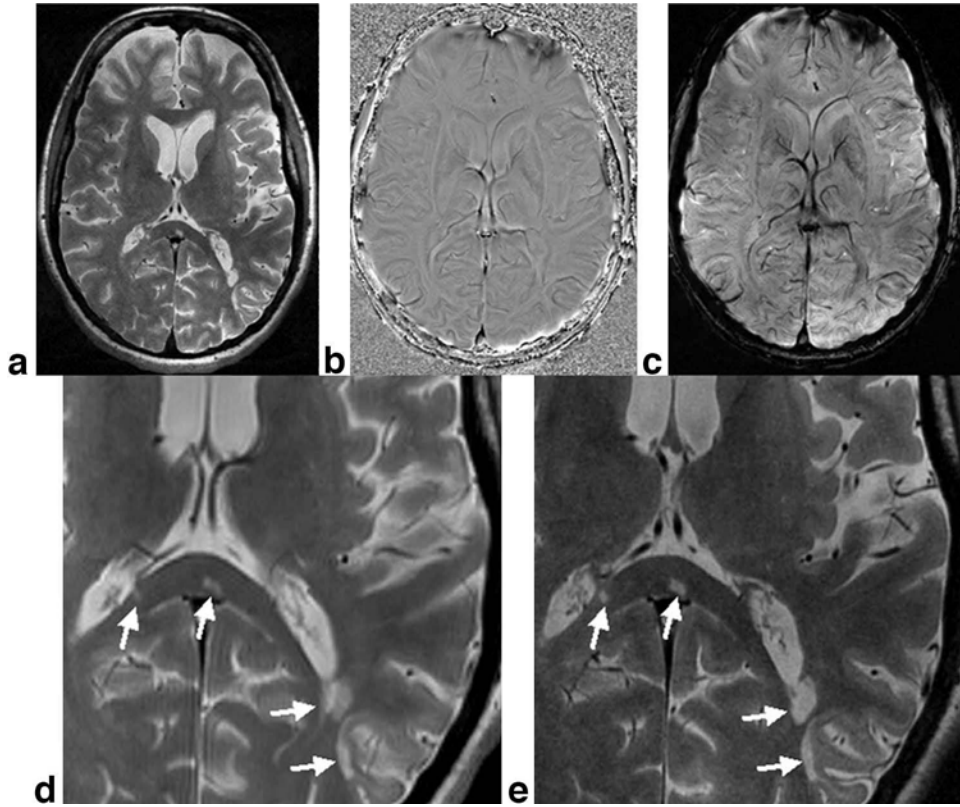
Figure 2-1. The 4.7 T images from MS patient #1, a 43-yearold female: (**a**) high resolution T2WFSE, (**b**) phase SWI, (**c**) magnitude-masked SWI, (**d,e**) magnified sections of (d) moderate and (e) high resolution T2WFSE. In this patient, no lesions were detected in phase or magnitude SWI. Several lesions are shown on T2WFSE (arrows). Small lesions are better depicted with (e) high resolution T2WFSE, but are also visible with (d) moderate resolution T2WFSE.
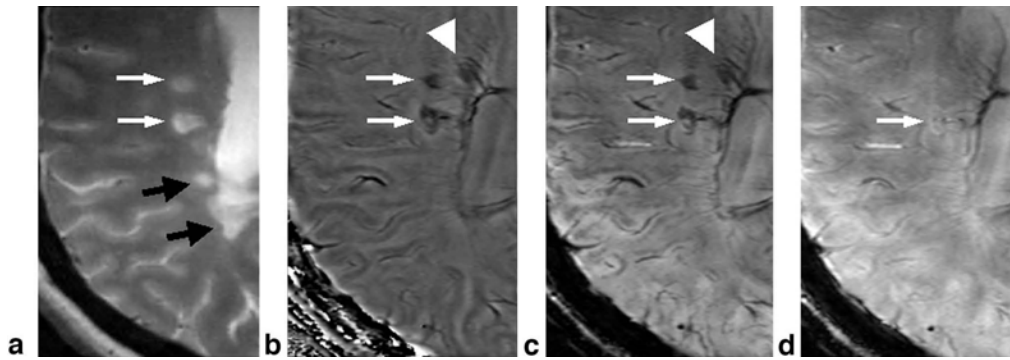
Figure 2-2: 4.7 T images from a 46 yr old female MS patient **(a)** moderate resolution T2WFSE, **(b)** phase SWI, **(c)** magnitude-masked SWI, (d) Magnitude (T2* weighted). Visible lesions include two detected with all methods (arrows), one lesion not detected by T2WFSE (arrowhead in b and c), and two additional lesions detected only on T2WFSE (black arrows in a).

Including all phase-visible lesions, the mean lesion phase difference relative to local background signal was -0.28 ± 0.15 radians (-16.3º ± 8.5º), with a range from –0.10 to –0.61 radians. The negative values support the presence of iron, which is paramagnetic and will align with the magnetic field leading to a negative phase shift relative to normal tissue for a standard right-handed system (3,9). This phase shift is linearly dependent on the local susceptibility difference, the echo time and the magnetic field. Given our TE of 20 ms and 4.7 T, the mean frequency shift in parts per billion (ppb) was -11.15 ± 5.97 ppb with a range of -3.9 to –24.3 ppb. The mean frequency shift in lesions was similar to the mean putamen shift of –11.07 ± 4.78 ppb relative to the same background. In other words, the lesion hypointensity on the phase image was typically isointense with putamen in these MS patients. Although the phase shift can be quantified and compared between sites, the phase variation is also dependent upon voxel dimensions and orientation with the main magnetic field (25,26). For these reasons, we only use the qualitative phase hypointensity when defining lesions.

86
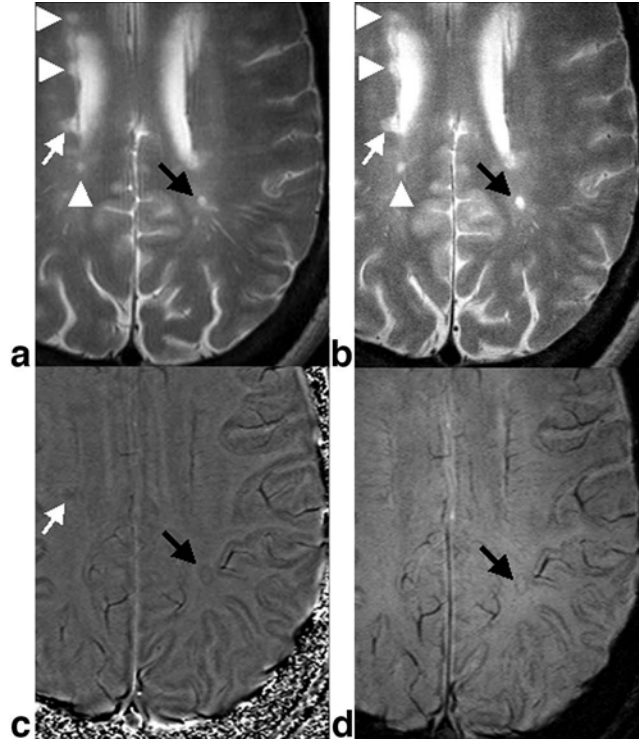
Figure 2-3: The 4.7 T images from MS patient #3, a 59-year-old female, illustrating a lesion (black arrows) with hyperintensity detected on **(a)** moderate and **(b)** high resolution T2WFSE, surrounded by a hypointense ring detected on **(c)** phase and **(d)** magnitude-masked SWI. Also visible is a lesion detected on phase SWI and T2WFSE (white arrow), as well as lesions detected only on T2WFSE (white arrowheads). In this case, the circumscribing head coil was used for receiving the signal (not the 4-element array), leading to lower SNR.

2.4 Discussion

We found 18% of the total lesions (22 out of 124) were seen only on phase SWI, and were invisible in moderate and high resolution T2WFSE images. Previous work in MS has also compared SWI to T2-weighted FSE. At 3.0 T, Haacke (9) found 18% (20 out of 111) of total lesions were seen only on SWI magnitude or phase and not T2WFSE, while at 4.0 T in a different population 47% (45 out of 96) of lesions were seen on SWI and not on T2WFSE. Hypointense phase lesions likely have a significant iron content, which provides

an additional imaging tool to reveal lesions with high iron loads. However, the differential diagnosis for hypointense phase lesions includes MS lesions, as well as other lesions such as microbleeds and cavernous hemangiomas. In addition, veins can also produce hypointensities. Since MS lesions tend to contain a central vein (10,11,16), the distinction between venous structures and an MS lesion can be difficult. More detailed discussion of the phase SWI characteristics of MS lesions is available elsewhere (8, 9).

Considering only the 102 lesions visible with T2WFSE, 16 of these (i.e.: 16%) were also seen in phase SWI. In our case, the T2WFSE and phase SWI methods were complementary, each demonstrating a specific contrast mechanism, but typically both methods did not coincide. Haacke found a far greater percentage of concordance between T2-visible lesions and phase SWI hypointensity: 65% of T2-visible lesions were seen with phase SWI at 4.0 T, and in a different patient population, 42% at 3.0T (9). Three possible reasons for these differences between studies are: patient heterogeneity, spatial resolution differences, and lesion identification differences. First, differences may simply arise from MS patient heterogeneity since both studies used small patient numbers. The variation between MS patients is clearly evident in Table 2-2. In particular, we note that two MS patients had many lesions visible on T2WFSE, without any visible on phase SWI. Second, spatial resolution differences, particularly slice thickness differences, between FSE and SWI may account for variable lesion counts. At 4.0 T, Haacke used twice the slice thickness for FSE versus SWI, which may have led to reduced lesion counts in FSE. At 3.0 T, the

8 times larger FSE voxel volume and 50% larger FSE slice thickness may have also favored SWI. In our study, moderate resolution FSE used 3.5 mm slices, high resolution FSE 2.5 mm and SWI used a similar slice thickness of 3.0 mm. While in-plane resolution differences were substantial in our work (0.3 mm^2 SWI, 0.53 mm^2 moderate FSE, and 0.14 mm^2 high resolution FSE), we did not use the high resolution FSE for lesion identification. Third, differences in SWI lesion identification methods are likely. Phase SWI is a new technique, our neuroradiologist excluded veins on phase SWI that also produce hypointensities similar to MS lesions, which may have led to a more conservative count of SWI visible lesions. In addition, we considered each imaging method independently, thus phase SWI did not have the benefit of knowledge of the location of the T2WFSE hyperintensity. A larger study of MS patients is warranted to assess the relationship between T2 visibility and iron-sensitive susceptibility methods in more detail using matched resolution and field strength.

For lesion quantification, we focused on the phase SWI image only and did not use the raw magnitude image, nor the SWI image. The phase image is immune to differences in relaxation weighting, which enables easy comparison across sites. For SWI at 4.7 T, we used a TE of 20 ms, which corresponds to a TE of 31.3 ms at 3.0 T to achieve the same susceptibility phase evolution. When performing 3D SWI with 20º flip angle and TR of 70 ms as used here, the T2* magnitude has some T1 weighting, which darkens fluid and edema leading to poorer observation of hyperintense lesions on the raw magnitude images. Use of a longer TR, or a 2D interleaved method, minimizes the T1 weighting, however

hyperintensity in the T2*-weighted magnitude combined with hypointensity in the phase can partially cancel lesion visibility in the SWI image. This effect was observed in one lesion in Fig. 2-2, even with substantial T1 weighting in the T2*-weighted magnitude. By focusing only on the phase images for quantification, we remove the T2* and T1 relaxation confounds arising in the magnitude and SWI image, and obtain pure susceptibility weighting. In addition, the phase image benefits from relative immunity to transmit and receive RF variation, which is common at high magnetic fields. While our goal here was to evaluate only the phase SWI image versus T2WFSE, both the raw magnitude and magnitude SWI provide additional contrast mechanisms for MS lesion visualization (8,9).

For T2WFSE at 4.7 T, the high resolution technique used 0.34 mm^3 voxels, which is ten-fold smaller than standard low field clinical FSE where ~ 4 mm^3 voxel volumes are more common (eg: 5 mm slice, 230 mm field-of-view, 256 x 256 in plane matrix). This extremely high resolution FSE depicted the MS lesions precisely and would be ideal for observing time course changes in MS lesion volumes. The higher resolution FSE provided sharp lesion delineation and less partial volume effects for small lesions. Including all visible lesions in both FSE methods, high resolution had 92% more normalized contrast than moderate resolution. Nevertheless, owing to only 1 mm difference in slice thickness (2.5 vs. 3.5 mm), moderate resolution T2WFSE still provided similar lesion counts, although with substantially reduced lesion sharpness. When considering noise as well, moderate resolution had on average 2.9 times higher CNR mainly due to the five-fold increase in voxel volume. In particular, for large lesions

without partial volume effects, moderate resolution produced substantially more CNR, although with reduced edge definition.

The FSE sequence is RF intensive. RF heating scales with the square of the magnetic field and the square of the RF pulse amplitude. To control RF heating at 4.7 T, the RF refocusing pulses were lengthened in time and reduced in flip angle by using a variable refocusing train (21,27). For this implementation, we used 6 ms pulse duration refocusing pulses (480 Hz pulse bandwidth) with variable flip angle trains of 7 or 8 echoes as listed. Owing to this RF pulse length and the need for extremely high spatial resolution, interecho spacings were 22 ms for high resolution FSE (readout: 67 kHz, 768 points) and 17 ms for moderate resolution FSE (readout: 49 kHz, 294 points). With these parameters we were able to obtain high quality T2W FSE images with significant brain coverage in reasonable imaging times. At 7.0 T, MS studies using phase SWI have yet to perform a detailed comparison to T2WFSE at the same field strength (6,8,16). The lack of T2WFSE correlation at 7.0 T arises from the challenges in performing multi-slice, time-efficient T2WFSE at higher magnetic fields due to increased RF heating, as well as increased RF interference (7). For example, a recent MS study at 7.0 T using T2WFSE typically obtained only 6 slices in 4.4 minutes owing to the RF heating limitation (19).

The 4.7 T field strength can provide both very high resolution T2WFSE and excellent susceptibility weighting as demonstrated. Currently, 4.7 T is a rare field strength for human imaging, with 3.0 and 7.0 T strengths being far more common. The 4.7 T strength theoretically provides 67% of the SNR of 7.0 T with

the advantage of only 45% of the RF heating, making 4.7 T well-suited for patient protocols requiring time-efficient, RF-intensive FSE. For susceptibility-weighting, 4.7 T provides benefits over 3.0 T by enabling SWI echo reduction by 63%, as well as theoretically providing 1.6 times greater intrinsic magnetization. For neurological MRI protocols demanding both susceptibility-weighting and time-efficient FSE, 4.7 T is well positioned on the field continuum.

Limitations of this work include the lack of whole head coverage. The imaging volume was limited to only ~9 cm superior-inferior coverage with transverse slices (eg: 36 slices at 2.5mm thickness for high resolution FSE) due both to thin slices and acquisition time limitations for high in-plane phase encode resolution. Whole head coverage would have been possible with much longer acquisition times for FSE, however we wished to limit each high resolution pulse sequence to under 9 minutes for patient comfort and compliance. For SWI, whole head coverage could have been possible by using a much shorter TR and reduced flip angle to allow for increased slices, or by using an interleaved 2D approach. In our case, we used a 70 ms TR for 3D SWI, which lead to significant dead time between acquisitions. We chose this approach to allow partial T1 recovery for a moderate flip angle of 20°.A second limitation was the use of only one neuroradiologist in the evaluation process. We used the only experienced MS neuroradiologist in our clinic familiar with the new SWI method. Finally more comprehensive studies with more patients are warranted; however this study, with 124 identified lesions, provides support of the potential radiological value of phase susceptibility imaging in combination with high resolution T2WFSE at the

same high field strength, and provides the first patient study of any kind to use 4.7 T for T2WFSE combined with phase SWI.

In conclusion, we have demonstrated the value of the combination of extremely high resolution T2WFSE and phase SWI for lesion detection in MS. In seven relapsing remitting MS patients at 4.7 T, we found that 18% of MS lesions were invisible on moderate and high resolution T2WFSE, but were observed on phase SWI. Phase SWI improves assessment of MS lesion load and emphasizes iron-containing lesions. Further MS studies are necessary to understand the signal time course of this new contrast mechanism in relation to both T2WFSE and gadolinium-enhancement.

2.5 References

1. Ogg, RJ, Langston, JW, Haacke, EM, Steen, RG, Taylor, JS. The correlation between phase shifts in gradient-echo MR images and regional brain iron concentration. Magn. Reson. Imaging 1999; 17:1141–1148.

2. Abduljalil, AM, Schmalbrock, P, Novak, V, Chakeres, DW. Enhanced gray and white matter contrast of phase susceptibility-weighted images in ultra-high-field magnetic resonance imaging. J. Magn. Reson. Imaging 2003; 18:284–290.

3. Haacke, EM, Xu, Y, Cheng, YC, Reichenbach, JR. Susceptibility weighted imaging (SWI). Magn. Reson. Med. 2004; 52:612–618.

4. Rauscher A, Sedlacik J, Barth M, Mentzel HJ, Reichenbach JR. Magnetic susceptibility sensitive MR phase imaging in the human brain. AJNR 2005 177:1065-9.

5. Duyn JH, van Gelderen P, Li TQ, de Zwart JA, Koretsky AP, Fukunaga M. High-field MRI of brain cortical substructure based on signal phase. PNAS 2007; 104:11796-801.

6. Hammond KE, Lupo JM, Xu D, et al. Development of a robust method for generating 7.0 T multichannel phase images of the brain with application to normal volunteers and patients with neurological diseases. Neuroimage. 2008; 39:1682-92.

7. Vaughan JT, Garwood M, Collins CM, et al. 7 T vs. 4T: RF power, homogeneity, and signal-to-noise comparison in head images. Magn Reson Med 2001; 46:24-30.

8. Hammond KE, Metcalf M, Carvajal L, et al. Quantitative in vivo magnetic resonance imaging of multiple sclerosis at 7 Tesla with sensitivity to iron. Ann Neurol 2008; 64:707–713.

9. Haacke EM, Makki M, Ge Y, et al. Characterizing iron deposition in multiple sclerosis lesions using susceptibility weighted imaging. J Magn Reson Imaging. 200; 29(3):537-44.

10. Ge Y, Zohrabian VM, Grossman RI. Seven-Tesla magnetic resonance imaging: new vision of microvascular abnormalities in multiple sclerosis. Arch Neurol. 2008;65:812-6.

11. Zamboni P. The Big Idea: Iron-dependent inflammation in venous disease and proposed parallels in multiple sclerosis. J R Soc Med 2006; 99:589-93.

12. Haacke EM, Cheng NY, House MJ,et al. Imaging iron stores in the brain using magnetic resonance imaging. Magn Reson Imaging. 2005;23:1-25.

13. Schenck JF and Zimmerman EA. High-field MRI of brain iron: birth of a biomarker? NMR in Biomed 2004; 17:433-45.

14. Miller DH, Grossman RI, Reingold SC, McFarland HF. The role of MR techniques in understanding and managing multiple sclerosis. Brain 1998; 121:3-24.

15. Rudick RA, Lee JC, Simon J, Fisher E. Significance of T2 lesions in multiple sclerosis: a 13-year longitudinal study. Ann Neurol 2006; 60:236–242.

16. Tallantyre EC, Brookes MJ, Dixon JE, Morgan PS, Evangelou N, Morris PG. Demonstrating the perivascular distribution of MS lesions in vivo with 7 Tesla MRI. Neurology. 2008; 70:2076-8.

17. Wattjes MP, Barkhof F. High field MRI in the diagnosis of multiple sclerosis: high field-high yield? Neuroradiology. 2009; 51:279-92.

18. Keiper MD, Grossman RI, Hirsch JA, et al. MR Identification of White Matter Abnormalities in Multiple Sclerosis:A Comparison between 1.5 T and 4 T. Am J Neuroradiol 1998; 19:1489–1493.

19. Kollia K, Maderwald S, Putzki N, et al. First clinical study on ultra-high-field MR imaging in patients with multiple sclerosis: comparison of 1.5T and 7 T. AJNR Am J Neuroradiol. 2009; 30:699-702.

20. Erskine M, Cook L, Riddle K, Mitchell JR, Karlik SJ, Resolution-Dependent Estimates of Multiple Sclerosis Lesion Loads, Can J Neurol Sci 2005; 32:205-212.

21. Lebel RM, Wilman AH. Time-efficient fast spin echo imaging at 4.7 T with low refocusing angles. Magn Reson Med 2009; 62:96-105.

22. De Vita E, Thomas DL, Roberts S,et al. High resolution MRI of the brain at 4.7 Tesla using fast spin echo imaging. Br J Radiol. 2003; 76:631-7.

23. Thomas DL, De Vita E, Roberts S, Turner R, Yousry TA, Ordidge RJ. High-resolution fast spin echo imaging of the human brain at 4.7 T: implementation and sequence characteristics. Magn Reson Med 2004; 51: 1254-1264.

24. Carmicheal DW, Thomas DL, De Vita E et al. Improving whole brain structural MRI at 4.7 Tesla using 4 irregularly shaped receiver coils. Neuroimage 2006;32:1176-84.

25. Xu Y, Haacke EM. The role of voxel aspect ratio in determining apparent vascular phase behavior in susceptibility weighted imaging. Magn Reson Imag 2006; 24:155–160.

26. Deistung A, Rauscher A, Sedlacik J, Stadler J, Witoszynskyj S, Reichenbach JR. Susceptibility weighted imaging at ultra high magnetic field strengths: theoretical considerations and experimental results. Magn Reson Med 2008; 60:1155-1168.

27. Hennig J, Scheffler K. Easy improvement of signal-to-noise in RARE-sequences with low refocusing flip angles. Rapid acquisition with relaxation enhancement. Magn Reson Med 2000; 44: 983-985.

Chapter 3

3D MRI with Independent Slab Excitation and Encoding

(ISEE): Application to Oblique SWI

Purpose: The purpose of this work is to introduce a new approach to 3D imaging that separates slab excitation and slab encoding directions. One version of this new method enables oblique imaging volumes with voxel encoding aligned with the main magnetic field, which enables accurate obliquely oriented susceptibility-weighted imaging.

3.1 Introduction

Three dimensional Fourier transform MRI typically uses the same orientation for slab excitation and slab phase encoding (1). Here, we introduce a new approach for oblique 3D imaging, whereby an arbitrary oblique angle can be chosen to unlock the slab excitation and slab phase encoding directions, with reliance on aliasing principles to achieve full image reconstruction of the excited slab. The method thus enables 3D Independent Slab Excitation and Encoding (ISEE) MRI. The immediate application of 3D ISEE is to oblique susceptibility-weighted imaging (SWI), where an oblique excitation of the region of interest can be coupled to image encoding directly aligned with the main magnetic field.

For brain imaging with 3D SWI, pure axial planes tend to be used to ensure the voxel dimension, in the typically larger slab select direction, aligns with the main magnetic field (2). The axial alignment in SWI is due to the fact

---

A version of this work has been filed as a report of invention with the University of Alberta and is currently in process for provisional patent application. Eissa, Wilman.

that SWI utilizes the image phase which is highly dependent on the angle of the rectangular voxel with the main field direction. A major limitation of the axial orientation is the inability to align the volume with the patient's exact anatomy. Most MRI exams are based on anatomical alignment, especially for studies following a time course of disease. The ability to perform accurate oblique SWI would be a substantial advance in the quantitative capability of this method.

3.2 Theory

Before introducing the ISEE method, we review the field perturbations arising around a magnetic dipole aligned with the main field by considering a rectangular paramagnetic cylinder. We shall see that a rectangular area aligned with the dipole will have a pattern of phase/field summation drastically different from the same summation when applied to a rectangular area that has a non-zero angle with the dipole direction (2). The field variation arising from a paramagnetic cylinder can be described by the following equations (3-1, 3-2) derived in reference (2,3):

$$\Delta B_{in} = -4\pi C \chi B_o / 3 \tag{3-1}$$

$$\Delta B_{out} = 4\pi C \chi \cos 2\phi \left(\frac{r^2}{\rho^2} \right) B_o \tag{3-2}$$

where ΔB_{in} is the field difference within the cylinder, ΔB_{out} is the field difference outside, χ is the susceptibility difference between the cylinder and its surrounding tissue, B_o is the static field strength, and C is a constant that contains other non-directional factors such as fractional hematocrit and oxygen saturation in the case of blood. ϕ is the polar angle between the considered position and the

98

static field, r is the vessel radius and ρ is the distance between the position

considered and the center of the blood vessel. Figure 3-1 illustrates the resulting

field perturbations of this cylinder when it lies perpendicular to the main magnetic
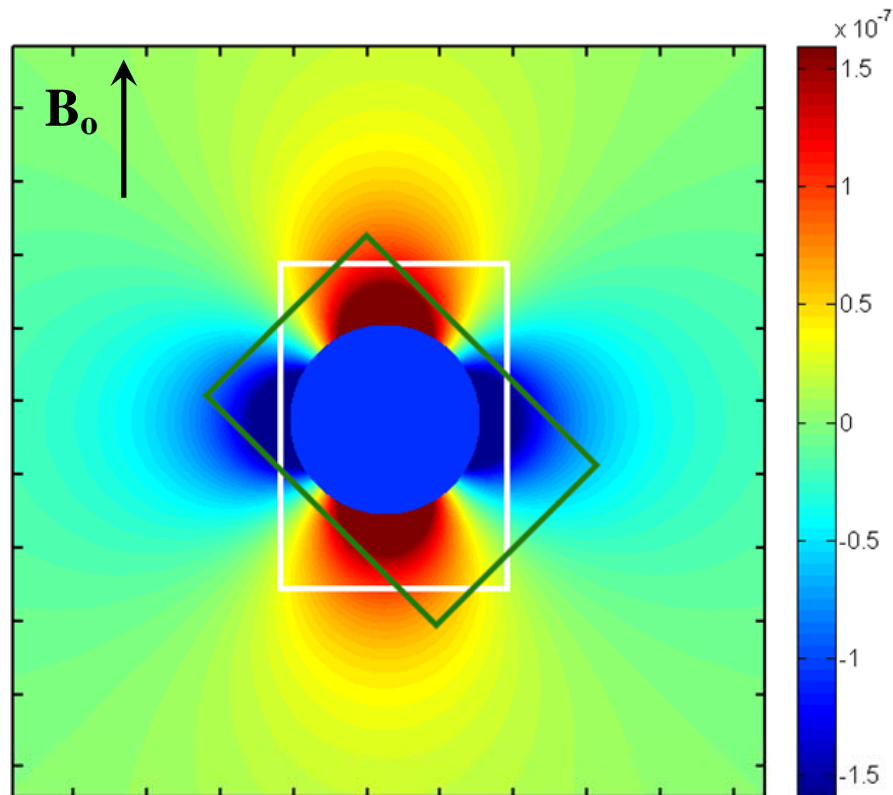
field.

Figure 3-1: Theoretical magnetic field distribution around a long paramagnetic cylinder aligned perpendicular to the static magnetic field. The white rectangle shows a section of a voxel aligned with the field, while the green rectangle shows a voxel at 45° with the static field*.

If the voxel is aligned with the magnetic field (white box), the magnetic

field perturbation is mainly positive, so phase effects in the image will sum up to

give a negative average value for the cylinder containing voxel. However, if the

---

*The specific parameters used to obtain field values in figure 3-1 are B_o = 1.5 T , Y = 60% (as used by Ogawa (3)) and Hct = 47% which is a value that fits in the normal range for Human Male (45-62%) and Human Female (37-48%) (4).

voxel is angled (green box), the summation may lead to cancellation due to negative and positive additions.

In addition, we can see that shifting the white voxel in Figure 3-1 along its longer dimension can affect the summation of the field within it but not drastically enough to change its sign. Thus, this voxel direction can (within a tolerable error) represent the object in the figure and hence, the coherence and reliability of axial phase images are improved (2). The green voxel, on the other hand, can suffer from a drastic change of phase values, including a complete change of the sign with different spatial positioning, while remaining at the same angle with the field.
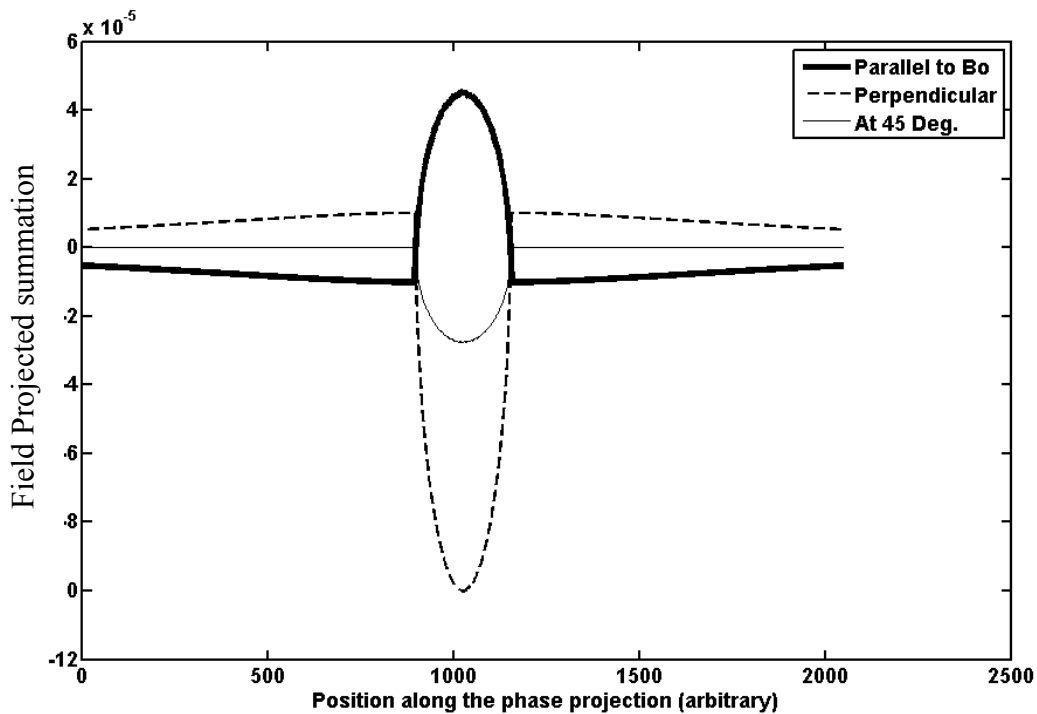
Figure 3-2: Projected summation of the theoretical field distribution along very long pixels in a volume containing a vein perpendicular to the static field with the summation performed along lines at 0º (parallel), 45º and 90º (perpendicular) with the field direction.

Figure 3-2 shows the projected summations of the same field distribution along different directions. It is evident that the direction of summation plays a large role in the resulting phase of the voxel. In the case of field summation applied perpendicular to the main field, higher sensitivity is shown in this particular case. However, if voxel direction is into the page, this mode of summation can cause spatial blurring in the resulting phase image. This mode of summation can also produce higher variability of phase values due to voxel spatial localization offset.

To obtain good contrast from a phase/SWI image, a rod shaped voxel is preferred with the longer dimension lying parallel to the static field (2). The integration of phase along the field direction increases the sensitivity in the resulting image to phase variation within the voxel, as it has a coherent phase sign. In the extreme case of a voxel in which the long dimension lies perpendicular to the magnetic field, the phase sign could be completely reversed. This implies phase cancellation and other erratic behaviors for voxels at varying angles with the magnetic field. This effect is more noted in heterogeneous voxels encompassing different tissue types, as in the case of smaller veins as well as boundaries between different structures. Although we have focused on a cylinder for simplicity, a spherical paramagnetic object would also have lobes aligned with the main magnetic field, but with perpendicular lobes forming a "doughnut" distribution.

In summary, we have seen the major directional dependence of the field perturbation that affects the phase distribution. To avoid severe directional

dependence in SWI, the long dimension of the imaging voxel has typically been chosen parallel to the main magnetic field. This is a substantial limitation for 3D imaging when the slab select direction may need to be angled to conform with patient anatomy, which is the normal practice in clinical MRI. For brain imaging, angulation of the imaging volume is valuable when a limited region is imaged with time efficiency, when patients have limited neck mobility, and when positioning must exactly match previous MRI studies.

3.3 Methods

3.3.1 Pulse Sequence Modifications

The ISEE method involves the application of slab excitation and slab spatial encoding at independent angles. This concept is illustrated in figure 3-3, where the slab excitation is applied to the rectangular area outlined by a solid line. The acquisition volume however, is illustrated by the rectangle outlined by a dashed line. It is well known that imaging signal picked up by the reception coil(s) from outside the prescribed FOV(s) gets mapped to a different or erroneous location within the imaging volume, a phenomenon referred to as aliasing (1). It is generally an undesirable quality in most imaging applications and can happen despite proper placement of imaging volume and RF excitation (5). For 3D ISEE, aliasing is part of the data collection process, where if the aliased data are mapped to an area where no other data exist, reconstruction involves only a simple re-mapping process. However, if aliasing causes any overlap of imaging data, the affected area of the image will be irreversibly

damaged. To allow aliasing of data points only to a location where no other data exist, the slab thickness of the acquisition volume must be changed accordingly.

Previous work has been done utilizing 2D-RF pulses to achieve a non-plane (curved) slice selection (6,7) that is projected onto the readout direction to form a 2D image. The similarity between the 3D ISEE approach and 2D curved slice selection is that both methods can project the Rf excited region onto a plane different from the data origin. However, the 3D ISEE approach uses aliasing and a simple angulation of the slab selection with no alteration in RF pulse shape, as opposed to the complex 2D RF pulse and use of frequency encoding projection in the described curved slice works. Our work is based on simple angular adjustment of the slab selection gradients with and has a performance almost identical to standard Cartesian imaging.
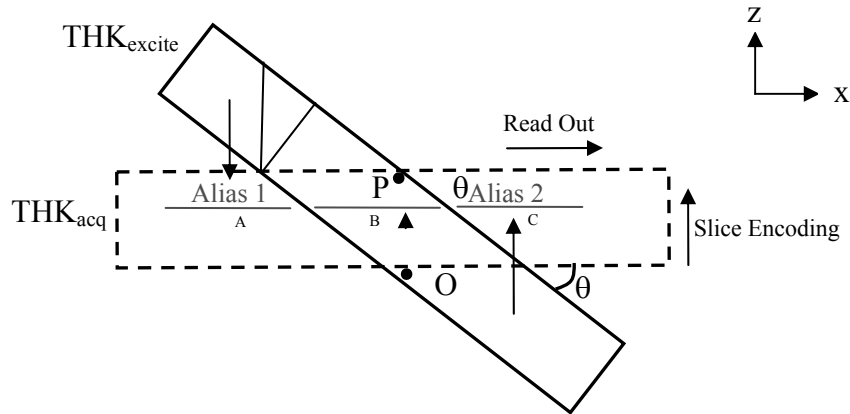
Figure 3-3: Schematic showing the slab excitation volume (solid line) and the image data acquisition volume (dashed line). Note that the field of view (thickness) in the slice direction phase encoding is larger than excitation volume thickness. Points O and P are examples of two data points that might overlap when aliasing occurs. The horizontal lines within the imaging volume mark different image vectors of data, where A is aliased from above the imaging slab, B is positioned in the imaging slab properly with no mapping and C is mapped from sample area below the imaging slab.

The 3D ISEE method can be implemented simply by adjusting the slab selection excitation gradient into multiple components. For a single oblique slice, the main change to the pulse sequence involves separating the slice selection gradient into two components in the x and z directions which are determined by the angle between the slab selection plane and the acquisition plane:

$$G_X = G_{SS} \sin \theta \tag{3-3}$$

$$G_Z = G_{SS} \cos \theta \tag{3-4}$$

where G_X and G_Z mark the read out and slice selection gradients respectively, and G_{SS} is the slice select gradient as set up for the specific excitation slab thickness. A pulse sequence diagram is shown in figure 3-4, where ISEE has been incorporated into a standard 3D SWI sequence. Gradient lobes could be further combined, but for illustrative purposes the encoding and slice select gradients are played out separately.

To validate the method for 3D imaging, phantom experiments were conducted using the pulse sequence in figure 3-4. To further visualize the process, a slice of an image set collected from a phantom is shown in figure 3-5. It resembles the plan illustrated in figure 3-3, where the A and C markings on the image also represent areas aliased from outside the imaging volume.
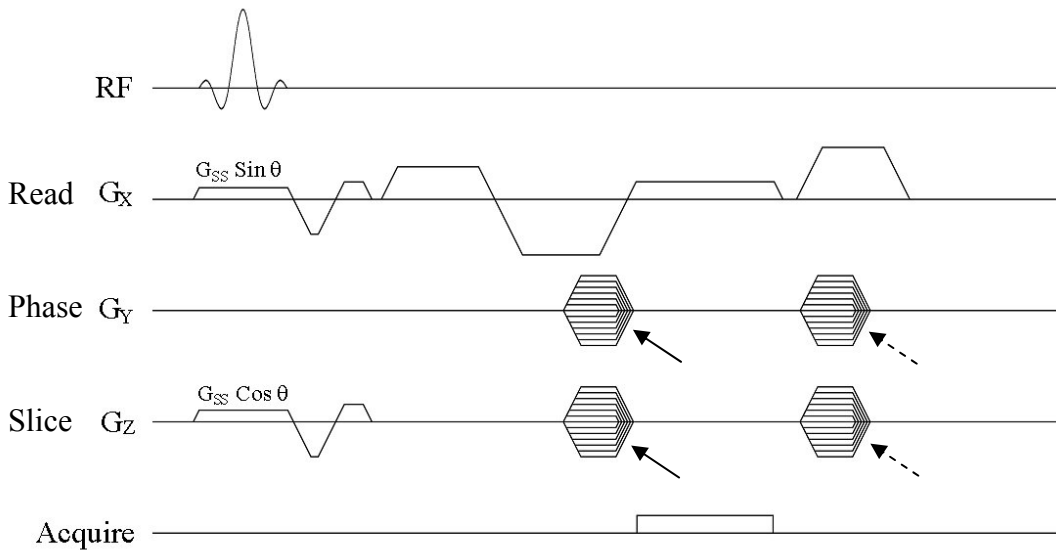
Figure 3-4: Pulse sequence diagram for independent slab excitation and encoding. The sequence is essentially the same as a flow compensated 3D Gradient Echo sequence, with the slab selection gradient as well as its corresponding flow compensation now distributed amongst both X and Z axes according to the angle required between the acquisition volume (lying along the Read-out direction) and the slice selection slab. The solid arrows point at phase encoding gradients while the dashed arrows point at the corresponding phase rewinding gradients.

As an example for this application, it is assumed that an oblique image of the brain is needed which is at a 45º with the anterior-posterior direction. This can best be illustrated in a sagittal view showing the slab selection volume as well as the imaging volume at the stated angle (figure 3-6(a)). On applying this pulse sequence, most of the signal comes from outside the imaging/acquisition volume, which results in aliasing of image portions (segments) back into the imaging volume. Each of these segments will have a vertical height equal to that of the imaging volume. If the desired imaging volume is other than axial, the same concept will apply with the exception that the "vertical" notion will refer to

105
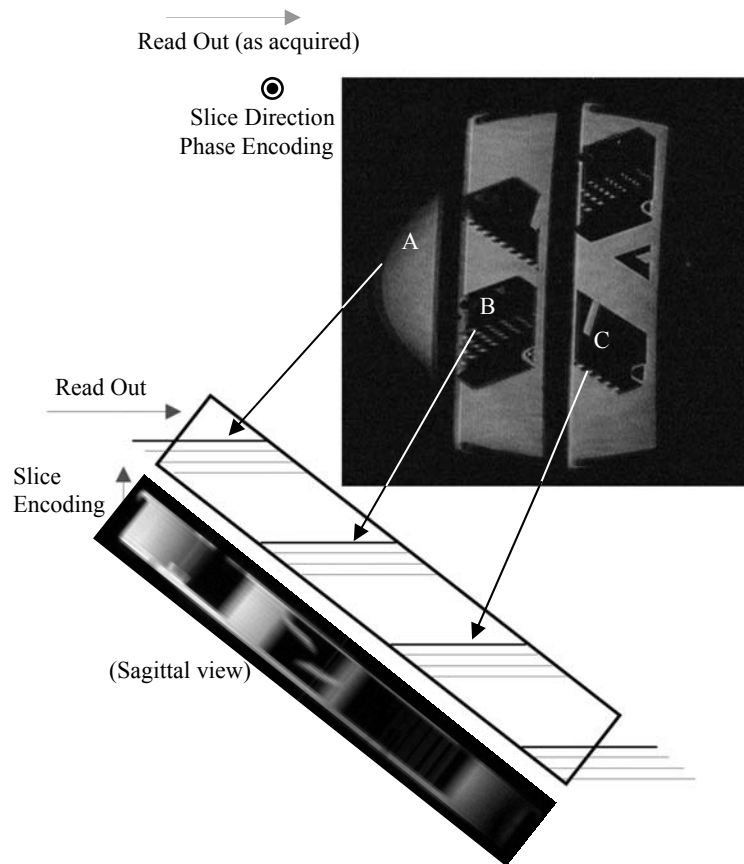
Figure 3-5: Phantom result using the new method. A thin phantom was scanned while placed in an oblique manner inside the head coil. The three sub-slices shown in the image as A,B and C represent same corresponding lines from figure 3-3. The tilted rectangle shows the original slab excitation volume and the arrows from the shown image point to the location where each of the sub-slices came from in the original sample geometry. This suggests the way image data points can be mapped back to their respective proper locations. The gaps or discrete jumps between the sub-slices appear because the acquisition volume thickness was set to be wide enough to separate image points as noted by P and O in figure 3-3. This parameter will be defined later in the text. The picture at the bottom shows a thick sagittal slice close to the middle of the same phantom.

"along the Z-phase encoding direction". In the particular example shown in figure 3-6(b), the assumption was made that the relevant data from the excited area extent until the right and left borders in the schematic (leading to seven different image segments).

106

It must be noted that the schematic dimensions and geometry show an example different from that shown in 3-6(a). Only the segment marked as "1" is a non-aliased segment where the image information appears in the same position as its source tissue. All segments marked with "SS" show the original location of each segment in the image, while segments marked with "Acq" show the correspondingly numbered segments as they appear in the first image set after the scan, a set of axial images where each slice contains multiple axial slices from different locations of the original obliquely excited volume.

The imaging slab thickness depends on both the excitation slab thickness and the angle between the imaging and excitation planes:

$$THK_{ACQ} = \frac{THK_{SS}}{\cos\theta}$$
(3-5)

where THK_{ACQ} is acquisition slab thickness and THK_{SS} is slab selection thickness.

This new thickness is chosen to avoid irreversible aliasing that would take place in the event that any information from two image sub-slices or image segments ('segments' are defined below in figure 3-6) get aliased to the same image location. The same concept was illustrated above in figure 3-3 by the discussion about points O and P and also by emphasizing the image gaps in the main image of figure 3-5. To preserve the originally planned voxel size, an update of the number of slices acquired is needed so that it would increase by the same ratio as the slab thickness:

$$N'_z = \frac{N_z}{\cos\theta}$$
(3-6)

where N'_Z is the new slice number applied in the new method to preserve the resolution and voxel size and N_Z represents the number of slices for the corresponding axial imaging case with the same resolution. It is important to note that N'_Z is rounded up to an integer and then updated in THK_{Acq} accordingly.

3.3.2 Image Reformatting

As a starting point for rearrangement, the image is first shown in the horizontal imaging area in figure 3-6(b). With this image, it is required to reformat into an image set, as shown by the oblique slab selection volume in the same figure.

Reformatting and rearrangement process is presented in figure 3-7 (sagittal view), where a few copies of the same acquired image set are stacked on top of each other (as many as the number of needed image segments). Figure 3-7(a) shows the result of this process where the original slab selection area has been brought back together, as indicated by the black area and the unwanted repeated aliases that are shown in red. The same is illustrated by a brain image set where the number of needed repetitions was three, based on the number of image segments as well as the nature of the anatomy being imaged (note that the non-brain parts show up on the left in figures 3-7(b), (c) and (d)). After stacking the image copies on top of each other as needed (figure 3-7(c)), the extra aliases can be removed, as observed in figure 3-7(d). Figure 3-7(e) shows an overlay of the resulting image on a sagittal brain image from the same volunteer. The image set is then interpolated to set the aspect ratio of the image voxels to the appropriate value (in the XZ plane).

In other words, image voxels are normally aligned in a straight line arrangement in the read out direction. However, the desired slice direction lies at an angle θ with the read out direction. To obtain reformatted slices in any desired direction (say, in the above described oblique direction), the image voxel size in the XZ plane can be manipulated so that the line connecting the centers of each two corner to corner touching voxels lies along the new direction of reformatted slice.
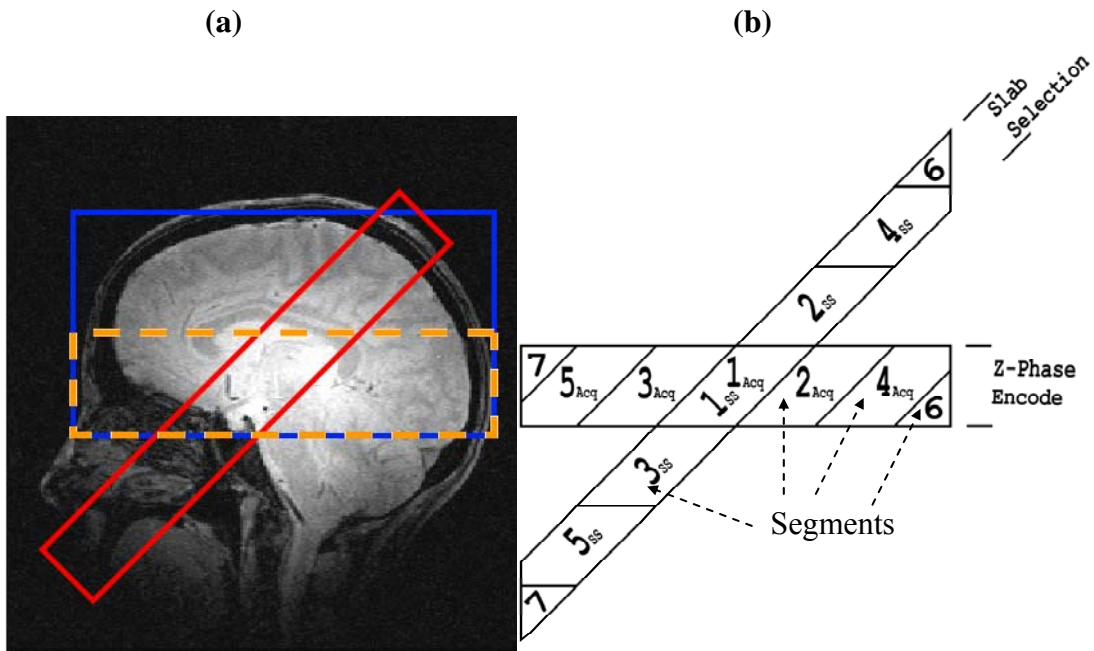
Figure 3-6: Sagittal view showing slab selection performed at an angle different from image acquisition (specifically Z-phase encoding). Slab selection is noted by the tilted red rectangle in **(a)** and as marked in **(b),** while acquisition slab is noted by the dashed orange rectangle in *(a)* and as marked (Z-Phase Encode) in *(b)*. As in the examples shown by the dashed arrows, each enclosed and numbered area is called a 'segment'. The larger blue rectangle in *(a)* shows the alternative slab thickness needed to image the required area of the brain in the traditional axial manner. The numbered areas in *(b)* show the image different segments in their original location (N_{SS}) and as they appear in the acquired image (N_{Acq}), which shows the need to re-arrange these image segments as described in the text. Note that only segment 1 is placed properly in the resulting image.

Hence, to be able to collect image slices along straight lines in the XZ plane, which are also parallel to the slab selection volume and perpendicular to the slab selection direction, the following ratio must be set based on angle θ as follows:

$$\tan\theta = \frac{Voxel\ Height}{Voxel\ Width} \tag{3-7}$$

In the present case, an angle of 45° was used to give an aspect ratio of 1 (isotropic in XZ). The interpolation process can be done by using zero padding, of k-space data, in X and Z, up to the desired number of points in both directions as dictated by the above explained aspect ratio.

Figure 3-8 presents geometrical parameters relating some of the standard imaging parameters and the angle between the slab selection and image encoding planes to illustrate the corresponding parameters applied in the new experimental method in addition to geometrical parameters needed for the image re-formatting process. '*thk*' is the thickness of slab selection, θ is the angle between the imaging slab and the slice selection slab, *thk/sin θ* is the section width which defines the width of each aliased image section, and A, B, C and D are lengths of different line segments. Moreover, S_1 and S_2, which define the number of segments in one half of the read out field of view, can be expressed as follows:

$$S_1 = \frac{1}{2}\frac{FOV_X}{Section\ Width} \tag{3-8}$$

$$S_2 = S_1 + 1 - remainder(S_1) \tag{3-9}$$

110
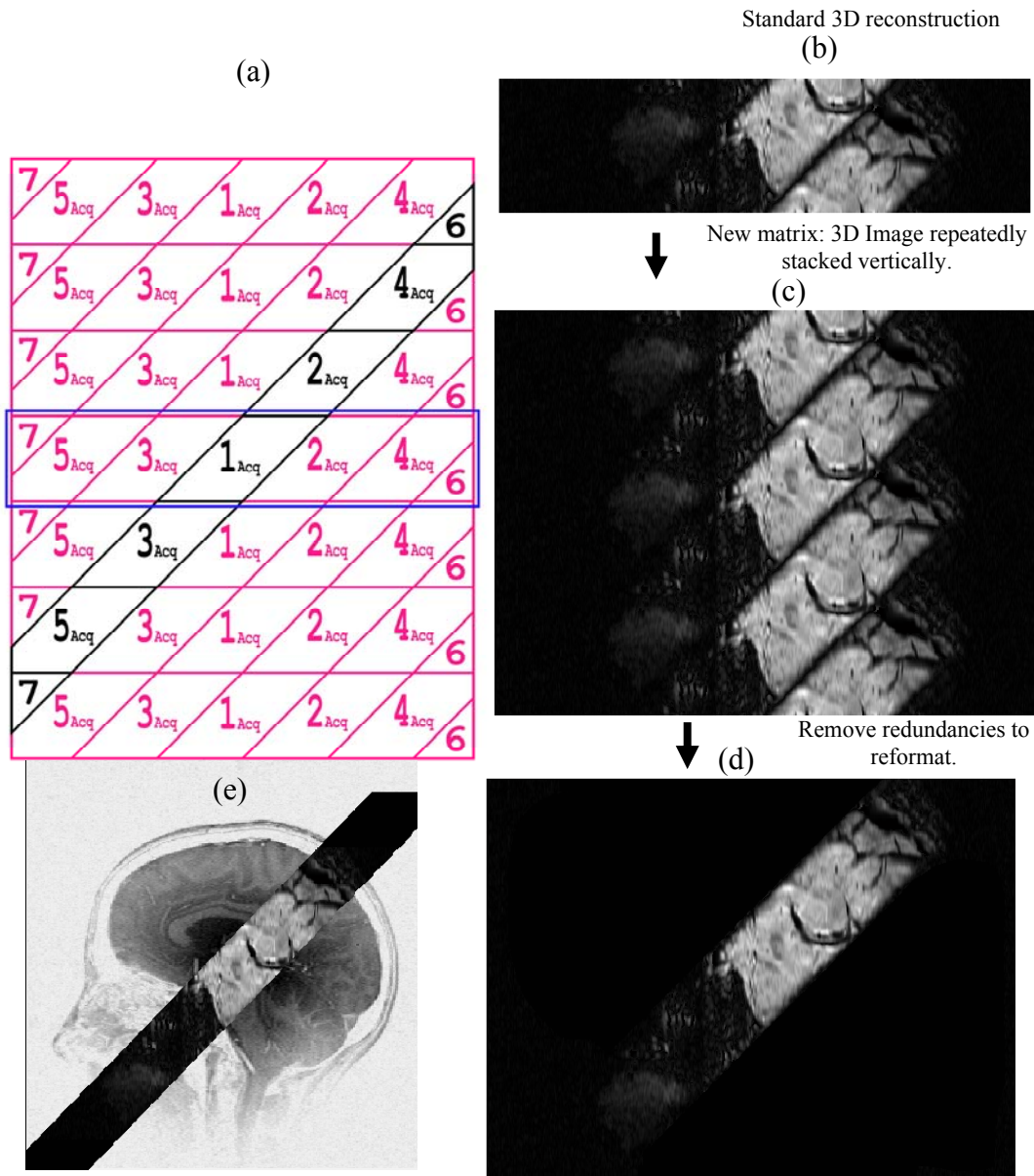
Figure 3-7: (a) Schematic of the acquired image lined by blue rectangle and the proper arrangement (as original slab selection) shown in black color. This schematic assumes that all the shown segments contain important image data, which is not always the case. The image is repeatedly stacked on top of itself to connect the segments (7,5,3,1,2,4,6) as shown. All repeated segments shown by magenta color will then be discarded. Next subfigures show the same concept applied to another imaging case where the geometry is different and the stacking process is repeated only three times, since the left segments of the acquired image lie either in air or unimportant anatomy (outside the brain). **(b)** A human image where the sagittal view of the acquired image is shown (corresponding to the blue box in **(a)**). **(c)** A sagittal view showing three sets of the same image from *(b)* stacked on top of each other. **(d)** The same image from *(c)* after discarding unnecessary aliases. **(e)** The image result from *(d)* after superimposing it on an inverted sagittal image for the same volunteer.

If the segments are counted using the upper side, this count will miss segment "6", since it has no contact with the upper side. To account for this segment, the addition of the value of 1 is included in the following equation:

$$S_{total} = 2S_2 + 1 \qquad (3\text{-}10)$$

Moreover, the line segments A, B and C in Figure 3-8 can be expressed as follows:

$$A = \text{Remainder}(S_1) \text{ x section width} \qquad (3\text{-}11)$$

$$B = A \tan\theta \qquad (3\text{-}12)$$

$$C = \frac{thk}{\cos\theta} - B \qquad (3\text{-}13)$$

Figure 3-8: Schematic showing a magnification of the lower left corner in figure 3-7(a) to show different significant dimensions relating to slab thickness determination and the re-formatting process. Definitions follow below. To prevent irreversible aliasing in the Z direction, we must apply a new value to the Z field of view to match the distance between slab selection volume edges measured in the direction of planned acquisition (vertical blue line).

112

$$N_C = N_{Zacq} \cdot \frac{C}{\left(\dfrac{thk}{\cos\theta} \right)} \qquad\qquad (3\text{-}14)$$

where N_C is the number of data points in the acquired slice direction along the length of 'C'. N_{Zacq} is the acquisition slice number.

$$D = thk \cdot \sin\theta \qquad\qquad (3\text{-}15)$$

where D is the length outside the imaging solume that can be filled with zeros to offer a simple-to-reformat data matrix.

$$N_{DX} = D \cdot \frac{N_X}{FOV_X} \qquad\qquad (3\text{-}16)$$

where N_{DX} is the number of data points in the length of D, N_X is the number of data points in the acquired read-out direction and FOV_X is the field of view in the read-out direction.

The image matrix is then padded both on the left and the right side (of the sagittal view) by N_{DX} zeros zone.

After the zero padding process, a new matrix size is defined. In the new matrix structure, the point 'c' at the top of the line segment 'C' has an X coordinate of $N_{DX} + 1$ and a Z coordinate of N_C.

Hence, the new slice length, N'_X, becomes:

$$N'_X = N_X + N_{DX} \qquad\qquad (3\text{-}17)$$

The rearranged slices are mapped starting from point 'c' where the slice is read as vectors (into the page) and where each subsequent vector is located by incrementing both X and Z indices by 1 until the new slice length is reached.

The next slice starting location is defined by incrementing Z by 1 while decrementing X by 1. The new value FOV'$_Z$ is calculated from:
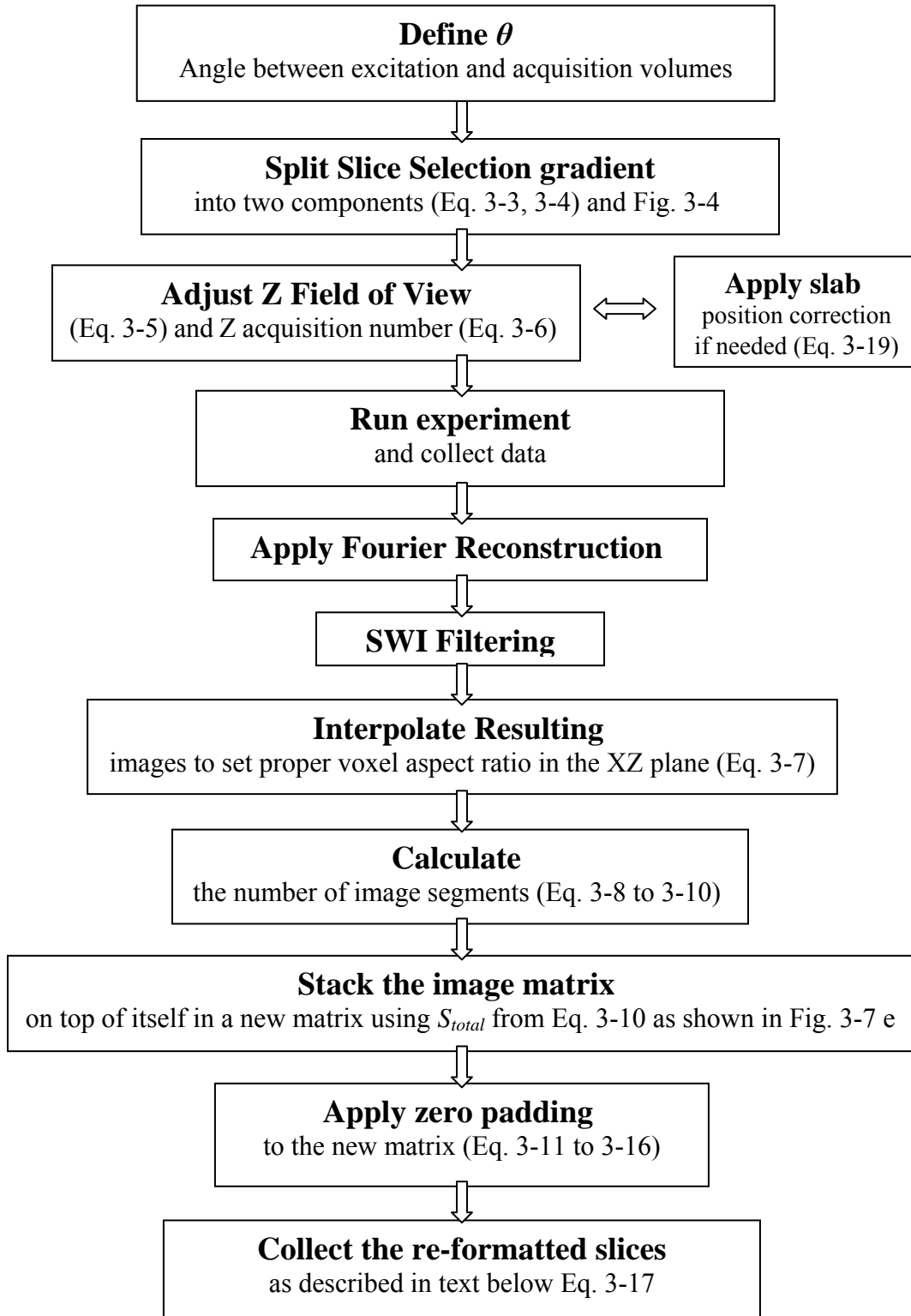
$$FOV_Z^{'} = \frac{thk}{\cos\theta} \qquad (3\text{-}18)$$

This new imaging volume is shown by the dashed orange box in figure (3-6 a), where the "narrower" red box shows the slab selection volume. This value is always larger than *thk* for any angle greater than zero (i.e. $\theta > 0^o$).

To achieve the same voxel size as the standard axial method, the Z phase encoding number must be increased, which in turn leads to a proportional increase in scan time. This increase in scan time is justified by the fact that, in order to acquire the same volume axially, an even larger sample volume must be included, as illustrated by the blue box in figure 3-6(a). The blue box covers all the relevant brain area where the oblique slab traverses the brain. In other situations, this box can be even thicker had there been a need for the image information from the mouth and sinuses in this specific case. In other words, the maximum expected increase in scan time is determined by the separating angle, slab selection thickness and the extent of relevant anatomy along the main field direction.

Figure 3-9 shows Flow chart demonstrating the application of the new method starting with pulse sequence changes until obtaining the final reformatted images.

114

Assuming experimental parameters are adjusted for standard imaging.

Define *θ*
Angle between excitation and acquisition volumes

⇓

Split Slice Selection gradient
into two components (Eq. 3-3, 3-4) and Fig. 3-4

⇓

Adjust Z Field of View
(Eq. 3-5) and Z acquisition number (Eq. 3-6) ⟺ **Apply slab** position correction if needed (Eq. 3-19)

⇓

Run experiment
and collect data

⇓

Apply Fourier Reconstruction

⇓

SWI Filtering

⇓

Interpolate Resulting
images to set proper voxel aspect ratio in the XZ plane (Eq. 3-7)

⇓

Calculate
the number of image segments (Eq. 3-8 to 3-10)

⇓

Stack the image matrix
on top of itself in a new matrix using S_{total} from Eq. 3-10 as shown in Fig. 3-7 e

⇓

Apply zero padding
to the new matrix (Eq. 3-11 to 3-16)

⇓

Collect the re-formatted slices
as described in text below Eq. 3-17

Figure 3-9: Flow chart showing the application of the new method starting with pulse sequence changes until obtaining the final reformatted images.

115

3.3.3 Experimental Procedure

The ISEE method was implemented on a 4.7 T research MRI Scanner (Varian, Palo Alto, CA) and two different sets of experiments were executed on phantom as well as healthy volunteers.

Phantom experiments involved scanning a thin phantom placed obliquely at about 45º with the static field where the phantom was imaged twice; *A)* Applying a standard oblique scan (aligned with the phantom structure and thus expected to yield "axial looking" images). *B)* Applying the ISEE method with slab selection identical to the "*A)*" (at 45º with B_o) and an axial encoding volume.

Further Experimental parameters:

A) **TE/TR** 6/70 ms. **Spectral width** 100 kHz. **Flip angle** 20º. **Excitation slab thickness** 0.66 cm. **FOV$_X$** 20.5 cm, **FOV$_Y$** 21 cm, **FOV$_Z$** 0.8 cm

B) **TE/TR** 6/70 ms. **Spectral width** 100 kHz. **Flip angle** 20º. **Excitation slab thickness** 0.66 cm. **FOV$_X$** 14.9 cm, **FOV$_Y$** 21 cm, **FOV$_Z$** 1.13 cm

The above scan *B* was followed by reformatting the resulting images to retrieve image slices similar to those produced in scan *A*.

Five healthy volunteers were scanned using the same pulse sequences with three scanning sessions applied to each volunteer. All three experiments were adjusted to include the Red Nucleus and Subtantia Nigra in the imaging volume. These deep gray matter structures are known for their iron content and hence their expected contrast, with background tissue, in SWI phase images. The three scanning protocols were as follows:

Phantom experiments involved scanning a thin phantom placed obliquely at about 45º with the static field where the phantom was imaged twice;

A) Applying a standard axial SWI scan.

B) Applying a standard oblique scan of an oblique slab in the brain which is at 45º with the main field (as shown in figure 3-7 e).

C) Applying the ISEE method with slab selection identical to *B* (at 45º with B_o) and an axial encoding volume.

Further Experimental parameters:

A) **TE/TR** 15/35.7 ms. **Spectral width** 35 kHz. **Flip angle** 11º. **Excitation slab thickness** 4 cm. **FOV$_X$** 22.2 cm, **FOV$_Y$** 16.1 cm, **FOV$_Z$** 4.4 cm **Slice thickness** 2 mm (N_X . N_Y . N_Z = 512 . 256 . 22)

B) **TE/TR** 15/35.7 ms. **Spectral width** 35 kHz. **Flip angle** 11º. **Excitation slab thickness** 4 cm. **FOV$_X$** 22.2 cm, **FOV$_Y$** 16.1 cm, **FOV$_Z$** $\boxed{4.4}$ cm **Slice thickness** 2 mm (N_X . N_Y . N_Z = 512 . 256 . $\boxed{22}$)

C) **TE/TR** 15/35.7 ms. **Spectral width** 35 kHz. **Flip angle** 11º. **Excitation slab thickness** 4 cm. **FOV$_X$** 22.2 cm, **FOV$_Y$** 16.1 cm, **FOV$_Z$** $\boxed{6.4}$ cm **Slice thickness** 2 mm (N_X . N_Y . N_Z = 512 . 256 . $\boxed{32}$)

Each of the above resulting image sets was processed to produce SWI phase images by applying a high pass filter to the complex image data. The processing method has been explained in previous work (8,9). Results from experiment *C* were reformatted (as described earlier) to retrieve image slices similar to those produced in scan *B*.

3.4 Results

The 3D ISEE method was tested on phantoms and five normal volunteers. The results from phantom imaging verified the performance as observed in figures 3-5 and 3-10, where the method showed multiple sub-slices per source image. The re-mapping process was also applied to phantom results successfully, as illustrated in figure 3-10.

(a) **(b)**
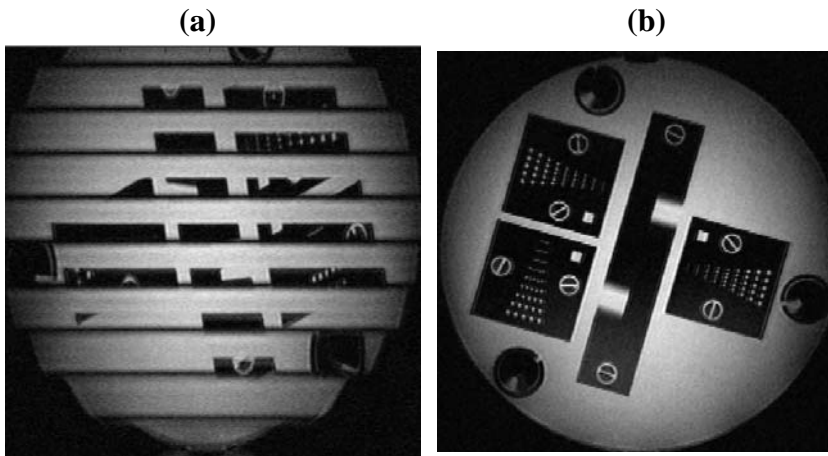
Figure 3-10: Phantom results showing an acquired aliased image slice (a) and a corrected/reformatted slice from the same dataset (b). The ISEE method was used on a thin phantom placed at 45º with the main field (phantom was placed obliquely). Excitation was applied to partial thickness of the phantom at the same oblique angle. Acquisition on the other hand was applied to an axial volume (axial encoding).
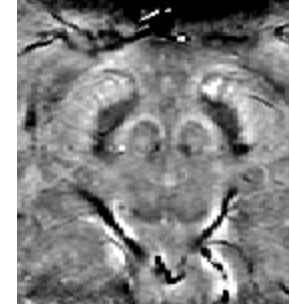
Standard Axial   Standard Oblique

A   B

C   D

ISEE   (C "dataset") re-formatted to (D)
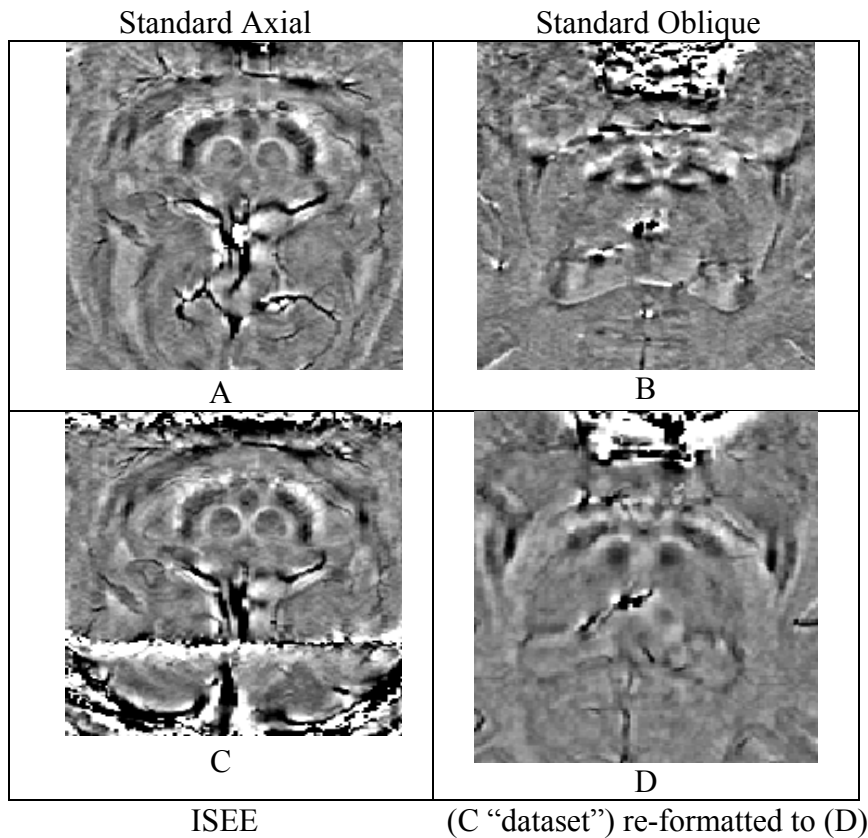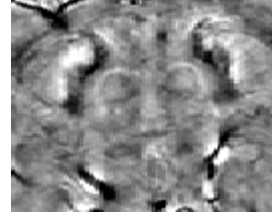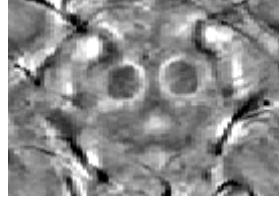
Figure 3-11: Results from different imaging methods (A) Axial Image; (B) Traditional Oblique Image; (C) Oblique Slab Selection with Axial Acquisition; (D) Same Image set as "(C)" after re-formatting to the oblique plane.

By scanning the same volunteer using the different variants of traditional axial, traditional oblique and the new method's "oblique excitation with axial acquisition", it is apparent from figure 3-11 that the traditional oblique method produces a qualitatively different phase image, whereas the new method (ISEE) resulted in restoring the contrast and phase color level to that expected from a proper axial scan. Figure 3-11(c) shows a phase image with preserved contrast that is comparable to the axial image in figure 3-11(a).

Example results from three additional volunteers are shown in figure 3-12. The same above conclusions are evident in all three cases.

119

Volunteer Number	Axial	Traditional Oblique	New Method
4			
5			
6			

Figure 3-12: Phase images of Substania Nigra and Red Nucleus from three different volunteers. For each volunteer, an axial image is shown to demonstrate standard SWI contrast (left column) and another image shows the deterioration in contrast in case of traditional oblique imaging (middle column) while the third image shows the restoration of standard SWI contrast when using the new method (right column).

The resulting images require rearrangement and re-formatting in order to appear in the usual oblique fashion. The above concept is perhaps more obvious on examining the red nucleus areas in the images. ROI measurements have been

applied to the red nucleus area as well as Substantia Nigra and average phase measurements were obtained for each imaging variant.

The purpose of the ROI measurements is to examine the SWI contrast performance of each imaging variant. Both structures are expected to have stronger negative contrast with their surroundings in the SWI image as opposed to the magnitude image. Figure 3-13 shows an example of ROI placement on red nucleus, substantia nigra and background.
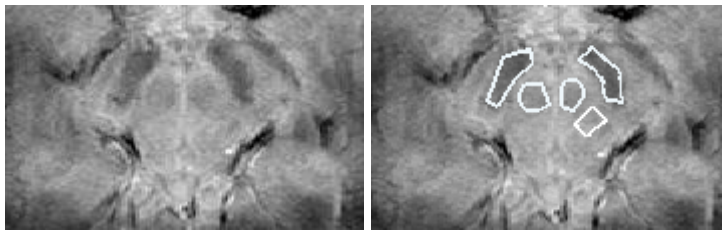
Figure 3-13: Two identical images are presented, with a sample ROI placement superimposed on the image on the right. The top two ROIs are placed on Substantia Nigra, followed by two ROIs placed on Red Nucleus, while the ROI at the bottom is placed for background measurement.

The plots in figure 3-14 present the quantitative results of the above measurements and verify the loss of contrast in the case of traditional oblique imaging, where the SWI normalized contrast is lower than magnitude normalized contrast. However, the new method "axial acquisition with oblique excitation" shows the restoration of SWI normalized contrast being more negative than magnitude normalized contrast.

Comparison of SWI contrast results for different imaging methods

a. Red Nucleus (RN)
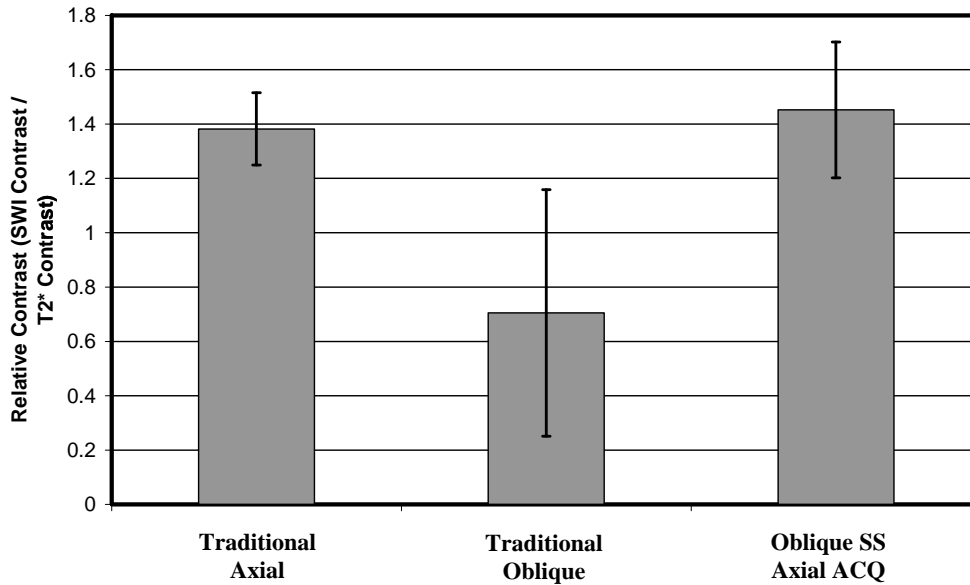
b. Substantia Nigra (SN)
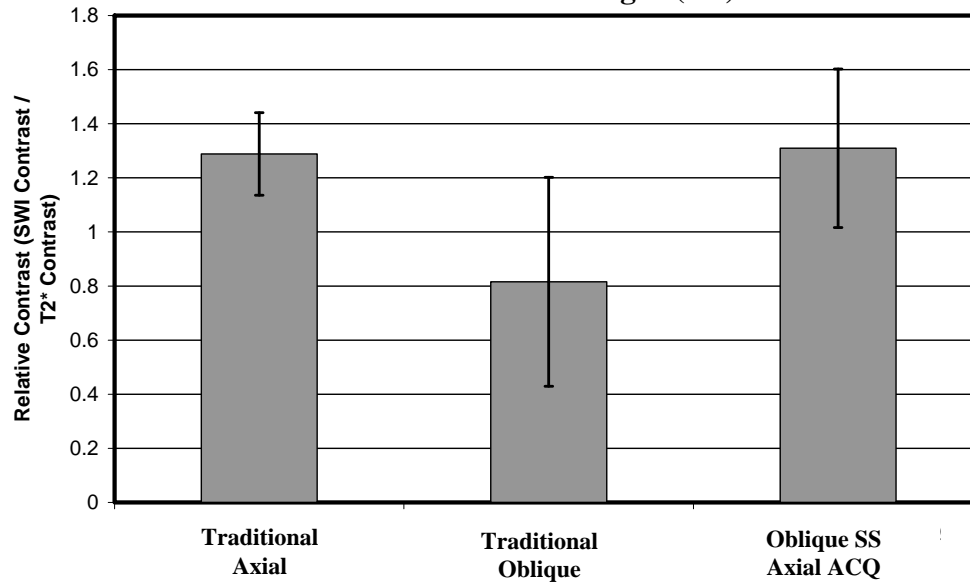
Figure 3-14: Experimental results from five volunteers comparing different imaging techniques. The average values shown in histogram bars represent the ratio of the contrast from the processed SWI image to the contrast from the corresponding unaltered magnitude image. Contrast results are depicted as normalized contrast (ROI − Background)/Background. Three bars represent the noted imaging method with "traditional oblique" showing loss of contrast in the SWI image. However, the other two methods show the desired enhancement of SWI contrast over the magnitude image. **a:** shows results from the Red Nucleus region while **b:** shows results from Substantia Nigra.

3.5 Discussion

It is worth noting that the same pulse sequence changes are applicable to 2D imaging without the need for re-slicing as no Z-aliasing is applicable to the 2D methods.

On examining figure 3-14, the results from the new method have almost the same mean value as the standard axial SWI. However, the standard deviation is higher in the current results for the new method. This might seem counterintuitive because the longer scan time in the ISEE method is rightfully expected to increase the SNR in the resulting images. This effect might be due to the application of SWI post-processing to the acquired image before re-formatting which led to the high pass filter encountering more sudden changes across the thinner sub-slices in each axially acquired slice. This should not be a concern because it is possible to apply SWI post processing after re-formatting the images to the oblique plane. However, for comparison purposes, it was important to validate the new method's results against the standard axial SWI results and hence the application of SWI post-processing using the former approach.

The ISEE method can be applied the same way to any mode of angulation or obliqueness from either or both phase encoding directions. The current work was applied to the slab phase encoding direction due to the geometrical feasibility where the field of view in this direction is usually smaller than the field of view in the read out direction.

An alternative to this approach to the described pulse sequence design would be keeping slice selection as one simple pulse while splitting the read out

gradients into two components and doing the same to the Z-phase encoding gradients. This approach would be more complicated than the one presented in the current work.

In conclusion, a new method has been developed and explained for 3D imaging with an application that allows for standard transverse encoding for SWI phase summation parallel to the main magnetic field, and that also allows for oblique angle excitations.

3.6 References

1- Haacke EM, Brown RW, Thompson MR, Venkatesan R. Magnetic resonance imaging physical principles and sequence design. New York:John Wiley & Sons; 1999.

2- Xu Y, Haacke EM. The role of voxel aspect ratio in determining apparent vascular phase behavior in susceptibility weighted imaging. Magn Reson Imag. 2006; 24:155-160.

3- Ogawa S, Lee TM, Kay AR, Tank DW. Brain magnetic resonance imaging with contrast dependent on blood oxygenation. Proc Natl Acad Sci U S A 1990;87:9868– 72.

4- www.BloodBook.com

5- Wilman AH, Riederer SJ. On the cause of increased aliasing in the slice-select direction in 3D contrast-enhanced magnetic resonance angiography. Magnetic Resonance in Medicine (2000); 44:336-338.

6- Bornert P, Shaffter T. Curved Slice Imaging. Magnetic Resonance in Medicine (1996); 36: 932-939.

7- Peter Bornert. 2D-RF-pulse-encoded curved-slice imaging. MAGMA (2003); 16: 86-92.

8- Haacke, EM, Xu, Y, Cheng, YC, Reichenbach, JR. Susceptibility weighted imaging (SWI). Magn. Reson. Med. 2004; 52:612–618.

9- Eissa A, Lebel RM, Korzan JR, Zavodni AE, Warren KG, Catz I, Emery DJ, Wilman AH. Detecting Lesions in Multiple Sclerosis at 4.7 Tesla Using Phase Susceptibility-Weighting and T2-Weighting. JMRI 30(4); 737-742, 2009.

Chapter 4

Effects of RF Inhomogeneity at 3.0 T on Ramped RF

Excitation: Application to 3D Time-of-Flight MR

Angiography of the Intracranial Arteries

4.1 Introduction

The application of three-dimensional time-of flight MR angiography (3D-TOF-MRA) at 3.0 T has two promising advantages over 1.5 T: increased signal-to-noise ratio (SNR) and improved background suppression due to longer T_1 values at 3.0 T (1,2). Nevertheless, 3.0 T has the shortcoming of a less homogeneous RF field distribution. This arises from the shorter RF wavelength, which can lead to destructive RF interference that causes a significant RF field focusing effect (3–7). These RF interference effects arise from the decreasing RF wavelength with increasing static field. At 3.0 T the half wavelength is approximately 14 cm, which is smaller than the head dimensions (3). This reduced wavelength is the primary result of the dielectric properties of brain tissue, which lead to an RF wavelength that is more than seven times shorter than the wavelength in air at 3.0 T. In overly simple terms, the interference effect arises because the RF field at any given point in the tissue is a summation of multiple traveling waves produced by each portion of the coil. When the wavelength is short, the summation may lead to destructive interference if the

---

path length of each wave component varies. At 3.0 T, RF variation across a thick axial 3D slab in the human head can be as much as 40% when the independent RF variations along both axial and superior–inferior dimensions are combined (3,6). Thus, when RF excitation is designed to deliver a specific flip-angle distribution over space at 3.0 T, these interference effects must be considered.

However, the effects of RF destructive interference have not previously been considered for MRA. Unlike static tissue, the flowing blood will pass through a range of flip angles over its path, making the response to a varying RF distribution somewhat more complex. Furthermore, in intracranial 3D-TOF-MRA, a ramped RF excitation is typically used with precise flip-angle variation over space. The ramped excitation uses increasing RF excitation as the blood advances through the slab, which has been shown to enhance the blood signal at lower fields (8–10). Although this method is also effective at 3.0 T, the actual profile received deviates substantially from that expected, owing to RF destructive interference. Specifically, the RF interference effect at 3.0 T leads to a reduced RF field as one moves outward from the center, which is the path of the middle and posterior cerebral artery branches that extend from the circle-of-Willis.

The purpose of this work is to investigate both theoretically and experimentally the effects of RF inhomogeneity on the response to ramped RF excitation at the clinical field strength of 3.0 T, with application to 3D-TOF-MRA of the intracranial arteries. In addition, a simple solution of applying a steeper ramp slope is shown to lead to significant enhancement over a standard

ramp pulse for the distal middle and posterior cerebral arteries. The benefits of the new method are shown in both simulation and normal volunteer experiments at 3.0 T.

4.2 Materials and Methods

### 4.2.1 Theory

The theoretical description of RF inhomogeneity in the human head has been well addressed in simulations and shown to be quite accurate experimentally (6,11– 13). We determined the theoretical RF field distribution over the human head at 3.0 T using results supplied by Collins and Smith (14) for a circumscribing 16-element RF birdcage coil. The effects of field distribution on ramped RF excitation are shown in Fig. 4-1. Figure 4-1a illustrates the coronal projection of a typical transverse volume for intracranial 3D-TOF-MRA, while Fig. 4-1b shows the normalized RF distribution at 3.0 T. This must be multiplied by the ramp RF variation shown in Fig. 4-1c to yield the actual RF distribution in Fig. 4-1d. Clearly, the distribution in 1d differs substantially from the applied RF ramp profile of Fig. 4-1c. For comparison, Fig. 4-1e shows a 50% steeper ramp profile combined with the same RF inhomogeneity profile. To theoretically address the effects on blood-to-background contrast, we assumed a straight diagonal artery. This diagonal artery is overlaid on the 3D TOF image in Fig. 4-1a and roughly represents a middle cerebral artery pathway. The RF distribution along that artery was calculated for various RF pulse profiles.

Using the Bloch equations, we performed a simulation to test the effect of increasing ramp slope on blood-to-background contrast for 3D-TOF-MRA at

3.0 T along the considered pathway of blood. Figure 4-2 shows three different ramp pulses that were considered, as well as the effective flip angles received by the diagonal blood vessel for each ramp profile. The ramp pulse profiles are shown with and without considering the effects of RF destructive interference. Without the interference effects, the applied flip angle varies linearly for the three cases shown in Fig. 4-2a: 15–35° (standard ramp), 10– 40° (ramp1.5) and 5–45° (ramp2), where the 1.5 and 2 are the factors by which the standard ramp slope was multiplied while maintaining the average flip angle at 25° in the three cases. When RF interference effects are considered, we must specify the artery path, and therefore we use the generic diagonal artery of Fig. 4-1a. This results in the adjusted RF profiles shown in Fig. 4-2b. To investigate the feasibility of other pulse shapes, we also considered a simple linear two-stage ramp for theoretical investigation. It starts at a 10° flip angle, increases linearly to 20° at the middle of the slab, and then increases linearly but at a higher slope to 45° at the slab superior end. This pulse shape will be referred to as "2-stage."

The diagonal vessel, as illustrated in Fig. 4-1a, was defined as a straight line from the center of the inferior slice to the edge of the superior slice of a 6.4 cm axial slab in the brain with a path length of 10 cm. This diagonal vessel serves as a rough approximation of a middle cerebral artery, emanating from the circle-of-Willis and proceeding outwards. A similar pattern of RF field distribution can also be shown along a vessel ascending toward the posterior of the brain, in the manner of a posterior cerebral artery. This is due to the RF fall-off occurring
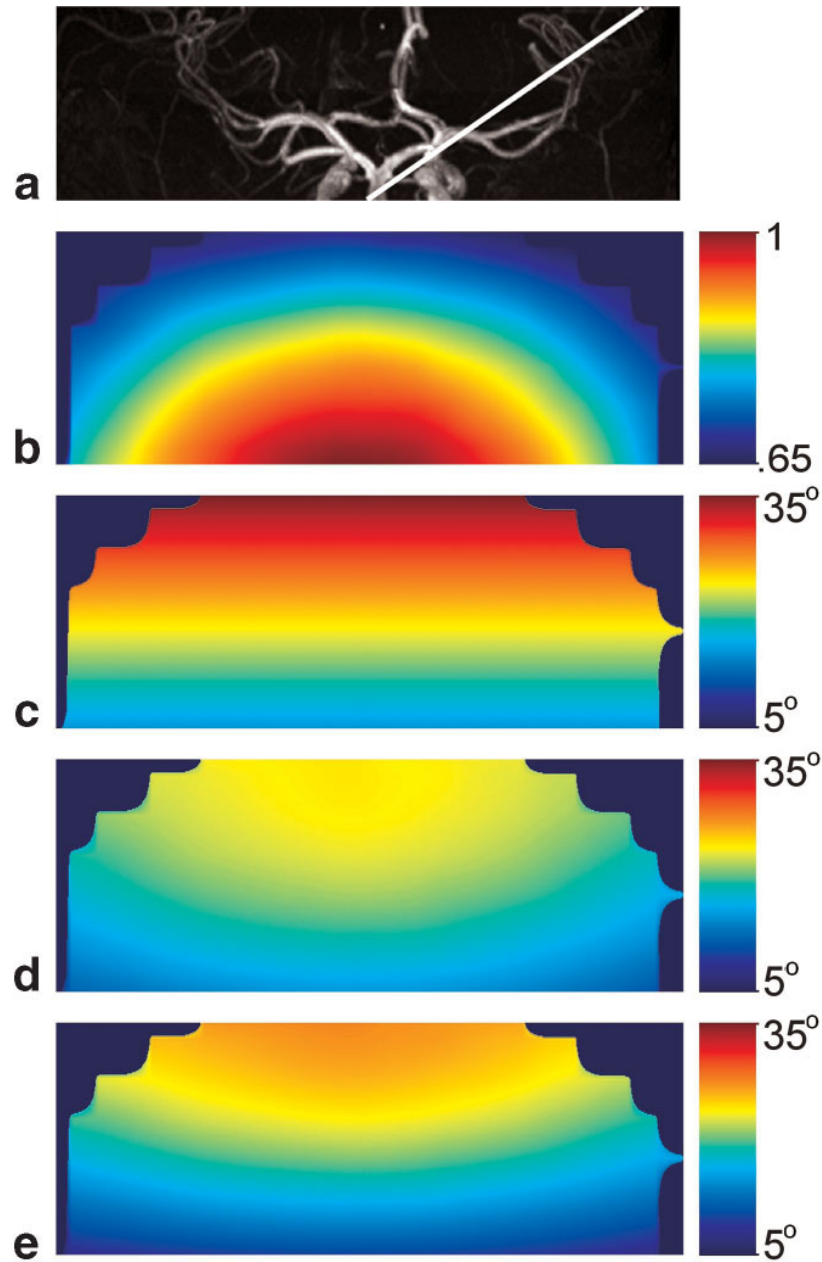
Figure 4-1: Coronal views of RF field variations in the brain at 3.0 T. **a:** A coronal MIP from a 3D-TOF acquisition, illustrating the hypothetical straight diagonal artery used in the simulation. **b:** The RF distribution due to RF inhomogeneity arising from RF destructive interference. **c:** The ideal ramp pulse coronal distribution without the effects of the RF inhomogeneity. **d:** The same ramp pulse after the RF inhomogeneity effect in b was applied to its distribution from c. e: The RF distribution, including RF inhomogeneity, for a 1.5 times steeper ramp pulse.

130
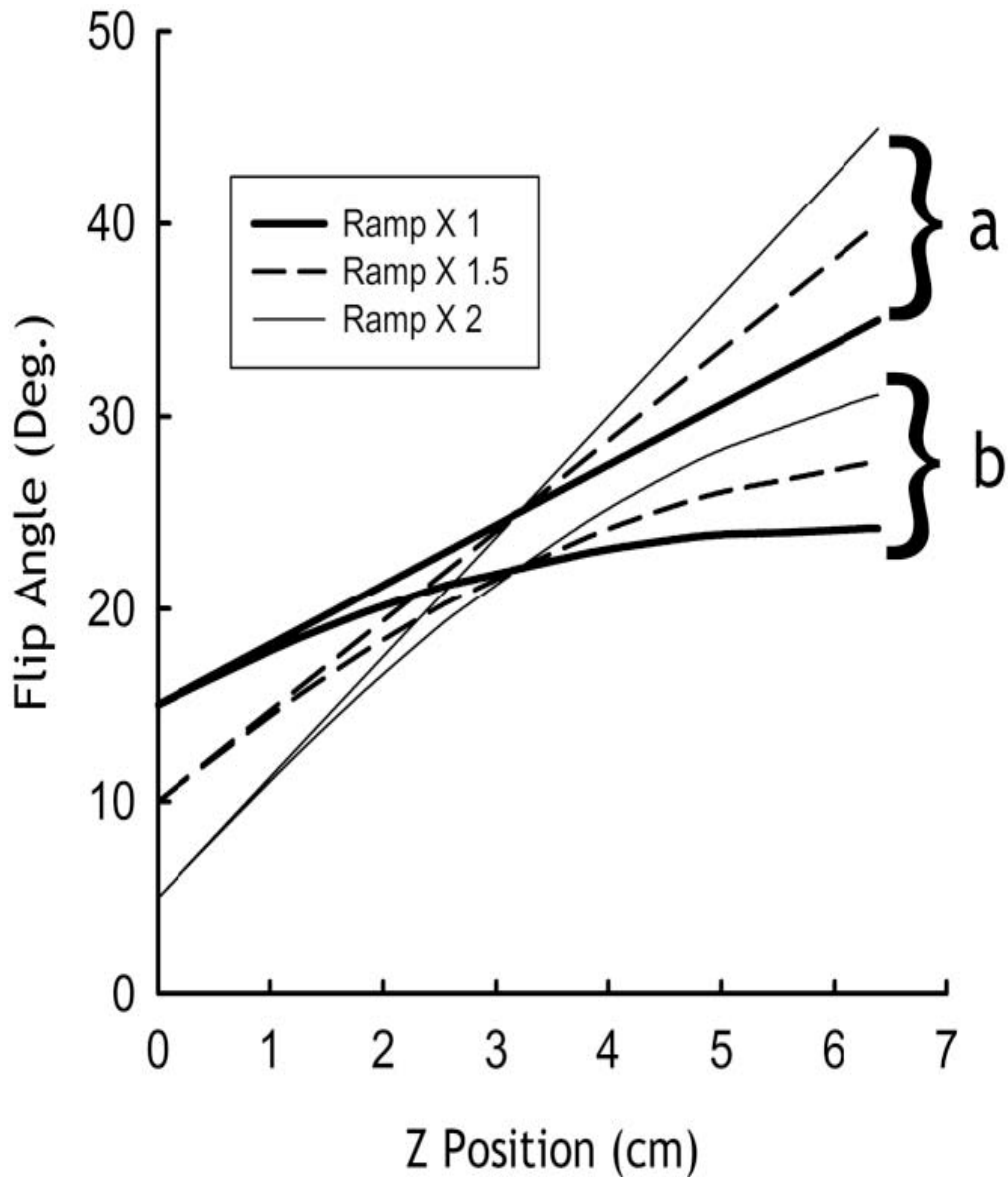
Figure 4-2: A graph illustrating the flip angle received vs. superior–inferior (z) position within the 3D slab. **a:** Applied RF frequency profile without the RF inhomogeneity effect. **b:** Actual RF profile at 3.0 T along the diagonal artery. The three applied RF profiles had an average flip angle of 25°.

toward the edges of the brain (specifically laterally and posteriorly). Blood speed

within the vessel was assumed to be constant along the vessel pathway, and three

values for speed were considered (5, 10, and 20 cm/second).

131

The above stated slow speeds were used to simulate typical patient populations. Other parameters used in the simulation included a TR of 36 ms and 64-mm slab thickness, which match the experimental parameters. For the simulation, the T_1 times used for 3.0 T were as follows: 1330 ms for gray matter (GM), 830 ms for white matter (WM) (15), and 1260 ms for blood (1). Transverse relaxation was ignored owing to the short experimental TE and the use of spoiling between TR times.

4.2.2 Experimental

The experimental 3D-TOF protocol was applied to eight healthy male volunteers (mean age = 27.4 ± 4.2 years) to image the circle-of-Willis and distal intracranial vessels. The volunteers provided written informed consent before the studies were conducted. Experiments were conducted at 3.0 T using a circular, 27-cm diameter, 16-element, cylindrically shaped birdcage coil for transmission and reception. All techniques used an average flip angle of 25° with TE/TR = 7/36 ms, 64 slices of 1–1.2 mm thickness, one slab, 512 x 256 in-plane resolution, and 200 x 200 mm square FOV. The 3D-TOF sequence used zeroth- and first-moment flow compensation applied both for the read and slice-selection gradients. A standard ramp pulse was first applied with flip angles varying linearly from 15° to 35°. We then varied the ramp pulse slope by increasing the imaginary part of the RF pulse to achieve a 1.5 and 2.0 times increased slope while maintaining the same average flip angle of 25°. The above was an empirical solution used to simplify sequence programming. The resulting RF profiles were verified experimentally to work as expected.

Experimental analysis of the images involved tracing a number of blood vessel pathways and making region of interest (ROI) measurements with an in-house-developed program (Matlab$^{\text{TM}}$, Mathworks Inc.). For detailed ROI analysis we chose six cases in which the blood vessel trajectory was close to the simulated artery and traversed the whole imaging slab. For each blood vessel, at least four ROIs were distributed along its length. Between successive scans, the anatomical features of the vessels were used to center the ROIs to avoid errors from any potential slight shift in positioning. Blood-to-background contrast (blood intensity – background intensity) was calculated for each region considered. We measured the noise by taking the standard deviation (SD) of an ROI that lay outside the image region in air. The contrast-to-noise ratio (CNR) was defined as the (blood – background)/noise. In addition, a measure of normalized contrast:

$$(blood – background)/background \text{ was also used.}$$

4.3 Results

The resulting blood-to-background normalized contrasts are illustrated in Fig. 4-3 for GM as background, using blood velocities of 10 and 20 cm/second. Corresponding results for WM are shown in Table 4-1 for blood speeds of 5, 10, and 20 cm/second. Positive values are necessary for blood to be visible. As the ramp pulse gets steeper, the distal portion of the slab performs better; however, the proximal portion performs worse. With decreasing speed, the contrast values decrease, and the ramp pulse changes have more pronounced effects. With GM as background, the contrast values are always higher owing to the longer T_1. However, with WM as background, the gains with a steeper ramp pulse in the
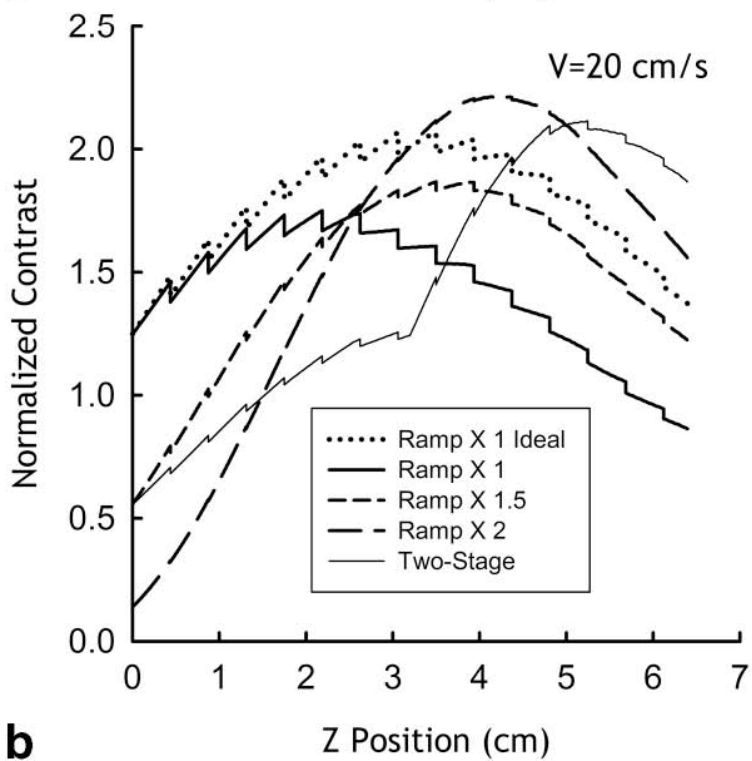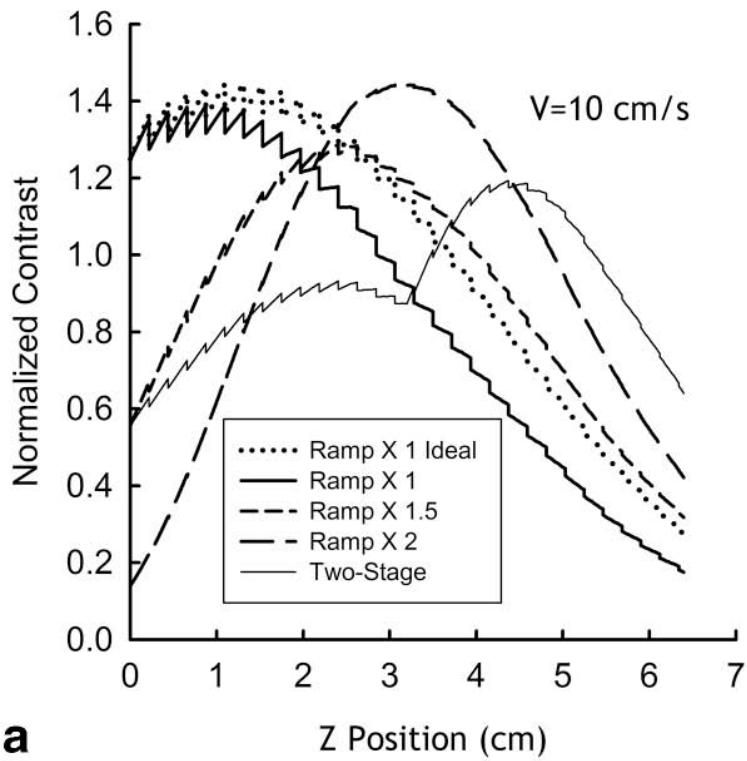
Figure 4-3: Theoretical results showing the effect of ramp pulse variation on blood-to-GM contrast along the inferior–superior direction for the diagonal artery. **a:** Bloodvelocity (V) = 10 cm/second. **b:** V = 20 cm/second.

134

distal region are larger and become more important for vessel visibility. At the

slower velocity of 5 cm/second, the standard ramp loses visibility even before the

middle of the imaging slab.

Table 4-1: Dependence of Normalized Blood-to-White Matter Contrast on Ramp
Shape

Speed (cm/s)	Slice position [a] (mm)	Normal Ramp	1.5 x Ramp	2 x Ramp	2-Stage Ramp
5	5	0.68	0.42	0.20	0.37
	35	-0.09	0.06	0.23	0.14
	40	-0.15	-0.03	0.10	0.14
	60	-0.30	-0.28	-0.27	-0.19
10	5	0.81	0.47	0.21	0.41
	35	0.36	0.57	0.78	0.52
	40	0.27	0.48	0.69	0.60
	60	-0.09	0.02	0.11	0.28
20	5	0.88	0.50	0.22	0.44
	35	0.91	1.09	1.27	0.87
	40	0.84	1.08	1.31	1.06
	60	0.43	0.68	0.93	1.10

[a] Slice position 1 refers to the most inferior slice.

Figure 4-4 shows the average experimental results from the detailed ROI

analysis of six blood vessels. Theoretical curves are also plotted using the

diagonal vessel with increased speed values of 40 cm/second for the inferior half

of the imaging slab (16) and 20 cm/second for the superior half. These higher

blood velocities are more realistic for the young healthy volunteers considered in

this study (17). The graph illustrates the contrast from steeper ramps relative to

the contrast from the standard ramp, with the standard ramp represented by a flat line at 1.0. The simulation and experimental results are in good agreement. Despite the overlapping of SD error bars, in the entire superior half of the slab, and for every individual case, the ramp1.5 CNR values were always higher than the corresponding standard ramp values and lower than ramp2 values. Table 4-2 illustrates the absolute experimental CNR values where the effects of increasing ramp slope are in agreement with theoretical trends.

Figures 4-5 and 4-6 show examples of maximum intensity projection (MIP) images, which illustrate the effects of varying ramp slope. The enhancement of blood vessel visibility in the distal area is noted for increasing ramp steepness, with a corresponding loss of visibility for proximal regions with increasing steepness. In Fig. 4-5, ramp1.5 offers the best compromise of the pulse shapes tested because it maintains proximal high signal, while adding distal vessel visibility improvement. Figure 4-6 shows a second experimental comparison between "no ramp," Ramp1, and Ramp2 pulse shapes. The arrows indicate improved image contrast with increasing ramp slope, particularly for vessels with a somewhat diagonal and sideways trajectory, which suffer from increased RF field fall-off along the path. Figure 4-6 also illustrates the effect on venous flow, with increasingly poor depiction of the superior sagittal sinus as the ramp slope is increased. The opposing direction of flow in the vein leads to an inverted ramp pulse for venous blood, which causes more rapid saturation. For all ramp pulses, when the assumption of flow direction is incorrect, the ramp can have a detrimental effect.

136
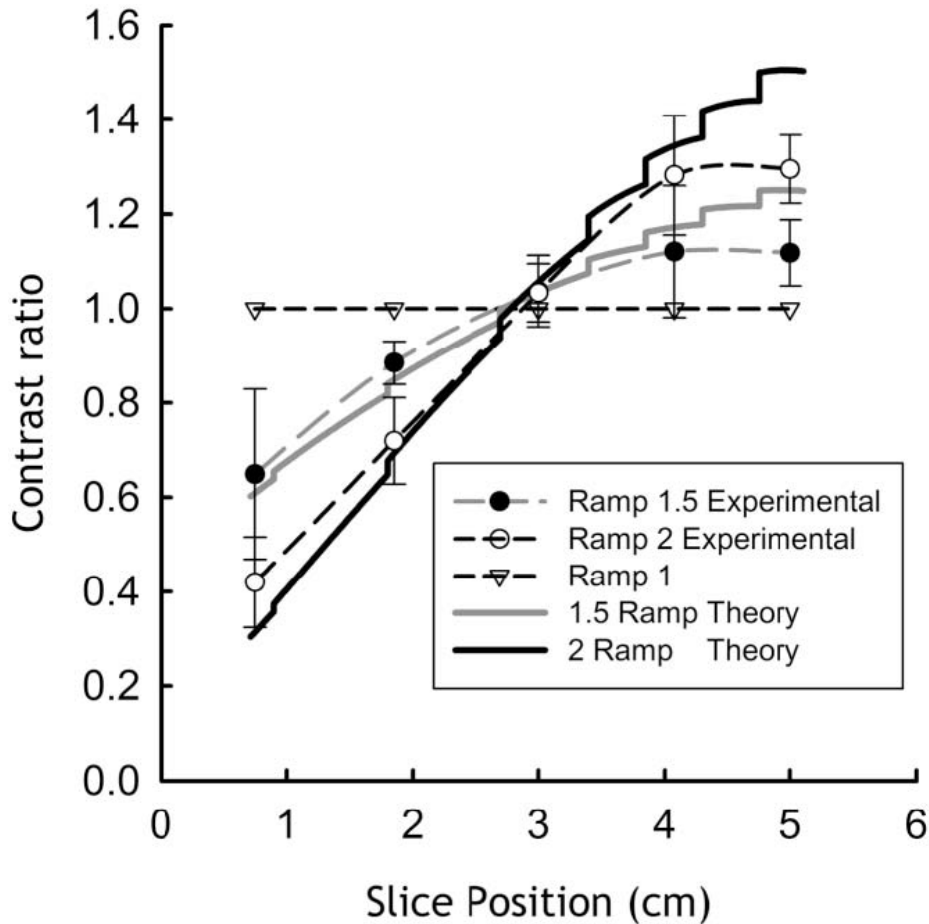
Figure 4-4: Graph illustrating experimental and theoretical results for blood-to-background contrast. The theoretical curves (solid) are shown with the experimental points joined by dashed best-fit lines. The y-axis plots the fractional change in contrast from the original ramp pulse (new ramp contrast / original ramp contrast). This measurement accounts for variations in background tissue signal. The experimental points are shown with SD error bars arising from averaging six different vessels. The theoretical results, shown in solid lines, arise from the diagonal vessel with a blood speed of 40 cm/ second for the first half of the slab, and 20 cm/second in the second half. The simulation curves shown are GM based.

Table 4-2: Average Experimental CNR Values for Different Ramp Slopes

Slice position * mm	Normal Ramp	1.5 x Ramp	2 x Ramp
7	94.3 $\pm$ 31.4	72.9 $\pm$ 23.7	45.7 $\pm$ 14.6
19	82.3 $\pm$ 12.9	73.1 $\pm$ 12.9	58.9 $\pm$ 10.0
30	72.0 $\pm$ 26.6	73.1 $\pm$ 25.7	73.4 $\pm$ 25.7
40	44.0 $\pm$ 19.7	48.6 $\pm$ 20.6	56.9 $\pm$ 24.0
51	39.7 $\pm$ 10.9	44.3 $\pm$ 12.0	51.4 $\pm$ 13.1

[a] The slice position shown is the middle slice position for the 3D-ROI(s) studied. Slice position 1 refers to the most inferior slice.

4.4 Discussion

Ramp pulses were first introduced to carefully control the RF field distribution in order to achieve better blood CNR. We have illustrated that the RF interference effect present at higher fields is detrimental to this careful control of RF field distribution. However, if the direction of a blood vessel is known, one can evaluate the interference effect to determine a better ramp shape. We used this approach to improve the visibility of the distal middle and posterior cerebral arteries by simply varying the ramp slope.

In Fig. 4-2, for the diagonal artery, the effective shape resulting from the ramp1.5 pulse most closely resembles the initial standard ramp profile without considering RF inhomogeneity. Thus, it is not surprising that ramp1.5 is the best compromise of the linear ramp choices considered. This is evident from simulation and quantitative experimental results, and qualitative inspection. When compared with the standard ramp shape, it shows higher contrast levels in the upper two-thirds of the slab, as evident in Fig. 4-3, and 15% higher experimental

values in the superior half of the imaging slab, as shown in Fig. 4-4. The reduced

contrast in the lower third is a reasonable compromise, since the thicker vessels in

this area still have more than adequate CNR even though the background levels

are higher. The ramp2 case shows more gain in the distal area, but the sacrificed

contrast may reduce visibility of proximal blood vessels.

Theoretical results from the 2-stage ramp are shown in Fig. 4-3.

It combines the benefits of standard ramp and ramp2 because it fits the general

profile of the former in the inferior half of the slab and the latter in the superior

portion. This gives rise to contrast levels in the superior portion of the slab that

outperform all of the linear ramps, with more significant enhancement at lower

blood speeds. The theoretical results of a 2-stage ramp show that one can achieve

enhancement ratios higher than 30% while still having reasonable CNR levels in

the inferior half of the slab. Clearly, more complex forms of ramp pulses are

possible, and indeed have been designed for lower fields (18,19). For the purpose

of this work, a simple experimental solution was used to illustrate the importance

of the RF focusing problem at higher fields.

The RF interference effect is typically not visually evident in a TOF

source image at 3.0 T. Even though the RF field is substantially reduced in the

periphery, the reduced flip angle can lead to higher background magnetization due

to less saturation. When the same circumscribing RF coil is used for reception,

this increased background magnetization in peripheral regions is offset by the

reduced reception profile associated with the same regions, leading to a relatively

flat background signal (20). Similarly, when local reception coils are used, the

peripheral regions may appear much more intense in the image, even though the transmit profile was significantly reduced. Nevertheless, the distal blood signal does suffer from the reduced transmit RF field, and blood-to-background contrast is significantly compromised, even though we do not see the effect on background signal alone.
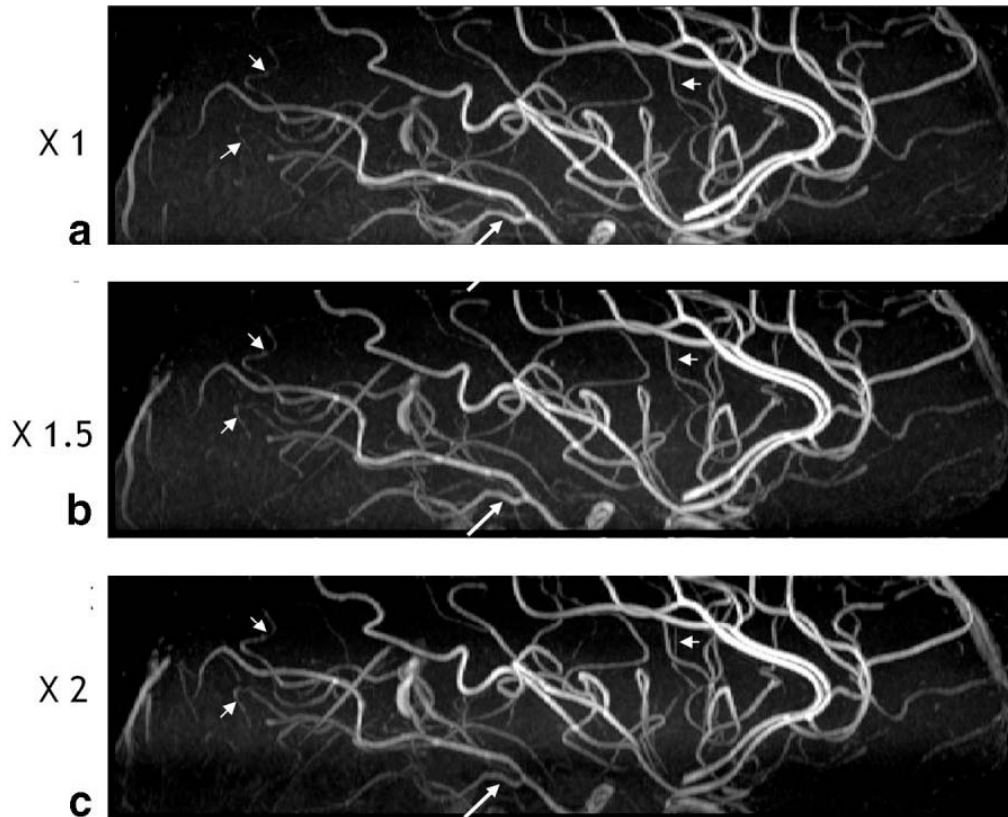
Figure 4-5: Sagittal MIP images of the right half of the brain are shown for comparison of the (**a**) original, (**b**) ramp1.5, and (**c**) ramp2 pulses. The three short arrows point to distal vessels with enhanced visualization as the ramp pulse gets steeper. The longer arrows show a proximal vessel in which visualization is reduced as the ramp pulse gets steeper. The ramp1.5 in b offers a compromise, and provides high visualization across the slab.
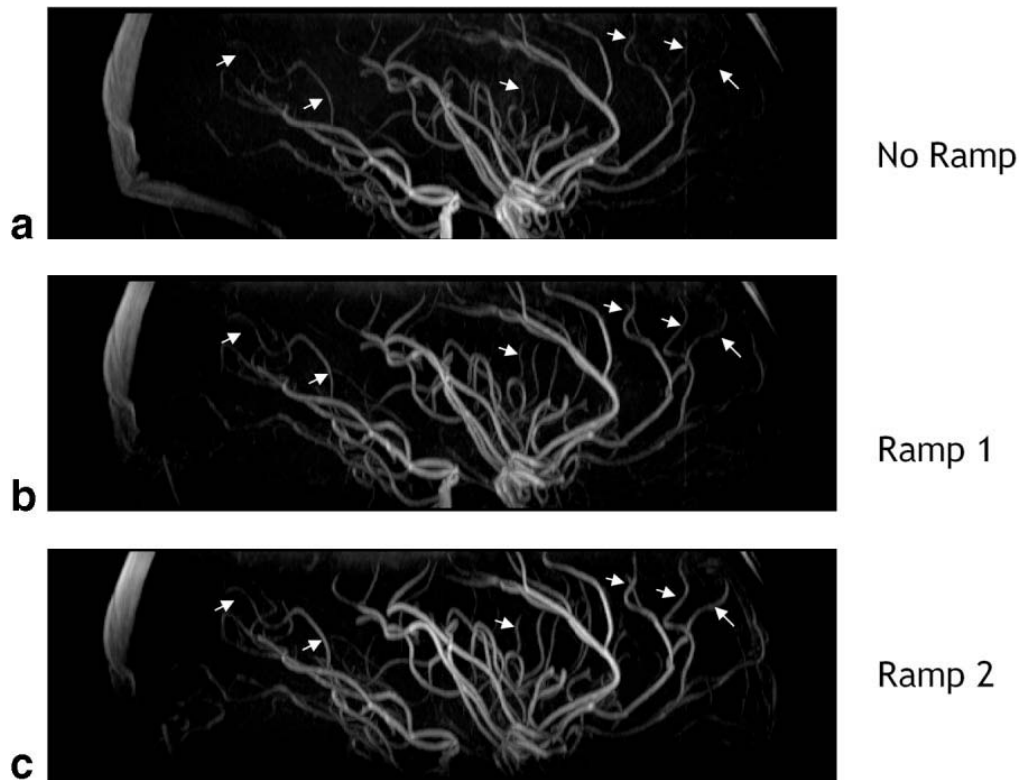
Figure 4-6: Sagittal MIP images of the brain are shown for comparison of (**a**) square, (**b**) standard ramp, and (**c**) ramp2 pulses. The left three arrows point to distal and lateral vessels with enhanced visualization as the ramp pulse gets steeper. The right three arrows show vessels with a medial trajectory. Without venous suppression, the superior sagittal sinus is also visible, which illustrates the detrimental effect of increasing ramp slope on venous flow.

The pathway of a typical middle or posterior cerebral artery leads to the RF interference effect playing a large role in altering the flip angle along the vessel path. For example, a central vessel proceeding only superiorly would not be nearly as affected as one proceeding superiorly and laterally. In this work, a diagonal vessel was used to approximate a middle cerebral artery. However, an artery that has a more direct path through the slab will receive a steeper RF ramp. Although this may not be an ideal RF profile, the fact that the artery is traveling through the slab with a shorter pathway means that blood must spend less time in

141

the slab than in other vessels with different geometry, assuming similar blood velocities. This faster passage through the imaging slab will yield reduced blood saturation. Distal middle and posterior cerebral arteries have both a longer path and less-suitable geometry for the high-field RF distribution. Therefore, tailoring a pulse shape to these arteries is expected to enhance their visibility without substantially harming the visibility of arteries with a more direct path. Nevertheless, like all ramp pulses, there is an inherent assumption about the directional dependence of blood flow. When the vessel flows counter to the ramp pulse slope, the value of the pulse is negated.

For simplicity, the diagonal vessel used in the simulation was assumed to have uniform thickness, which is not the case in reality. In Fig. 4-4, the most distal experimental point is significantly lower than the theoretical expectation. This can be attributed to the low SNR and small size of blood vessels in this region, which causes more pronounced partial-volume effects and makes it more difficult to measure the ROIs. This leads to a variation of experimental CNR values from those predicted by simulation. Also, blood speed decreases in the distal vessel segments. The above reasons show the need for more effective background suppression to make smaller blood vessels visible.

The stepped appearance of most plots of Fig. 4-3 is due to the application of the ramped RF excitation every TR in a quantized manner, and the use of a single average blood velocity. As blood traverses the volume, it can be considered as a moving segment with length equal to the product of TR and blood velocity. Since a ramp RF pulse is applied every TR, the moving segment experiences a

flip angle at its leading edge that is slightly larger than the flip angle it experiences at its tail. Thus the leading edge becomes saturated faster than the trailing edge, which changes the previously positive slope of this segment to a negative slope over time. However, this stepped appearance is not visible experimentally due to an averaging effect that smooths out the quantization process. Specifically, the blood velocity varies with vessel size, with position across the vessel diameter, and with time along the cardiac cycle, which leads to an averaging of the resulting blood signal.

The subjects of this study were healthy young volunteers with higher blood speeds than are found in most typical patient populations. This higher speed leads to highly visible vessels even when a flat ramp pulse is applied. Although the benefits of increasing the ramp pulse slope to overcome RF interference have been demonstrated in this group, the relative benefits are expected to be greater in cases of slower blood speeds, as suggested by the simulation results shown in Fig. 4-3. Although the simulations provide theoretical evidence, further investigation in a patient population is necessary.

In conclusion, the effect of RF destructive interference at 3.0 T on ramp pulses has been illustrated both theoretically and experimentally for imaging the intracranial arteries. For blood vessels flowing superiorly and to the periphery, simply changing the linear ramp slope can help counter the losses from RF interference. As verified in both simulations and normal volunteer experiments, altering the ramped excitation to 1.5 times its typical slope led to improved depiction of both the middle and posterior cerebral arteries.

4.5 References

1. Bernstein MA, Huston III J, Lin C, Gibbs GF, Felmlee JP. High-resolution intracranial and cervical MRA at 3.0 T: technical considerations and initial experience. Magn Reson Med 2001;46:955–962.

2. Al-Kwifi O, Emery DJ, Wilman AH. Vessel contrast at three tesla in time-of-flight magnetic resonance angiography of the intracranial and carotid arteries. Magn Reson Imaging 2002;20:181–187.

3. Alecci M, Collins CM, Smith MB, Jezzard P. Radio frequency magnetic field mapping of a 3 Tesla birdcage coil: experimental and theoretical dependence on sample properties. Magn Reson Med 2001;46:379–385.

4. Van de Moortele PF, Akgun C, Adriany G, et al. B-1 destructive interferences and spatial phase patterns at 7 T with a head transceiver array coil. Magn Reson Med 2005;54:1503–1518.

5. Roschmann P. Radiofrequency penetration and absorption in the human body: limitations to high-field whole-body nuclear magnetic resonance imaging. Med Phys 1987;14:922–931.

6. Jin JM, Chen J, Chew WC, Gan H, Magin RL, Dimbylow PJ. Computation of electromagnetic fields for high-frequency magnetic resonance imaging applications. Phys Med Biol 1996;41:2719–2738.

7. Bottomley PA, Andrews ER. RF magnetic-field penetration, phase shift and power dissipation in biological tissue—implications for NMR imaging. Phys Med Biol 1978;23:630–643.

8. Nagele T, Klose U, Grodd W, Petersen D, Tintera J. The effects of linearly

increasing flip angles on 3D inflow MR-angiography. Magn Reson Med 1994;31:561–566.

9. Goodrich KC, Blatter DD, Parker DL, Du YPP, Meyer KJ, Bernstein MA. A quantitative study of ramped radio frequency, magnetization transfer, and slab thickness in three-dimensional time-of-flight magnetic resonance angiography in a patient population. Invest Radiol 1996;31:323–332.

10. Atkinson D, BrantZawadzki M, Gillan G, Purdy D, Laub G. Improved MR-Angiography—magnetization-transfer suppression with variable flip angle excitation and increased resolution. Radiology 1994;190: 890–894.

11. Collins CM, Li SZ, Smith MB. SAR and B-1 field distributions in a heterogeneous human head model within a birdcage coil. Magn Reson Med 1998;40:847–856.

12. Simunic D, Wach P, Renhart W, Stollberger R. Spatial distribution of high-frequency electromagnetic energy in human head during MRI: numerical results and measurements. IEEE Trans Biomed Eng 1996;43:88–94.

13. Vaughan JT, Garwood M, Collins CM, et al. 7T vs. 4T: RF power, homogeneity, and signal-to-noise comparison in head images. Magn Reson Med 2001;46:24–30.

14. Collins CM, Smith MB. Signal-to-noise ratio and absorbed power as functions of main magnetic field strength, and definition of "90 degrees" RF pulse for the head in the birdcage coil. Magn Reson Med 2001;45:684–691.

15. Wansapura JP, Holland SK, Dunn RS, Ball Jr WS. NMR relaxation times in the human brain at 3.0 Tesla. J Magn Reson Imaging 1999;9:531–538.

16. Moore DF, Altarescu G, Ling GSF, et al. Elevated cerebral blood flow velocities in Fabry disease with reversal after enzyme replacement. Stroke 2002;33:525–531.

17. Ringelstein EB, Kahlscheuer B, Niggemeyer E, Otis SM. Transcranial Doppler sonography—anatomical landmarks and normal velocity values. Ultrasound Med Biol 1990;16:745–761.

18. Priatna A, Paschal CB. Variable-angle uniform signal excitation (VUSE) for 3-dimensional time-of-flight MR-angiography. J Magn Reson Imaging 1995;5:421–427.

19. Nagele T, Klose U, Grodd W, Nusslin F, Voigt K. Nonlinear excitation profiles for 3-dimensional inflow MR-angiography. J Magn Reson Imaging 1995;5:416–420.

20. Wang D, Heberlein K, LaConte S, Hu XP. Inherent insensitivity to RF inhomogeneity in FLASH imaging. Magn Reson Med 2004;52: 927–931.

Chapter 5

Simultaneous and Time Efficient Arterial and Venous Time of Flight MRA with Reduced Spatial Saturation

5.1 Introduction

Comprehensive imaging of both the arterial and venous vascular system is a useful diagnostic tool. However, without contrast agent, exclusive imaging of both arteries (A) and veins (V) is a time consuming process since two distinct acquisitions, one suppressing arteries and one suppressing veins through the application of spatial saturation pulses are required (1). Alternative approaches to AV separation include exploiting first-pass dynamics in contrast enhancement (2) or using susceptibility-induced phase for AV distinction (3,4). Limitations of the susceptibility approach include a long echo time at low field in order to achieve venous phase evolution, hence leading to poor signal to noise ratio (SNR) in the venous image. Moreover, susceptibility weighted imaging (SWI) is not affected by flow rates or patterns within the veins, which can be both an advantage and a disadvantage. For contrast agent methods, their limitations include added cost, rapid contrast dynamics and safety concerns (5,6).

In this work, we return to the use of saturation pulses for preferential vessel saturation, but demonstrate that the time overhead of a second full scan can be minimized along with the associated extra SAR resulting from the utilization of RF saturation. The common practice in TOF MRA is to apply the shortest

possible echo time which typically requires a high bandwidth RF pulse. The need to minimize RF pulse time, increases SAR/power deposition in the sample. The higher the static magnetic field the more significant the RF power concern. With the addition of venous saturation pulse, this problem can be further exacerbated as the spatial saturation pulse includes the application of an additional 90° RF pulse.

To reduce the application of spatial saturation, we will make use of the fact that the central imaging views make up most of the image contrast. This well-known fact has been exploited in many MRI methods including contrast-enhanced MR Angiography (MRA) (7), magnetization transfer MRA (8,9) and dynamic MRI (10). In our case, we will acquire a portion of the central k-space data with different saturation pulses. We will make use of the preferential value of central k-space views in determining image contrast, and the fact that outer k-space views acquired without spatial saturation can be used for both arterial and venous imaging.

The method introduced in this work is similar to the above methods in the approach of augmenting the middle of k-space information by data from the same imaging volume that has changed contrast. At first, applications of the Keyhole method used the high frequency portion of k-space from a full image acquisition applied prior to contrast injection (11). This approach had a limitation of utilizing low resolution data to present the newly introduced contrast, leading to undefined borders and "spatial blur of enhancement" also known as "signal bleeding". Bishop, et al., offered an approach to overcome the above limitations (12) by introducing contrast from a fully acquired contrast enhanced image. The method

proposed in this work is specifically designed to be immune to such limitations where it intrinsically holds full k-space information from a non-saturated scan. This includes contrast as well as border information for both arteries and veins. In other words, the proposed method applies selective contrast subtraction at the centre of k-space rather than partially introducing the desired contrast to the centre of k-space.
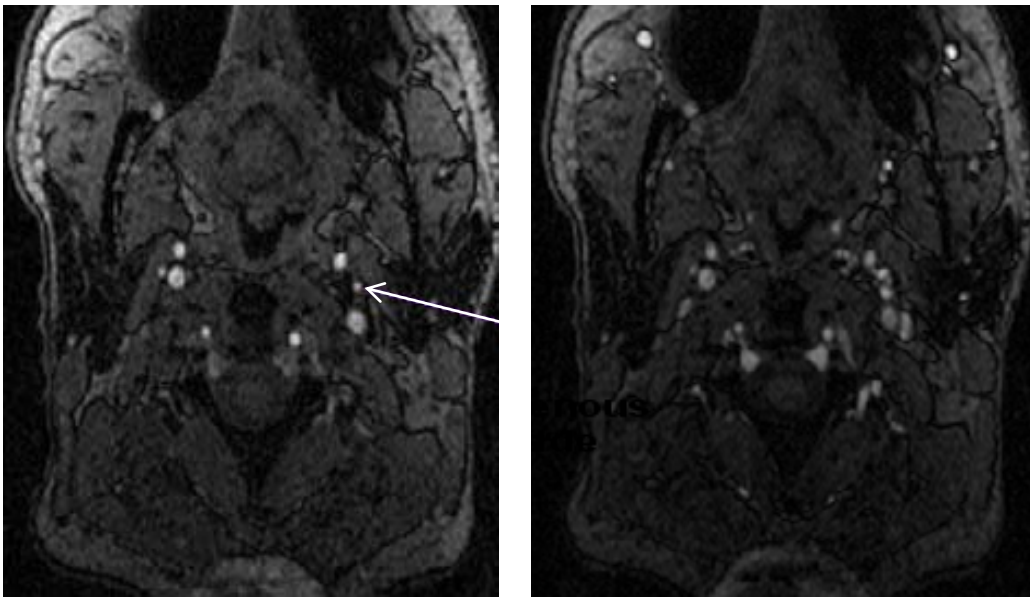
Figure 5-1: Arrow showing an artery that is visible only in the venous saturated case (left) while on the right side image, it is overwhelmed by the two neighboring veins.

5.2 Methods

### 5.2.1 Theory

Three-dimensional time-of-flight (3D TOF) images from both arteries and veins are developed in two separate sets of images using minimal scan time and minimal power deposition. A complete unsaturated scan containing all the information and contrast for both veins and arteries is collected. As most of the contrast in an image resides in the central k-space, a second scan with venous saturation applied can be obtained of only this small fraction of the centre of k-space in the phase encoding plane. The second data set contains only the non-saturated vessels (i.e. arteries). By subtracting or replacing the no saturation (no-sat) acquisition using partial k-space information from the venous saturation (V-sat) acquisition, the contrast pertaining to the veins from the main scan can be removed. This enables quicker scans with less RF power deposition. This enables significant reduction in scan time as well as less RF power deposition, which is an important factor for high magnetic field strengths.

5.2.2 Experimental Methods

In order to validate the proposed imaging technique and to determine the acceptable degrees of scan reduction, two scans were acquired on each of five normal volunteers. For the purpose of validation, a complete venous saturated scan was collected. Venous saturation was applied to one scan and no saturation to the other. The experiments were performed on a 1.5T Siemens Sonata magnet using a 3D-TOF sequence with 62.5% partial Fourier read-out, flow compensation on read-out and slice selection, 25° excitation flip angle,

150

FOV= 20x16.3x3.2 cm, acquisition matrix = 512x208x32, 1 mm slices, SW=82.6

kHz TR/TE 36/6.9 ms. Four consecutive slabs were acquired, with 25-50%

overlap between every two consecutive slabs.
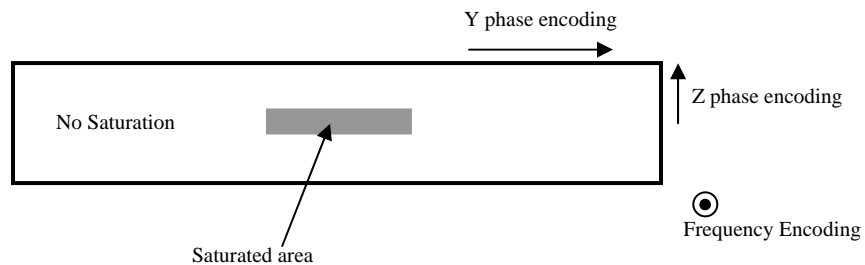
Figure 5-2: Schematic showing a section of k-space perpendicular to the frequency encoding direction (coronal view) with the gray shaded area showing the area imported from a partially venous-saturated scan. 5% segment at each edge of the shaded area were modulated by a hanning window with fall off towards the outside of the shaded area for saturated data and the reverse of the same modulation for the unsaturated data.
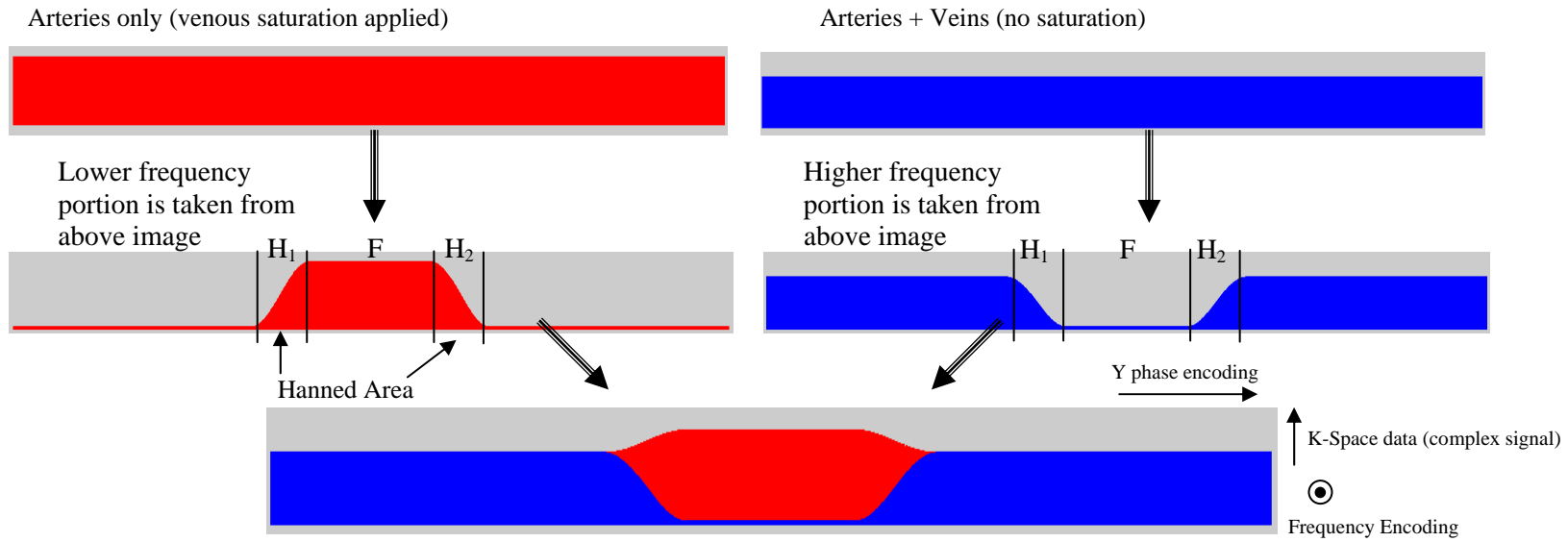
Figure 5-3: Example of merging two phase encoding data vectors. Schematic showing the process to merge the two images with different contrast and intensity using a mask applied to the Y phase encoding direction. The two hanned portions of the mask are marked (H$_1$) and (H$_2$) while the flat area of the mask is marked (F).

At first, filtering was applied to the Y phase encoding direction alone as demonstrated in figure 5-3, while the Z direction was completely utilized. To avoid sudden transition in the augmenting process, a hanning filter was applied where the data from the two scans would meet. The inverse of the same mask (*1-mask*) was applied to the (AV) data. The ratio of "hanned part" to flat part of the mask was varied while keeping the total width of the mask constant. The resulting images were assessed for any artifacts or other changes. As no such adverse results were noticed at all, the hanned ratio was set to 5% for the remaining work ($F/[\,H_1 + F + H_2\,] = 95\%$). The total mask width was also varied and resulting images were inspected to ensure that the process was qualitatively successful in removing venous contrast without any distortion to the images.

The next phase was to also vary the Z coverage. Every two corresponding k-space data sets were then combined as shown in figure 5-4, where different percentages from both phase encoding directions were incorporated into the unsaturated image. The resulting images were evaluated with ROI's for each vessel in the original unsaturated image.

The incorporation process was done in steps as follows (as fraction of the full (A) k-space matrix covered):

$PE_{1/Y}$ 5,10, …. , 100 %

$PE_{2/Z}$ 1/16,2/16, …., 16/16

All possible combinations of the above fractions were applied and all resulting images were analyzed. In these images, ROI's were placed on arteries, veins and adjacent background, as shown in Figure 5-5, and each ROI was

assessed for each of the above 320 PE variations. The results were determined for both a global average as well as selected veins of different sizes. All veins ROI's were measured for all 320 cases and compared to the unsaturated venous intensity for each vein.
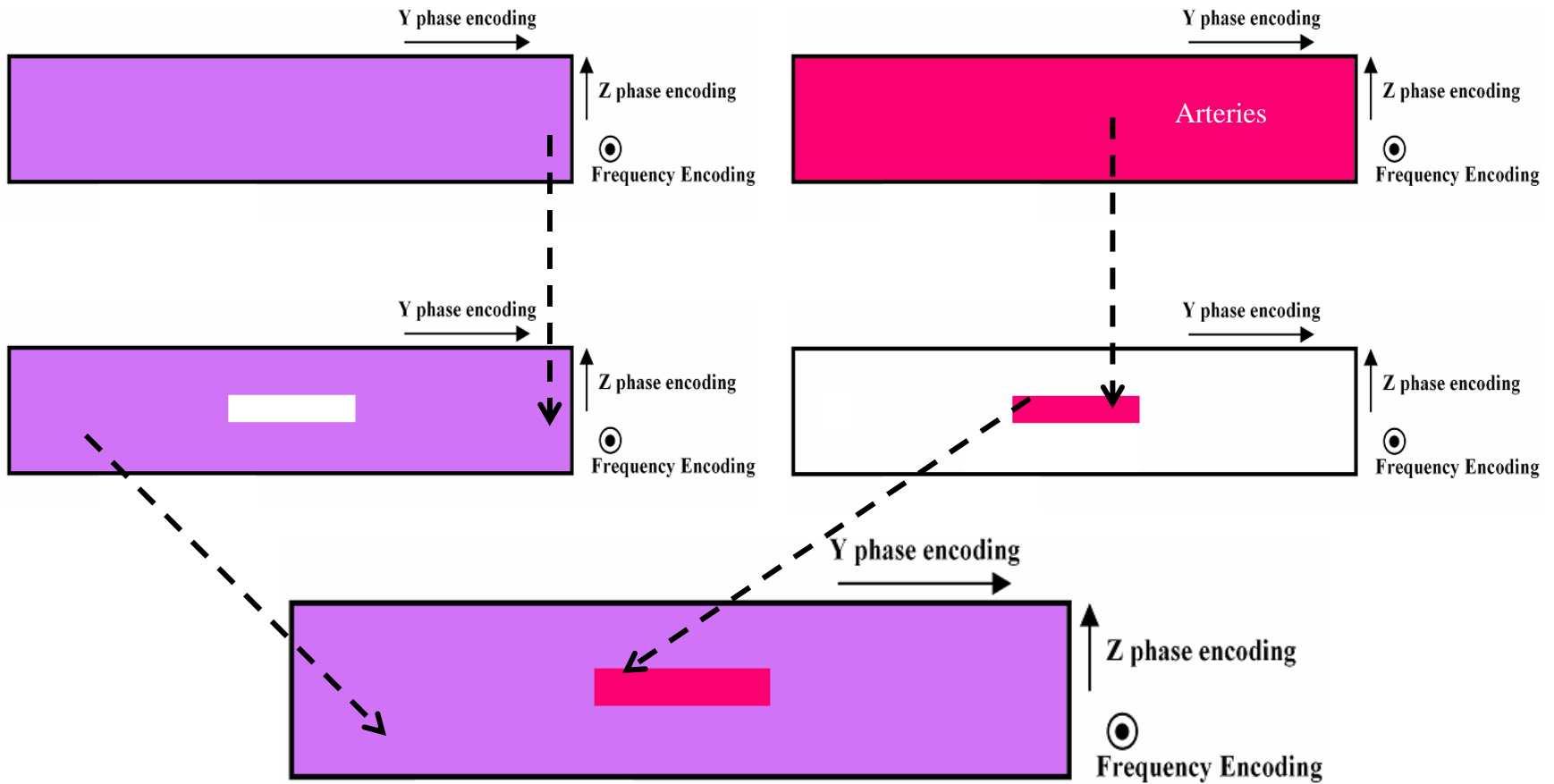
Figure 5-4: Schematic showing a section of k-space perpendicular to the frequency encoding direction with the red area showing the partial area imported from a venous saturated (A) scan.
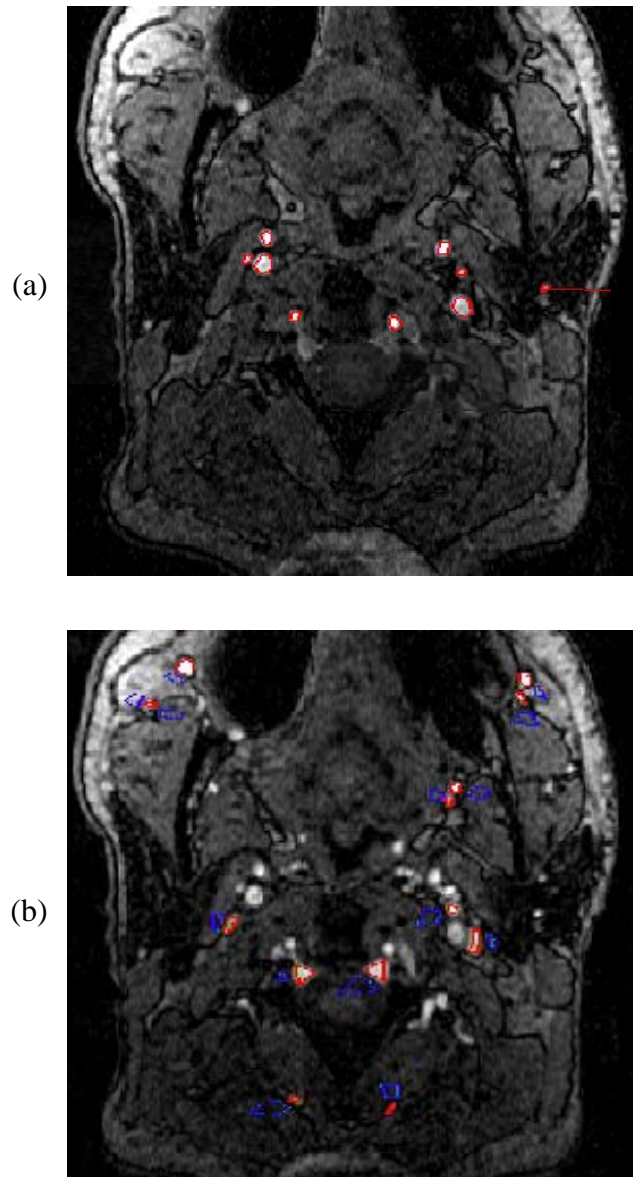
Figure 5-5: ROI examples from the analysis process. **(a)** Shows ROI placement on arteries from the venous saturated version of the same image in *(b)*. (b) Shows ROI placement on veins in a non-saturated image (Red) as well as background ROI selection in background areas close to the corresponding venous ROI's (Blue).

5.3 Results

Figure 5-6 shows images with varying degrees of saturation. The saturated k-space ratio of 25% led to all veins being suppressed down to the same level as the 100% saturated case while the 13% saturated k-space ratio led to some of the smaller veins being slightly above that level while still dim enough to be closer to the background intensity than the actual arterial intensity.

The proposed new method can be used to get separate venous images either by processing the images shown readily or by running another partial scan with arterial saturation.

It is observed by the red data element in the surface plot in figure 5-7, at *25% PE1 x 31.25% PE2*, that 82% venous suppression was achieved. This translates to only 8% scan time overhead for the venous saturation portion of the combined scan. This can reduce total scan time by as much as 46% while SAR due to spatial saturation could be reduced by as much as 92% in one scan.
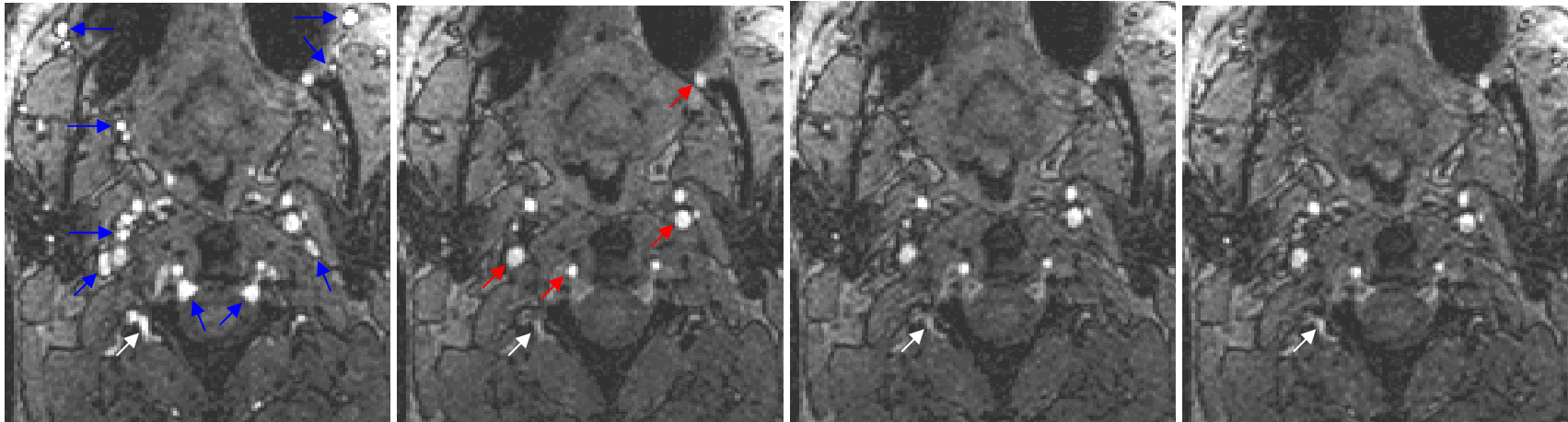
The plots in figure 5-8 show that less saturated K-space is needed to suppress a larger vein. It also shows that further increasing Y saturation is more effective than increasing Z saturation.

No Venous Saturation	100% PE1 x 100% PE2	50% PE1 x 50% PE2	35% PE1 x 37.5% PE2

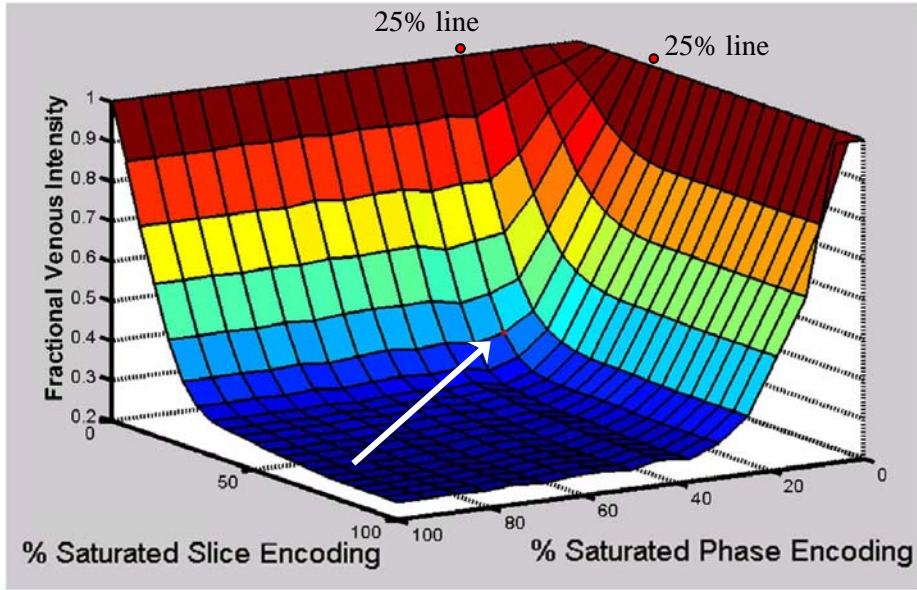(Veins Saturated)	(Veins Saturated)	(Veins Saturated)

Figure 5-6 : Neck source images showing different saturation extents. Blue arrows on the left point to veins while red arrows show arteries in the second image. The image at far right illustrates that only ~1/3rd of k-space in each phase encode dimension was necessary to achieve venous suppression requiring only 13% additional scan time. White arrows show a vein which is slightly more visible on the far right image yet still much less intense than the arteries in the same image and than its unsaturated level.

Table 5-1: Response of venous signal levels to different saturation extents.

Saturation ratio PE1 x PE2	Fractional scan time overhead	Average of all Vein results (% of max. intensity)	*% saturation (compared to full saturation case)*	Large Vein (5 mm diameter) (% of max. intensity)	*% saturation (compared to full saturation case)*
35% x 37.5%	13%	39%	82%	28%	95%
50% x 50%	25%	30%	95%	27%	96%
Full saturation	100%	26%	100%	24%	100%

Figure 5-7: Experimental results showing data processed with different degrees of saturation. A surface plot shows the average intensity from all veins illustrating progressive venous saturation. The white arrow points at 25% PE1 x 31.25% PE2, which achieves 82% venous suppression. This translates to only 8% scan time for the venous saturation portion of the combined scan.
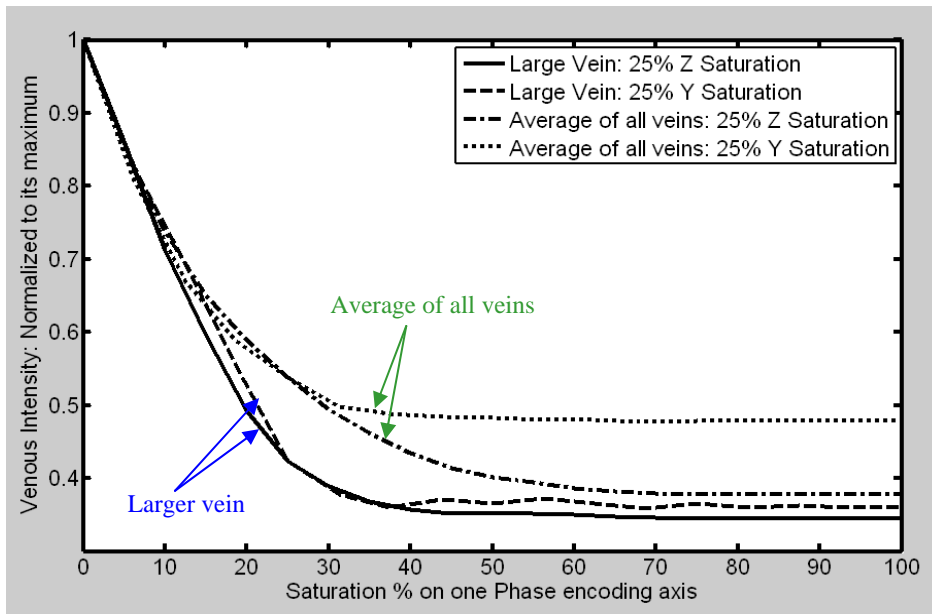

Figure 5-8: A graph differentiating between the average case and the case of larger veins. Venous intensity is illustrated for various degrees of saturation, and for all veins or a single large vein.

160

5.4 Discussion

Twenty-five percent saturation (ie: 50% in each phase encode direction) led to all veins being suppressed down to the "fully saturated" level while the 13% case led to some of the smaller veins being suppressed to slightly above the "fully saturated" level.

We demonstrated that less saturated K-space is needed to suppress a larger vein. Increasing Y saturation was more effective than increasing Z saturation (slice select direction) because the jugular veins in the neck traverse the imaging slab in a somewhat vertical manner (along the Z direction) which leads to a very narrow k-space in the Z-direction. Clearly, the volume choice and the matrix parameters will determine the k-space and the appropriate sampling. In regard to imaging volume, the preferential direction of the blood vessels of interest, should play a role in the selection of which central k-space views to use. For example a coronal plane for imaging the neck arteries and veins would lead to a cross sectional phase encode plane which would merit more isotropic sampling, since the objects of interest are essentially circular in that plane. However, in the axial plane of 3D acquisition, the blood vessels have a much longer profile in the z –direction.
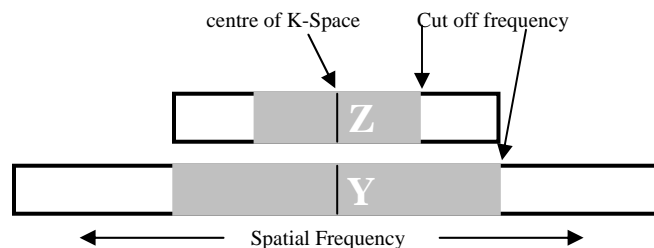
Figure 5-9: showing a typical case where $\Delta Y \sim \Delta Z/2$ and hence the spatial frequency of Ky_{max} is approximately double of Kz_{max}. The grey area represents 50% filtering/saturation in both phase encoding directions where in the Y direction the cut off frequency is consequently double that in the Z direction.

161

As well as object shape, the matrix resolution also plays a critical role in the extent of k-space. For example, assuming a typical situation where $\Delta Y \sim \Delta Z/2$, (eg: 1.5 mm slices with 200 FOV and 256 matrix), Ky_{max} will be roughly double of Kz_{max} as in figure 5-9. The figure also shows in gray shading a 50% filtering of both directions. In this case, weighting the choice of central views by distance to the k-space origin in the phase encoding plane, as has been done previously (13), would be preferred. However, when object shapes are known to be anisotropic in the phase encoding plane, isotropic may not necessarily be ideal (14).

In conclusion, we have introduced a method to allow artery and vein imaging with substantially reduced acquisition times and with minimal use of venous spatial saturation. The method is based on acquiring a full scan with no saturation, and a vastly reduced scan with partial saturation. We demonstrated that with only an extra 13% of scan time, it was possible to obtain separate arterial and venous images of the neck. Total scan time was reduced by as much as 46% over a two scan approach and SAR due to spatial saturation was reduced by as much as 92% over the two scan approach. Recently seven Tesla TOF MRA results for the human brain have tended not to use spatial saturation (15), owing to the high RF heating at this field strength that is ~25 times more than 1.5 T. Our method could also enable high field use of RF venous saturation by using central k-space selective venous saturation in the manner that magnetization transfer saturation was previously used by Parker (8) and Thomas (9). Thus, as well as applying to combined artery and vein imaging, our method may also be used for artery only imaging with far reduced RF power.

5.5 References

1- Felmlee JP, Ehman RL. Spatial presaturation: a method for suppressing flow artifacts and improving depiction of vascular anatomy in MR imaging. Radiology 1987:164:559-565.

2- Al-Kwifi O, Shelef I, Farb RI, et al. High-resolution imaging of the intracranial arterial and venous systems following a single contrast injection. JMRI 2006: 24 (2):267-273

3- Wang Y, Yu Y, Li D, Bae KT, Brown JJ, Lin W and Haacke EM. Artery and Vein Separation Using Susceptibility-Dependent Phase in Contrast-Enhanced MRA. JMRI 2000; 12:661–670.

4- Du YP, Jin Z. Simultaneous acquisition of MR angiography and venography (MRAV). Magn Reson Med 2008; 59:954–958.

5- Grobner T. Gadolinium: a specific trigger for the development of nephrogenic fibrosing dermopathy and nephrogenic systemic fibrosis? Nephrol Dial Transplant 2006; 21:1104–1108.

6- Martin DR, et al. Decreased Incidence of NSF in Patients on Dialysis After Changing Gadolinium Contrast-Enhanced MRI Protocols. JMRI 2010; 31:440–446 (2010)

7- Maki JH, Prince MR, Londy FJ, Chenevert TL. The effects of time varying intravascular signal intensity and k-space acquisition order on three-dimensional MR angiography image quality. JMRI 1996; 6(4); 642-651.

8- Parker DL, Buswell HR, Craig K, Alexander AL, Keck N, Tsuruda JS. The application of magnetization transfer to MR angiography with reduced total power. Magn Reson Med 1995;34:283–286.

9- Thomas,SD, Al-Kwifi O, Emery DJ, Wilman AH. Application of Magnetization Transfer at 3.0 T in Three-Dimensional Time-of-Flight Magnetic Resonance Angiography of the Intracranial Arteries. JMRI 2002; 15:479-483.

10- van Vaals JJ, Brummer ME, Dixon WT, et al. "Keyhole" method for accelerating imaging of contrast agent uptake. JMRI 1993; 3:671-675.

11- Chenevert TL, Helvie MA, Aisen AM, et al. Dynamic three-dimensional imaging with partial k-space sampling: Initial application for Gadolinium-enhanced rate characterization of breast lesions. Radiology 1995; 196 (1):135-142.

12- Bishop JE, Santyr GE, Kelcz F, et al. Limitations of the keyhole technique for quantitative dynamic contrast-enhanced breast MRI. JMRI 1997; 7(4):716-723.

13- Wilman AH, Yep TCH, Al-Kwifi O. Quantitative evaluation of nonrepetitive phase-encoding orders for first-pass, 3D contrast-enhanced MR angiography. Magn Reson Med 2001; 46(3):541-547.

14- Wilman AH, Riederer SJ. Improved centric phase encoding orders for three-dimensional magnetization-prepared MR angiography. Magn Reson Med 1996; 36(3): 384-392.

15- Monninghoff C, Maderwald S, Theysohn JM, et al. Evaluation of Intracranial Aneurysms with 7T versus 1.5T Time-of-Flight MR Angiography - Initial Experience. RöFo [1438-9029] 2009; 181(1):16-23.

Chapter 6

Conclusions

The work carried out in this thesis was focused on solving some of the limitations facing two gradient echo imaging methods, Time of Flight Angiography TOF and Susceptibility-Weighted Imaging SWI. Both methods, however differently, relate to blood vessel imaging where TOF utilizes the less magnetization saturation that blood suffers due to its moving nature while SWI utilizes the magnetic properties of deoxyhemoglobin in venous structures and can also visualize other paramagnetic and ferromagnetic structures in the brain. New methods have been introduced to overcome existing limitations due to high field phenomena as well as add more efficiency and versatility to these imaging techniques.

The methods introduced in this work can be used independently or in one coherent imaging battery. A complete vascular imaging comparative study is yet to be performed at 4.7T utilizing both TOF methods to ameliorate the RF focusing effect (chapter 4), with the application of the method from chapter 5 to minimize the SAR effect due to saturation pulses and with the utilization of the method shown in chapter 3 to image any desired volume using SWI. Further, with the utilization of the method shown by Du (1) at higher field strength, all three methods can be applied within one imaging pulse sequence to achieve high quality vascular imaging. Although the three methods tackle different aspects of MRI, they can converge in one application.

In chapter 2, we have demonstrated the value of the combination of extremely high resolution T2WFSE and phase SWI for lesion detection in MS. In seven relapsing remitting MS patients at 4.7 T, we found that 18% of MS lesions were invisible on moderate and high resolution T2WFSE, but were observed on phase SWI. Phase SWI improves assessment of MS lesion load and emphasizes iron-containing lesions. Further MS studies are necessary to understand the signal time course of this new contrast mechanism in relation to both T2WFSE and gadolinium-enhancement.

In chapter 3, a new approach to 3D imaging was introduced which enabled accurate oblique SWI scanning while overcoming the current restriction to axial imaging to produce correct phase effects for oblique imaging. New results from oblique phase imaging were presented and the phase measurements from key brain structures were successfully validated against images obtained by the current standard of axial imaging. The new method allows us to image any tissue volume as needed and unconstrained by the volume's angle with the main field while still encoding the image in a manner aligning the imaging elements parallel with the field and hence preserving the SWI contrast.

In chapter 4, 3D Time-of-Flight (TOF) MRA was implemented at 3.0T and a method was introduced to ameliorate the deterioration in distal middle cerebral arteries MCA due to RF field focusing at this high field. The effect of RF destructive interference at 3.0T on ramped RF excitation pulses for TOF has been illustrated both theoretically and experimentally for imaging the intracranial arteries. For blood vessels flowing superiorly and to the periphery, changing the

167

linear ramp slope was shown to help counter the losses from RF interference. As verified in both simulations and normal volunteer experiments, altering the ramped excitation to 1.5 times its typical slope led to improved depiction of both the middle and posterior cerebral arteries.

In chapter 5, a new method was presented for two in one MRA/MRV scanning was introduced where full k-space scanning without saturation was followed by limited central k-space scanning with select saturation, using only an extra 13% of scan time, it was possible to obtain separate arterial and venous images of the neck vasculature. Total scan time could be reduced by as much as 46% and SAR due to spatial saturation could be reduced by as much as 92%.

6.1 Limitations on the research

In chapter 2, a 2D protocol might work better for visualizing higher grey to white matter contrast in magnitude images as well as hyper-intense magnitude lesions. Having said that, it might be an advantage to keep the current protocol where the antagonism of T1 weighting and T2* weighting produce an image with less magnitude image contrast that could make an occasional MS phase lesion more visible in the SWI results.

In chapters 2 and 3, there are few other limitations on the SWI method in general which are not covered in this work. One such limitation is due to large susceptibility changes at air-tissue interfaces. Another limitation would be the high pass filtering method as it is suspected to irreversibly remove intrinsic contrast from the image along with the unwanted lower spatial frequencies. This

can be more drastic in larger brain structures like the Putamen and Globus pallidus.

In chapter 4, the work was done only on healthy volunteers while patient studies must be conducted to confirm the clinical usefulness of the method for specific pathological conditions. With ramp pulses in general and more specifically with our increased slope ramp profiles, background behavior might make MIP (maximum intensity projection) of inferior quality because higher background intensity from some slices might overwhelm blood signal from a different slice.

6.2 Future directions

In Chapter 2, SWI is showing great promise for identifying previously invisible lesions in Multiple Sclerosis. More research is needed to investigate lesion formation and progression with the help of this method. Analyzing ROI measurements of the phase images from different key brain regions and structures is another important direction.

In chapter 3 "Imaging with Independent Excitation and Encoding", only 3D SWI methods were used. Similar and simpler 2D SWI application of this method should be verified experimentally. Chapter 2 and 3; A different phase filtering method should be investigated in attempt to preserve more of the intrinsic phase contrast that might be affected by the current high pass filtering method.

In chapter 4, the theoretically introduced two-stage pulse should be implemented experimentally and tested for experimental validation. Other RF shapes can be tailored for specific anatomical geometries of blood vessels. Higher

field experience is yet to be tested. Finally, the same work must be conducted on different patient populations to realize its potential as well as find its limitations if any. To solve the possible problem of MIP lower quality, another processing alternative should be found, especially that in most individual slices the blood to background contrast is of good quality.

In regard to chapter 5, the venous system has been understudied. This method will enable arterial and venous investigations with minimal time overhead.

6.3 References

1. Du YP, Jin Z. Simultaneous acquisition of MR angiography and venography (MRAV). Magnetic Resonance in Medicine 59:954–958 (2008).

Appendix 1

Flow compensation in Read Out and Slice Select directions;

Equations for Pulse Sequence Programming

The following equations define timing parameters for flow compensation gradient lobes for both read out and slice selection.

This text is continued from (section 1.4.2; page 49).

Read Out First Lobe Duration:

$Tc1 = 0.5/(12\ gc1^2 + 12\ gc1\ gc2)\ (- 24\ grate\ gc1^3 - 36\ gc1^2\ grate\ gc2 - 12\ gc1\ gc2^2\ grate + 4\ sqrt(24\ gc1^2\ grate^2\ gro^3\ gc2 + 36\ gc1^2\ gro^3\ t3\ grate + 18\ gc1^2\ grate^2\ gc2^2\ gro^2 + 36\ gc1\ gc2^2\ gro\ t3^2 + 24\ gc1\ gc2^2\ grate^2\ gro^3 + 36\ gc1\ gc2\ gro^2\ t3^2 + 18\ gc1\ gc2^3\ grate^2\ gro^2 + 9\ gc1\ gc2\ grate^2\ gro^4 + 36\ gc1^2\ gro\ t3^2\ gc2 + 72\ gc1^2\ gro^2\ t3\ grate\ gc2 + 9\ grate^2\ gc1^4\ gc2^2 + 18\ gc1^3\ grate^2\ gc2^3 + 9\ gc1^2\ gc2^4\ grate^2 + 36\ gc1^2\ gro^2\ t3^2 + 9\ gc1^2\ grate^2\ gro^4 + 36\ gc1^2\ gro\ t3\ grate\ gc2^2 + 72\ gc1\ gc2^2\ gro^2\ t3\ grate + 36\ gc1\ gc2\ gro^3\ t3\ grate + 36\ gc1\ gc2^3\ gro\ t3\ grate));$

Read Out Second Lobe Duration:

$Tc2 = - 0.5\ (- 2\ gro\ t3 - 2\ grate\ gc1^2 - gc1/(12\ gc1^2 + 12\ gc1\ gc2)\ (- 24\ grate\ gc1^3 - 36\ gc1^2\ grate\ gc2 - 12\ gc1\ gc2^2\ grate + 4\ sqrt(24\ gc1^2\ grate^2\ gro^3\ gc2 + 36\ gc1^2\ gro^3\ t3\ grate + 18\ gc1^2\ grate^2\ gc2^2\ gro^2 + 36\ gc1\ gc2^2\ gro\ t3^2 + 24\ gc1\ gc2^2\ grate^2\ gro^3 + 36\ gc1\ gc2\ gro^2\ t3^2 + 18\ gc1\ gc2^3\ grate^2\ gro^2 + 9\ gc1\ gc2\ grate^2\ gro^4 + 36\ gc1^2\ gro\ t3^2\ gc2 + 72\ gc1^2\ gro^2\ t3\ grate\ gc2 + 9\ grate^2\ gc1^4\ gc2^2 + 18\ gc1^3\ grate^2\ gc2^3 + 9\ gc1^2\ gc2^4\ grate^2 + 36\ gc1^2\ gro^2\ t3^2 + 9\ gc1^2\ grate^2\ gro^4 + 36\ gc1^2\ gro\ t3\ grate\ gc2^2 + 72\ gc1\ gc2^2\ gro^2\ t3\ grate + 36\ gc1\ gc2\ gro^3\ t3\ grate + 36\ gc1\ gc2^3\ gro\ t3\ grate)) - grate\ gro^2 + 2\ gc2^2\ grate)/gc2;$

Slice Select Middle Lobe Duration:

$Tss2 = 0.5$ (grate gss^2 + $GG3/(12\ GG3^2 + 12\ GG3\ GG2)$ (- 12 GG3 $GG2^2$ grate - 36 $GG3^2$ grate GG2 - 24 $GG3^3$ grate + 4 sqrt(72 $GG3^2$ Tss1 grate gss^2 GG2 + 72 GG3 $GG2^2$ Tss1 grate gss^2 + 36 GG3 $GG2^3$ grate gss Tss1 + 9 GG3 GG2 $grate^2$ gss^4 + 36 GG3 GG2 grate gss^3 Tss1 + 24 GG3 $GG2^2$ gss^3 $grate^2$ + 36 GG3 GG2 gss^2 $Tss1^2$ + 36 GG3 $GG2^2$ gss $Tss1^2$ + 18 GG3 $GG2^3$ $grate^2$ gss^2 + 36 $GG3^2$ $GG2^2$ grate gss Tss1 + 24 $GG3^2$ gss^3 $grate^2$ GG2 + 18 $GG3^2$ $grate^2$ gss^2 $GG2^2$ + 36 $GG3^2$ gss $Tss1^2$ GG2 + 36 $GG3^2$ gss^2 $Tss1^2$ + 9 $GG3^2$ $grate^2$ gss^4 + 9 $GG3^2$ $GG2^4$ $grate^2$ + 18 $GG3^3$ $GG2^3$ $grate^2$ + 9 $GG3^4$ $GG2^2$ $grate^2$ + 36 $GG3^2$ grate gss^3 gss^2 Tss1)) - 2 $GG2^2$ grate + 2 gss Tss1 + 2 $GG3^2$ grate)/GG2;

Slice Select Last Lobe Duration:

$Tss3 = 0.5/(12\ GG3^2 + 12\ GG3\ GG2)$ (- 12 GG3 $GG2^2$ grate - 36 $GG3^2$ grate GG2 - 24 $GG3^3$ grate + 4 sqrt(72 $GG3^2$ Tss1 grate gss^2 GG2 + 72 GG3 $GG2^2$ Tss1 grate gss^2 + 36 GG3 $GG2^3$ grate gss Tss1 + 9 GG3 GG2 $grate^2$ gss^4 + 36 GG3 GG2 grate gss^3 Tss1 + 24 GG3 $GG2^2$ gss^3 $grate^2$ + 36 GG3 GG2 gss^2 $Tss1^2$ + 36 GG3 $GG2^2$ gss $Tss1^2$ + 18 GG3 $GG2^3$ $grate^2$ gss^2 + 36 $GG3^2$ $GG2^2$ grate gss Tss1 + 24 $GG3^2$ gss^3 $grate^2$ GG2 + 18 $GG3^2$ $grate^2$ gss^2 $GG2^2$ + 36 $GG3^2$ gss $Tss1^2$ GG2 + 36 $GG3^2$ gss^2 $Tss1^2$ + 9 $GG3^2$ $grate^2$ gss^4 + 9 $GG3^2$ $GG2^4$ $grate^2$ + 18 $GG3^3$ $GG2^3$ $grate^2$ + 9 $GG3^4$ $GG2^2$ $grate^2$ + 36 $GG3^2$ grate gss^3 Tss1));